Francesco Mazzocchi

DEVELOPMENT OF NBN BASED KINETIC INDUCTANCE DETECTORS ON SAPPHIRE AND DIAMOND SUBSTRATES FOR FUSION PLASMA POLARIMETRIC DIAGNOSTICS

SCHRIFTENREIHE DES INSTITUTS
FÜR ANGEWANDTE MATERIALIEN BAND 108

KIT Scientific Publishing

Francesco Mazzocchi

Development of NbN based Kinetic Inductance Detectors on sapphire and diamond substrates for fusion plasma polarimetric diagnostics

Schriftenreihe
des Instituts für Angewandte Materialien
Band 108

Karlsruher Institut für Technologie (KIT)
Institut für Angewandte Materialien (IAM)

Eine Übersicht aller bisher in dieser Schriftenreihe erschienenen Bände finden Sie am Ende des Buches.

Development of NbN based Kinetic Inductance Detectors on sapphire and diamond substrates for fusion plasma polarimetric diagnostics

by
Francesco Mazzocchi

KIT Scientific Publishing

Karlsruher Institut für Technologie
Institut für Angewandte Materialien

Development of NbN based Kinetic Inductance Detectors on sapphire and diamond substrates for fusion plasma polarimetric diagnostics

Zur Erlangung des akademischen Grades eines Doktor-Ingenieurs von der KIT-Fakultät für Elektrotechnik und Informationstechnik des Karlsruher Instituts für Technologie (KIT) genehmigte Dissertation

von Francesco Mazzocchi, M.Sc.

Tag der mündlichen Prüfung: 6. Mai 2021
Hauptreferent: Prof. Dr. Ing. Theo Andreas Scherer
Korreferent: Prof. Dr. rer. nat. Sebastian Kempf

Impressum

Scientific Publishing

Karlsruher Institut für Technologie (KIT)
KIT Scientific Publishing
Straße am Forum 2
D-76131 Karlsruhe

KIT Scientific Publishing is a registered trademark of Karlsruhe Institute of Technology.
Reprint using the book cover is not allowed.

www.ksp.kit.edu

Print on Demand 2022 – Gedruckt auf FSC-zertifiziertem Papier

ISSN 2192-9963
ISBN 978-3-7315-1181-6
DOI 10.5445/KSP/1000144793

Considerate la vostra semenza:
fatti non foste a viver come bruti,
ma per seguir virtute e canoscenza

Dante, Divina Commedia, *Inferno*,
Canto XXVI, vv 118-120

Acknowledgment

I consider myself lucky for all the help, technical and not, that I received during this work and I want to acknowledge the people that played an important role in the birth of this thesis.
First of all, my deepest thanks to Prof. Dr. Ing. Scherer and to Prof. rer. nat. Kempf, for having given me the possibility to grow as a scientist and having always supported me during this experience. My gratitude goes also to my group leader, Dr. Ing. Strauss and to my institute director Prof. Dr. Ing. Gorr for having been supportive from the very first moment. A big thank you to Dr. Driessen for the patience and the competence he showed while dealing with me during our video-conferences and email exchanges. Thanks to Dr. Ilin for the always interesting and constructive discussions and for the invaluable help he provided during the production phase of the detectors. My gratitude goes also to Dr. Merker and Dr. Kuzmin for having helped me familiarize with the various measurement techniques employed in this work. Thanks to Dr. Grossetti for having relentlessly pushed me to be a better scientist and in general for bringing me into the world of research. Big thanks to all my other colleagues at work: Andreas Meier, Cathrin Schuler, Jutta Howell, Gaetano Aiello, Judith Jung, Peter Spaeh and Sabine Schreck: you all make the work place more pleasant. Thanks to Dr. Simondon, that took the time to proof-read part of this work and to give me suggestions. Merci beaucoup!
A huge shout to my sister Chiara, for the hours-long correction-of-the-thesis video-conferences we had during the writing phase and for giving me a very good example to get inspiration from. My dad Sergio and my other sister Nora get huge credit for putting up with me and all the love they gave me. Thanks to Silvia, for the evenings spent with pleasant discussions while cooking pasta and getting fatter together. Mad props to Eric and Mike, always ready to discuss everything from politics, to technology, to how perfectly smoke ribs or prepare cheese curds. Cheers, boys! Finally, a big thank to a wild bunch of friends (Anna, Eleonora, Lawrence and Manel) for making me live my personal version of the Decameron, and always having put a smile on my face.

Zusammenfassung

Die Kernfusion stellt eine der besten Chancen für die Menschheit dar, sich von fossilen Brennstoffen zur Energieerzeugung zu lösen, um die Probleme im Zusammenhang mit der globalen Erwärmung anzugehen. Das empfindliche Plasmagleichgewicht, das für einen stabilen Betrieb erforderlich ist, erfordert ein breites Spektrum verschiedener Diagnose-Methoden, die die verschiedenen Plasmaparameter laufend überwachen und dem Aufkommen von Instabilitäten entgegenwirken, die natürlich innerhalb eines Tokamaks auftreten. Polarimetrie gehört zu diesen Techniken, die sich in jahrzehntelangen Anwendungen in der Kernfusionsforschung als zuverlässiges Instrument erwiesen haben. Durch Messung der in die Polarisationsebene induzierten Rotation einer durch das Plasma wandernden elektromagnetischen Welle können wichtige Parameter wie die Stromdichte und das poloidale Magnetfeld rekonstruiert werden. Diese Arbeit untersucht die Anwendung von Kinetischen-Konduktivität-Detektoren (KIDs) auf Basis von Saphir- und Diamantsubstraten. Diese Art von Sensoren zeichnen sich durch einen sehr einfachen Aufbau aus, der aus einer einzelnen supraleitenden Dünnschicht besteht, und so einen LC-Schwingkreis bildet. Eintreffende Photonen mit ausreichender Energie brechen Cooper-paare innerhalb des Supraleiters auf und verändern dessen Oberflächenimpedanz. Dies führt zu einer Änderung der Resonanzfrequenz und Phase der Resonatoren, die mit Standard-Hochfrequenztechniken erfasst werden können. Das angenommene Design umfasst eine Multi-Pixel-Konfiguration mit Polarisationsempfindlichkeit für den Einzeldetektorbetrieb. Der Entwurfs- und Produktionsphase der Prototypen ging eine umfangreiche Simulations- und Modellierungsstudie voraus, die durchgeführt wurde, um den Bereich der Betriebsfrequenzen der Resonatoren zu bewerten, das Auftreten von Übersprechen zwischen den auf dem Detektor vorhandenen Pixeln zu untersuchen und die Kopplungsstärke zu bewerten zwischen den Resonatoren und

der Zuleitung, mit dem Ziel, die Detektoren für die jeweilige Anwendung zu optimieren. Die hergestellten Prototypen wurden dann durch Messungen charakterisiert, die die kritische Temperatur und den kritische Strom der abgeschiedenen Filme, die Reaktion der Resonatoren auf einen Anregungsfrequenz und auf eintreffende THz-Strahlung einschließen. Die Verwendung von Diamant als Substrat für derartige Geräte wird hier nach bestem Wissen erstmals vorgeschlagen. Die erhaltenen Ergebnisse zeigen, dass dieses Material, das sich durch außergewöhnliche mechanische, thermische und Strahlungshärteeigenschaften auszeichnet, ein vielversprechender Kandidat für einen vollständig optimierten Detektor für den Einsatz in zukünftigen Kernfusionskraftwerken ist.

Abstract

Nuclear fusion represents one of the best chances humanity has to detach itself from fossil fuels for energy production, in an effort to tackle the issues related with global warming. The delicate plasma equilibrium necessary to reach stable operation requires a wide array of different diagnostics capable of continuously monitoring the various plasma parameters and to counteract the insurgence of instabilities that naturally arise inside a tokamak. Polarimetry is among these techniques, having being proven as a reliable instrument in decades of nuclear fusion research applications. By measuring the rotation induced into the polarization plane of an electromagnetic wave traveling through the plasma, important parameters like the current density and the poloidal magnetic field can be reconstructed. This thesis studies the application of Kinetic Inductance Detectors (KID) based on sapphire and diamond substrates as the sensitive component of an innovative polarimetric diagnostic system. These kind of devices are characterized by a very simple construction, consisting in a single superconducting thin layer patterned to form an LC resonating circuit. Incoming photons with sufficient energy break down Cooper pairs within the superconductor, changing its surface impedance. This leads to a change of the resonance frequency and phase of the resonators that can be detected with standard radio frequency techniques. The adopted design includes a multi-pixel configuration with polarization sensitiveness for single detector operation. The design and production phase of the prototypes was preceded by an extensive simulation and modelization study performed to evaluate the range of operating frequencies of the resonators, to investigate the occurrence of cross-talk between the pixels present on the detector and to assess the coupling strength between the resonators and the feedline, with the aim of optimizing the detectors for the application at hand. The produced

prototypes where then characterized with measurements that include the critical temperature and current of the deposited films, the resonators response to an excitation tone and to incoming THz radiation. The usage of diamond as a substrate for these kind of devices is proposed here for the first time to the best of our knowledge. The results obtained show how this material, characterized by exceptional mechanical, thermal and radiation hardness properties, represents a promising candidate for a fully optimized detector to be employed in future nuclear fusion power plants.

Introduction

The global warming issues that characterize this era of ever growing energy needs represent one of the major challenges that scientists and engineers have to face nowadays. The need to increase the global energy output without relying on fossil fuels, especially in those countries which feature a rapid ongoing development as well as a demographic growth, requires a transition toward "greener" energy sources [1]. Magnetically-confined nuclear fusion power can, in principle, represent a solution to these problems, with its capability to produce vast amounts of energy with a very limited environmental impact.
In a D-T nuclear fusion reactor a 50/50 mixture of deuterium and tritium gases is heated to temperatures of the order of 10^4 keV (equivalent to hundreds of millions degrees) to enable the reaction

$$ {}^{2}_{1}D \; + \; {}^{3}_{1}T \rightarrow \; {}^{4}_{2}He \, (3.5MeV) \; + \; {}^{1}_{0}n \, (14.1 \; MeV) \tag{0.1} $$

The plasma, consisting of a mixture of free electrons and positively charged ions, is confined with the use of powerful magnetic fields to avoid contact with the reactor walls. The charged particles are driven into spiral trajectories along magnetic field lines generated by coils around the reactor chamber to ensure the plasma stability. The magnetic fields lines are generated by either planar coils in the toroidal and poloidal planes (tokamak concept), or specially twisted ones able to recreate the required field shape (stellarator concept). Currently there are numerous machines dedicated to the experimental study of plasma physics and to the development of materials capable of withstanding the extreme operational conditions imposed by fusion plasmas.
The most advanced of them all is the International Thermonuclear Experimental

Reactor (ITER), a tokamak machine under construction in the town of Cadarache, France. ITER is designed to be the first machine of this kind to have sufficient energy for a Q factor up to 10, leading to an output thermal power 10 times the required heating input. The goal is set to 500 MW of fusion power generated in front of 50MW spent to heat up the D-T plasma to the required temperatures of around 10 keV in pulses of at least 1000 s [2]. The operational plan of ITER will start with a basic performance phase of 10 years to study the physics of the plasma ignition and the capabilities of plasma control. Its plasma will represent the first occasion for scientists to study ignition and long pulse operation and will therefore be endowed with a full range of diagnostics able to measure the various parameters in the range of reference.

In this context, polarimetry is a well-established technique to measure fundamental plasma parameters, such as the electronic density and the poloidal field [3]. The rotation induced by the Faraday effect directly relates to the path integral of the two aforementioned quantities and, when coupled to the line integrated values of the electron density obtained by an interferometric system, the plasma current density can also be evaluated [4–7]. Additionally, safety factor profiles [8, 9] and electronic temperatures [10] inside the fusion plasma can be studied with this kind of devices. The majority of the polarimetric systems used and proposed so far all rely on high power gas lasers as source [11–18]. Such devices have several issues caused by their thermal stability, health hazards related to poisonous active media and high voltages, cost and demanding requirements for maintenance and space. To solve these issues, a novel polarimetric system based on Quantum Cascade Lasers (QCL) has been proposed by the High Frequency research group [19] at the KIT Institute for Applied Materials - Applied Materials Physics (IAM-AWP). QCLs are low cost, extremely compact and require a very limited amount of maintenance, solving most of the problems afflicting the previous systems. One drawback is that, especially at the frequencies selected and addressed in this work (1 - 1.5 THz), they lack the power of their gas counterparts, being limited to emission in the order of 0.1 - 0.25 mW [20]. Therefore, an appropriate high sensitivity detector must be used in conjunction with the QCLs. Polarization sensitivity is also a desired requirement since it allows for the simplification of the optical system of the final device. Kinetic Inductance Detectors (KID) [21] represent a

good candidate for this application, having all the required characteristics, and they are the subject of this thesis.
KIDs have been developed in the context of astrophysical observation of radiation captured by radio-telescopes at very low power conditions [22]. The working principle of these devices is based upon the change in quasi-particle density induced in a superconducting thin film, typically composed of pure aluminum operating at 250-300 mK, by the radiation impinging on it. In a superconductor, the charge carriers are pairs of electrons coupled through the exchange of a virtual lattice phonon. The photons that get absorbed break down the Cooper pairs back to normal conduction electrons, on the condition that their energy is higher than the superconductor energy gap ($h\nu > 2\Delta = 3.5\ k_B T_C$ as per BCS theory [23]). This results in a change of the value of the kinetic inductance L_k that derives from the inertia of the charge carriers and represents the inductive component of the reactance of a superconductor. If the thin film is structured as an LC microresonator circuit, the increase of surface impedance related to the absorption of radiation will then result in a shift of the resonance frequency and of the phase of the signal, both measurable with common radio-frequency (RF) techniques. The most prominent advantage of the KID devices is the possibility to excite and read these multi-pixel detectors with frequency dividing multiplexing (FDM) techniques. In this case, a comb of frequencies is injected inside the device. By carefully tuning each pixel to its own resonance frequency, absorption dips will appear in the output signal (measured as the scattering parameter S_{21}), making it possible to use a single feed line to excite and read multiple pixels at once. This greatly simplifies both the design and production of the detectors. Additionally, when a Lumped Element (LEKID) configuration is adopted [24], there is no need for antenna structures to couple the radiation to the absorber, which presents a purely planar geometry.
This work revolves around the study and development of custom KIDs as detectors to be used in a polarimetric diagnostic in the field of nuclear fusion. The customization is particularly necessary since this is the first attempt to apply this technology to the aforementioned context. In particular, it was decided to investigate different substrates and superconducting thin films thicknesses. The first depositions were performed on a silicon substrate to establish a baseline for

the deposition parameters that would result in good quality niobium nitride thin films, refining them later on for the depositions on sapphire and diamond substrates. Both sapphire and diamond show, compared to silicon, superior optical, mechanical and thermal properties and represent the bulk of the work carried on for this thesis. Of particular interest in the context of fusion as well as high energy colliders is the use of radiation-hard materials (such as diamond) that are capable of operating in environments flooded with highly energetic ionizing radiation. The resilience of the device deriving from these choices allows it to be installed in close proximity to the reactor, limiting the use of extensive waveguides infrastructures, necessary to carry the signal from and to the polarimeter. Additionally, the optical transparency and very low loss tangent of both sapphire and diamond [25] limit the detector internal losses, resulting in higher responsivity and signal-to-noise ratios. For the first time diamond has been considered and studied for use as substrate for superconducting thin films detectors, to the best of our knowledge.

The detector development was preceded by a numerical investigation of the Faraday effect induced by a fusion plasma, necessary to better define the range of the operational parameters involved in this application. This phase was followed by extensive simulations performed with the Sonnet Software EM simulation suite [26]. The calculations were carried on to tune the resonance frequencies of the resonators composing the detector, to estimate the coupling strength between the microstrip transmission line and the detector pixels, as well as to study the occurrence of cross talking. The measurements of superconducting thin film characterization provided the values of the critical temperature and thin film surface impedance of the samples necessary to define their kinetic inductance. L_k is a fundamental parameter in our simulations since it defines, together with the substrate electrical permittivity, the range of frequencies the patterned structures oscillate at. Frequency response measurements were performed with the use of a vector network analyzer (VNA) connected to a dipstick submerged in liquid helium. The higher critical temperature of niobium nitride [27] compared to aluminum [28] allows measurements to be performed at 4.2 K in common bath cryostats or directly in the LHe dewar, greatly simplifying both the characterization process and the operation of these devices. The optical response was

obtained with the use of one of these cryostats, equipped with attenuators (-10 and -20 dB) to decrease the input noise level and a combination of cryogenic and room temperature amplifiers at the output. The radiation source consisted in a tunable backward wave oscillator (BWO) with maximum base frequency of 350 GHz, tripled with a high frequency broadband multiplier from Virginia Diodes based on planar GaAs Schottky diodes [29]. The source was actually operated at 900 GHz, given the higher power output at that frequency compared to the maximum frequency 1.15 THz emission. The signal was chopped at 23 Hz and recorded with the same VNA used for the previous measurements.

Contents

List of Symbols

a = acceleration, lattice parameter
P = power
e = electron charge
ϵ_0 = permittivity of free space
c = speed of light
k_B = Boltzmann's constant
T = temperature, transmission coefficient
T_C = superconductor critical temperature
n_e = electron density
μ_0 = free space magnetic permeability
E = electrical field
σ = reaction cross section, conductivity
v = particle velocity
τ = confinement time, resonator ring-down time
Q = reaction quality factor, resonator quality factor
θ_F = Faraday angle
ν = Verdet constant, frequency
ν_e = electron collisional frequency
m_e = electron mass
ω = angular frequency
B = magnetic flux density
B_C = thermodynamic critical magnetic flux density
B_{C1} = lower critical magnetic flux density
B_{C2} = upper critical magnetic flux density
j = electric current density
i = imaginary unit

σ_1 = real part of conductivity
σ_2 = imaginary part of conductivity
$\mathbf{k}$ = wave vector
k = wave number
$\boldsymbol{\epsilon}$ = dielectric tensor
ϵ = permittivity
Ω = electron cyclotron frequency
N = refractive index, electronic states density
n = superconductor charge carrier total density, plasma ion density
n_n = superconductor quasi-particle density
n_s = superconductor Cooper pairs density
n_0 = superconductor Cooper pairs density at T = 0
λ_L = London magnetic penetration length
λ = effective magnetic penetration length, wavelength
v_F = Fermi velocity
ω_D = Debye frequency
Θ_D = Debye temperature
V = electron - phonon interaction potential
r = Cooper pair radius
Δ = superconducting energy gap
ξ = single particle energy
ξ_0 = coherence length
ξ_P = Pippard's coherence length
ξ_{GL} = Ginzburg - Landau coherence length
ℓ = electron mean free path
ϕ = macroscopic superconductor wave function, magnetic flux
ϕ_0 = magnetic flux quantum
L_k = kinetic inductance
L_m = geometric inductance
L = inductance
C = capacitance
Z = impedance
$\mathcal{E}$ = electro-motive force

h = Planck constant
$\Delta\nu$ = coupled resonator fractional bandwidth
$\Delta\nu_0$ = un-coupled resonator fractional bandwidth
$S_{i,j}$ = scattering parameter
κ = resonator - feedline coupling factor, Ginzburg-Landau parameter
τ_{qp} = quasi-particle life time
η = photon absorption efficiency factor β = effective wave number
λ_{Eff} = effective wavelength
A = plasma / detector absorption factor
ρ = resistivity
Λ = Pearl length

1 Motivation and Problem Definition

1.1 Magnetically confined nuclear fusion

The ability to extract energy from the nuclei of atoms represents one of the biggest achievement of science during the 20^{th} century, comparable to the Homo Erectus taming the fire-molecular energy. The basic concept behind this capability relies on nuclear reactions, in which the end-products are more stable atomic-nuclei systems (larger binding energy per nucleon, lower mass). The excess mass (energy) is released in a wide variety of ways, mainly through α, β, γ and neutron emission. Historically, this has been mostly performed through the process of fission of heavy nuclei, starting with the Chicago Pile 1 in 1942, the world's first artificial nuclear reactor, in an experiment led by Enrico Fermi. Referring to Fig. 1.1, it is immediately clear how fission represents an exothermic process for heavy nuclei. This leads, in the case of ^{235}U, to a total excess energy of 214 MeV, which can take the form of, for example, neutrons or γ emission, but mainly results in kinetic energy of the fragment nuclei, as they are driven apart by Coulomb repulsion. In a nuclear reactor, the fission reaction is initiated via neutrons that, impinging on a nucleus, induce the splitting [30]. From Fig. 1.1 it is also apparent that an alternative process to fission by "climbing" the binding energy curve from the other side of it can be found, starting with very light nuclei instead of heavy ones. If the product nucleus atomic weight stays below a mass of 56, then a net gain of energy will be obtained. This process is named nuclear fusion, and occurs naturally in very hot and dense environments, such as inside the core of a star.
Nuclear fusion presents several advantages over fission: as previously mentioned, the required fuel is composed of light atoms that are very abundant in nature, and

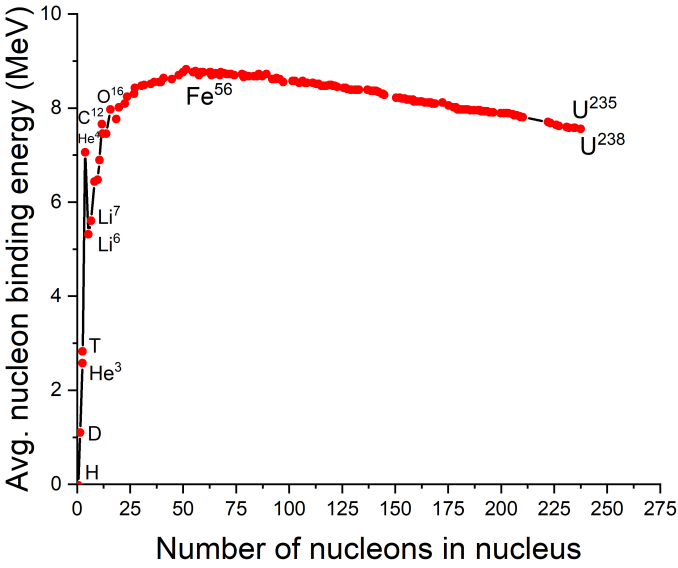

Figure 1.1: Binding energy per nucleon.

the products of the reactions are also light, stable nuclei, rather than heavy and radioactive ones. Unfortunately, fusion presents a big disadvantage, compared to fission: in order for the nuclear forces to start interacting, the Coulomb repulsion force between the nuclei must be overcome, whereas the neutrons inducing fission reactions bypass it, since they have no electrical charge. The general tendency is for the cross section of reactions induced by charged particles to decrease for decreasing energy [30]. One possible solution is to heat a container with the fuel in gaseous form until its thermal energy is high enough to increase substantially the probability of tunneling through the Coulomb barrier and allow the sustainment of the reactions. Thermonuclear fusion research main targets are improvements to the techniques that allow us to heat fusible nuclei and increase their density so that the number of reactions becomes large enough to self sustain, while giving

power outputs comparable with those of nuclear fission reactors (10^9 W). The most elementary of these reactions is

$$^1H +^1 H \rightarrow {}^2_1D + e^+ + \nu \qquad Q = 1.44\ MeV \tag{1.1}$$

where D represents a deuterium nucleus, e^+ is a positron and ν an electronic neutrino. This is also the first step in the proton-proton cycle powering the Sun. The presence of a neutrino indicates a weak interaction process, responsible for turning a proton into a neutron. Weak interactions are characterized by extremely small cross sections (in the order of 10^{-33} barns at keV energies) and therefore by extremely low reaction rates, making this reaction unpractical outside a star's core. Another reaction, characterized by the lowest activation energy, is:

$${}^2_1D +^3_1 T \rightarrow {}^4_2He\ (3.5\ MeV) +^1_0 n\ (14.1\ MeV) \tag{1.2}$$

or deuterium - tritium reaction. The high energy output and increased probability makes it the reaction of choice for Earth applications, given also the low activation energy.

In a thermonuclear reactor fuel temperatures and densities reach mean values around 10 keV and 10^{19-20} particles/m^3. Under these conditions, the fuel is ionized and forms a plasma that, being a mixture of positively charged ions and electrons, reacts to electromagnetic fields. Confining the plasma is the major issue present in thermonuclear fusion, since the energy exchange between the fuel and the reactor walls would decrease the temperature of the first and destroy the seconds. Given the nature of a long-pulse plasma, using magnetic fields to control its shape and dimensions (to *confine* it) is the most natural step to take in order to avoid damage to the reactor structures, while keeping the operational parameters within the range necessary to enable fusion reactions. The devices described in this thesis are designed to be employed in diagnostics dedicated to these techniques. Magnetic confinement fusion (MCF) is not the only configuration envisioned to confine the plasma, inertial confinement (ICF) being the other. In this case, the confinement comes from compression shock waves induced by laser

beams strucking simultaneously a small sphere of D-T mixture from multiple directions. The confinement of plasma is either way not total, since the particles lose energy via several mechanisms, the primary of which is *bremsstrahlung*: charged particles undergoing acceleration due to Coulomb scattering will radiate energy. An electron subject to acceleration a will radiate an amount of power equal to

$$P = \frac{e^2 a^2}{6\pi\epsilon_0 c^3}, \tag{1.3}$$

that translates to a power emitted per unit of volume equal to

$$P_{br} = 0.5 \times 10^{-36} Z^2 n n_e (k_B T)^{1/2}\ W/m^3, \tag{1.4}$$

with Z = 1 in case of hydrogen plasma, n and n_e being respectively ions and electrons densities and $k_B T$ expressed in keV. The reactor must be therefore operated at a temperature high enough to have a power gain able to counterbalance the various radiative losses plus the power needed to heat up the plasma. For a D-T plasma the balance starts to tilt in favor of energy production above 4 keV. Typical temperatures for the plasma reach 10 keV [31], and if equal densities for D and T (= 1/2 n) are assumed, the energy released per unit of volume is

$$E_f = \frac{1}{4} n^2 \langle \sigma v \rangle Q \tau. \tag{1.5}$$

Here Q is the energy release at each fusion reaction (17.6 MeV for D-T), σ is the reaction cross section, v is the particle velocity and τ is the confinement time, that gives a measure of the time scale within which the plasma can be considered confined. The quantity $\langle \sigma v \rangle$ is also referred to as reaction rate per particle pair. The total thermal energy (ions and electrons, assumed to have equal density n) is

$$E_{th} = 3 n k_B T, \tag{1.6}$$

therefore, to have a net energy gain from the reactor,

$$E_f \geq E_{th}, \tag{1.7}$$

which translates to the *Lawson criterion* [32]

$$n\tau > \frac{12k_BT}{\langle\sigma v\rangle Q}. \tag{1.8}$$

The Lawson formula for the self sustainability of the reactions has historically been a staple criterion in fusion reactors design. Eq 1.8 presents a minimum at T = 30 keV, at which point the criterion becomes

$$n\tau > 1.5 \times 10^{20}\, m^{-3}s. \tag{1.9}$$

The Lawson formula can be extended into a more useful figure of merit, called *triple product* (Fig. 1.2), by noting that τ is itself a function of T and its minimum shouldn't be taken as the optimum condition. As it turns out, a temperature of 10 keV is sufficient, thanks to quantum tunneling effects, to overcome the Coulomb

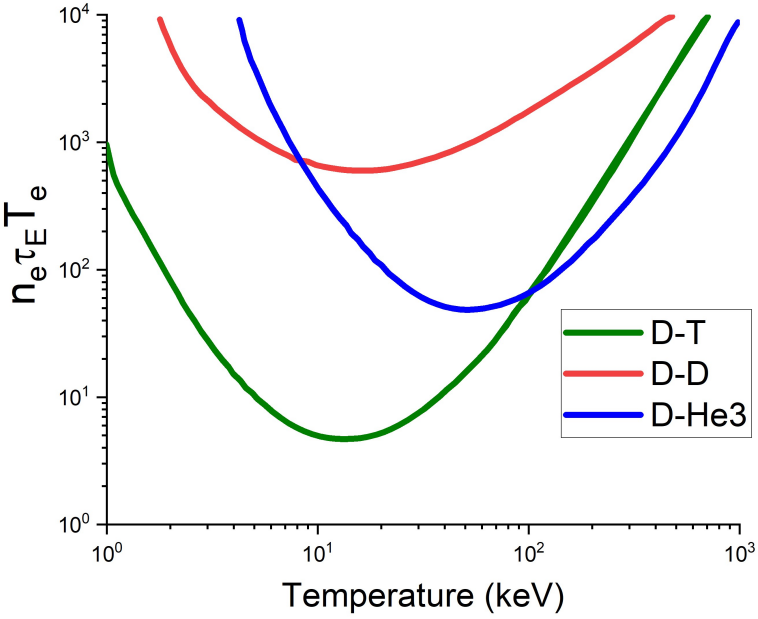

Figure 1.2: Fusion triple product criterion for D-T, D-D and D-He reactions.

barrier [33]. In this temperature range, the reaction rate can be estimated with a 10% precision as:

$$\langle \sigma v \rangle = 1.1 \times 10^{-24}\, T^2\, m^3\, s^{-1}, \tag{1.10}$$

which substituted in equation 1.8 together with Q = 3.5 MeV, yields the triple product condition for the D-T mixture:

$$nT\tau = 3 \times 10^{21}\, m^{-3}\, keVs. \tag{1.11}$$

This condition is for example reachable for $n = 10^{20}\ \ m^{-3}$, $T = 10\ keV$, and $\tau = 3\ s$.

1.1.1 Reactor design: tokamaks and stellarators

As mentioned above, several design concepts have spurred from research since the late fifties. The two most promising ones are the tokamak [34] and the stellarator [35]. They both are toroidal machines, but differ in the way they generate the magnetic fields responsible for the plasma confinement. In the former type of machine, the main (toroidal) field lines are generated by planar coils and lie parallel to the horizontal plane of the machine, in a continuous loop. The charged particles composing the plasma form spiral trajectories around the magnetic field lines as they move around the loop. If only the toroidal field was present, these trajectories would increase in size as the particles travel, since the field at the inner side of the loop is more intense than it is in the outer regions. This would result in impact against the wall of the reactor, and impossibility to obtain a proper stable plasma. To counteract this magnetic field gradient, an additional *poloidal* component generated by the plasma current and lying parallel to the cross section of the torus (fig. 1.3), is necessary. In the case of stellarators, the magnetic coils are carefully shaped in order to natively generate both magnetic field components. Following the development of the above theory, several machines have been built [36–43] all around the world. Tokamaks and stellarators, while both very promising, are still in an experimental phase and are equipped with a very wide range of diagnostic equipment, with the double task of monitoring the plasma operational parameters

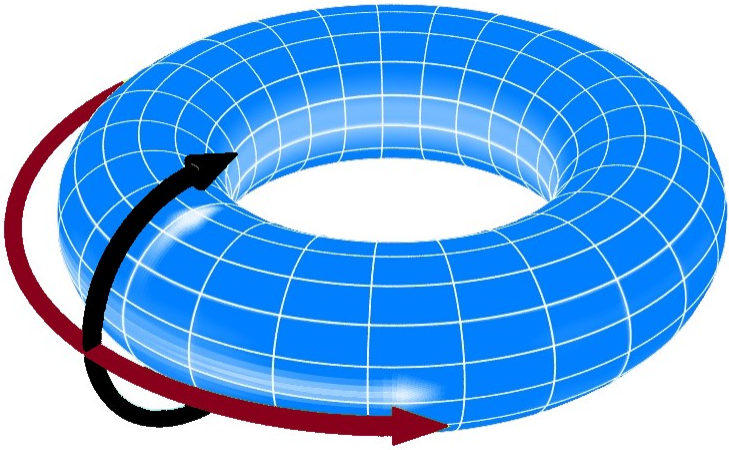

Figure 1.3: Toroidal (red) and poloidal (black) directions of the magnetic field lines in a closed loop fusion machine.

and study the complex physics behind ignition, plasma heating, instability control and many more topics. The large range of charged particles masses and velocities requires experiments, as numerical methods cannot yet suffice.

1.2 Polarimetry

Polarimetry is the measure of the Faraday rotation angle of a light beam when it propagates through a magnetized media (Fig.1.4). The most general expression for small angles of rotation is given by (in radians):

$$\theta_F = \nu B d, \tag{1.12}$$

where B is the magnetic flux density along the propagation direction, d is the light path length and ν is the Verdet constant, function of temperature and wavelength, and expresses the proportionality between applied magnetic field, rotation and distance in a given material. In the case of a plasma, the effect is purely caused

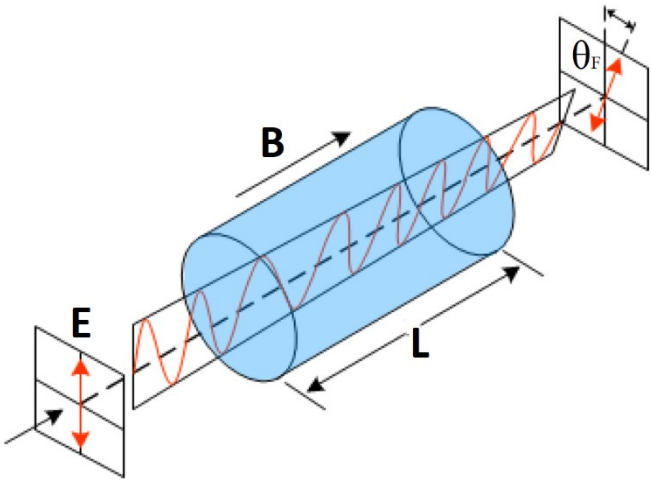

Figure 1.4: Representation of the Faraday effect.

by the free electrons, and the rotation depends only on the squared wavelength of the probing light [44]:

$$\theta_F = \frac{e^3}{2\epsilon_0 m_e^2 c}\frac{1}{\omega^2}\int n_e\,(z)\,B_{\|}dz, \tag{1.13}$$

where $B_{\|}$ (z) is the longitudinal magnetic field along the line of sight and n_e is the electron density. This formula is valid for non relativistic electron motion. The phenomenon arises from the presence of a magnetic field in the medium. The symmetry between the plasma dielectric constant for right and left handed circular polarization components of the electromagnetic (EM) wave is disrupted, given the different response electrons have to them. The result of such asymmetry is the rotation of the polarization vector, which is a function of the square of the wavelength, of the electron density and parallel component of the magnetic field. Once coupled with the additional information about the electron density given by an interferometric system, the estimation of both magnetic field and current density can be obtained, given that

$$\int n_e\left(z\right) B_{\parallel} dz \approx j. \tag{1.14}$$

Since the beginning of nuclear fusion machine research, polarimetry has been an essential instrument to estimate fundamental plasma parameters, such as electronic density and poloidal field, from the measure of the Faraday rotation angle [3]. Combined (and integrated) together these quantities give a value of the plasma current [4–7, 9]. It is therefore mandatory to have the most precise instrument with the widest dynamic range as possible, in order to be able to precisely measure such quantities. Current and past polarimetric systems employ gas lasers, typically HCN @337μm [11–13], HCOOH @ 433 μm [14–16] and DCN @195 μm [17, 18]. In other application fields, polarimetry has been extensively used as a way to characterize materials at multiple wavelengths. Materials that have been investigated through this technique include optical materials [45–48], bio-molecules [49] and bio-compatible materials [50], superconductors [51] and semiconductors [52, 53]. The Faraday effect can also be used in magnetic field and current sensors [54–57]. Faraday rotators employ this effect to rotate the polarization plane of a laser beam in order to avoid dangerous back reflections into the main oscillation cavity [58–60]. In analogy with interferometric systems, polarimeters can adopt various working schemes [61]. Our iteration of the polarimeter foresees the use of single, polarization sensitive multi-pixel detector. The laser beam enters the plasma, is reflected by retro-reflectors placed on the first wall at the high field side and returns back into the device, where it is detected by a single polarization sensitive detector. By using QCLs in place of gas lasers, costs and space footprint can be greatly reduced while power stability and reliability increase. QCLs have a wide frequency range (0.85 $\rightarrow$ 5 THz, roughly 350 $\leftarrow$ 60 μm) with the most common being 2.8 THz (107 μm), capable of ambient temperature operations (Fig. 1.5 and 1.6). Such a laser would give us rotations in the range of 0 - 5 degrees with typical conditions that can be found in middle-sized tokamaks ($n_e = 3 \rightarrow 9 \cdot 10^{19}$ m^{-3}, $B_{\parallel} \approx 0.2 \rightarrow 0.4$ T, plasma radius ≈ 1 m) [62], therefore a laser with a lower frequency would be better suited. Prototypes of 1.2 THz (250 μm) are being tested and applying a strong magnetic field would decrease the frequency to 0.85 THz (350 μm) [63]. The problem in this case

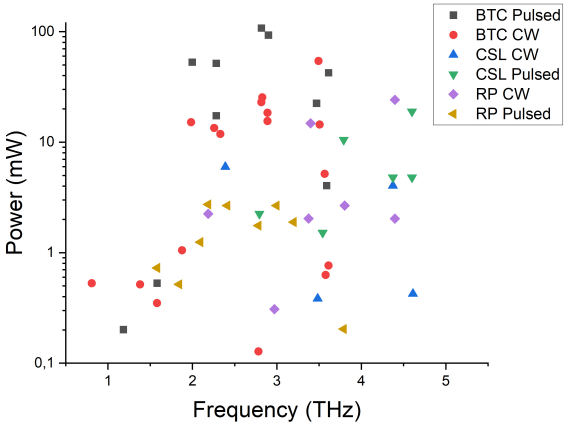

Figure 1.5: Peak optical power as a function of lasing frequency for different kinds of QCL, based on active region design (CSL = Chirped SuperLattice, BTC = Bound - To - Continuum, RP = Resonant Photon).

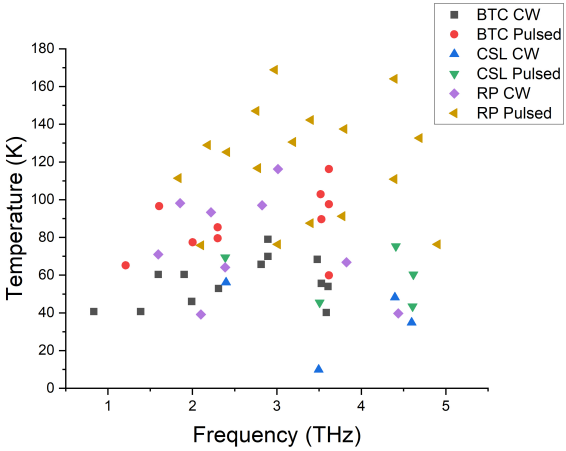

Figure 1.6: Peak operating temperature as a function of lasing frequency for different kinds of QCL, based on active region design (CSL = Chirped SuperLattice, BTC = Bound - To - Continuum, RP = Resonant Photon).

resides in the fact that, at these frequencies, the laser transitions are in the energy range of few meV. At ambient temperature or during continuous wave operation, the rise in thermal activity of the device can lead to longitudinal optical phonons scattering between lasing levels, resulting in a degradation of the population inversion. These devices therefore require cooling at liquid helium temperature levels in order to work properly [20, 64]. The inherent advantages of QCLs are their extremely compact size, ruggedness, and low price. They require minimal maintenance and the sources can be easily swapped in case of need. Their low price allows also to design multiple-sources machines for multiple lines-of-sight at a fraction of the cost of a single gas laser operating at THz frequencies.

1.3 Kinetic inductance detectors

Given the lack of source power compared to current gas laser based systems, a very high signal-to-noise (S/N) ratio detector is required. Under this point of view, KIDs [28] represent an attractive candidate. Based upon superconducting micro-resonators, their main advantages over other kind of detectors include a very simple, single layer structure that can be realized with conventional photolithographic techniques, fast action and frequency division multiplexing (FDM) readout, where a single transmission line is able to read-out a large number of pixels simultaneously. KIDs can also be designed to be polarization sensitive, in which case the pixels composing the detector are capable of selectively respond to light polarized along the direction of choice. The aluminum KID can reach a noise-equivalent power (NEP) of around $10^{-19}\ W\sqrt{Hz}$, [65] but requires temperatures in the order of 250-300 mK [28, 66], increasing both the assembly and operating costs. The usage of high T_c materials in the construction of these devices can, nevertheless, solve this problem. Developed for the use in astrophysics and astronomy ([67–70]) where power available is in the order of the nano and picowatt, KIDs can in principle be adapted to applications in plasma diagnostics. Photons with energy higher than the gap of an absorbing superconductor break Cooper pairs and change the absorber macroscopic electrical properties. The increased density of quasi-particles (conducting electrons) changes the surface

reactance of the superconductor (kinetic inductance effect). This effect can be measured efficiently when the absorber is implemented into a resonator circuit coupled to a transmission line (fig. 1.7), via the complex transmission scattering parameter S_{21}. The kinetic inductance of such devices can be calculated with the following formula [71]

$$L_{kin} = \frac{\sigma_2}{d\,(\sigma_1^2 + \sigma_2^2)\,\omega} \tag{1.15}$$

where σ_1 is the real part of the general circuit conductivity and σ_2 the imaginary one, d is the thickness of the absorber thin film and ω the angular frequency. The material of choice for the superconducting film is niobium nitride (NbN). With a critical temperature comprised in the 10 - 16 K range [27, 72], these thin films transit to the superconducting state at a temperature higher than liquid He

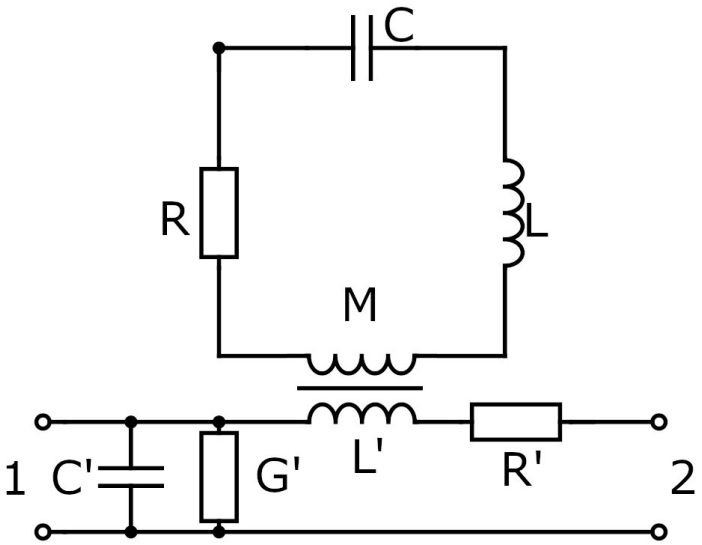

Figure 1.7: Schematics of a RLC resonating circuit coupled to a transmission line via mutual inductance M.

(4.2 K), simplifying the characterization of the final product and its operation. The design dimensions of the absorber strongly depend on the wavelength of the radiation to be measured. The single elements of the schematic resonator shown in Fig. 1.7 take the form of an interdigital capacitor and of a meandered line, the inductive section, and a microstrip transmission line (Fig. 1.8). Our iteration will need to detect a single frequency at much higher power than what they were originally designed for, therefore particular care was taken into the design phase to limit the occurrence of saturation. At the same time, the arrays used in astronomic measurements have a pixel count that often reaches the thousands, while for the current applications smaller amounts of pixels are sufficient. This characteristic allows us to introduce a greater separation between the frequencies of the single resonator units. The increased power impinging on the detector will result in a higher photon generated noise, with expected values in the order of $10^{-13}\ W/\sqrt{Hz}$.

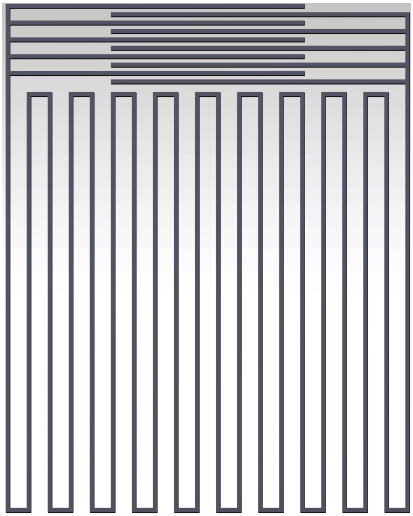

Figure 1.8: CAD 2D model of one of the pixels used in the KIDs. The microstrip feed line is not shown.

1.4 Scientific and technological motivation: problem assignment

Achieving fusion power in a reliable and safe way is one of the biggest challenges that scientists and engineers have in front of them, considering issues like global warming and the increasing energy demands of a world population that gets larger and larger. Reaching targets such as ignition, plasma stability and large Q values is highly dependent on the methods employed to study and monitor the operational plasma parameters in fusion machines. In the perspective of a transition from experimental to commercial reactors, the need for cheap and flexible diagnostics is also of primary importance, since whereas the first experimental machines are designed in the optic of physics investigation and plasma optimization, future power reactors like DEMO [73] will need to make commercial fusion a viable option under the practical and economical aspect. More compact, safe, inexpensive and reliable diagnostics are therefore needed. The Kinetic Inductance Detectors at the core of this thesis represent a promising new application for this kind of technology. The planar, mono-layer geometry translates to low-cost and simple production. These devices require no Josephson junctions or tuned bi-layers, so fabricating uniform arrays should present no problems [74]. The materials that will be studied as possible substrates are silicon, sapphire and CVD grown policrystalline diamond. They are very resistant to shock, thermal cycling and radiation, so the devices are rugged and are ideal for an environment potentially flooded with different kinds of radiation [74]. The superconducting thin films are realized with the deposition of niobium nitride (NbN). This material is relatively innovative in this application field and, with its higher critical temperature of roughly 14 K for good quality films, allows operation with simple liquid helium cryostats instead of mK level refrigerators. The chosen multi-pixel polarization sensitive configuration simplifies the final system, foregoing calibration issues that could arise by using two different detectors. Operating at THz frequencies should allow us to obtain appreciable Faraday rotation angles improving the response of the final instrument, with negligible absorption and refraction effects and larger optical tolerances allowed [75]. Typical polarimetric and interferometric systems currently operated as plasma diagnostics operate at millimeter to sub-millimeter

ranges ($\lambda \approx$ 100-2000 μm) to limit refraction, a strong effect for long wavelengths, while avoiding problems related to mechanical vibration and optical path stability that plague optical and NIR frequencies.
This work is organized as follows: in chapter 2 the theoretical basics of resonators, superconductivity and polarimetry are presented. Chapter 3 deals with the simulation and design phase, walking the reader through the process that lead to the choice of operational parameters and how the possibility of occurrence of various phenomena was studied via numerical calculations. Chapter 4 will illustrate the production process of the chips, while results of the characterization measurements are dealt with in the chapter 5. Chapter 6 presents the general design of a polarimeter based on the KIDs, while chapter 7 will summarize the presented work.

2 Physics Background

The following chapter presents the theoretical basis behind the physical principles of polarimetry and Kinetic Inductance Detectors (KID). Section 2.1 deals with how electromagnetic waves propagate through a magnetized plasma and how the electrical characteristic of this peculiar medium influences the polarization state of light. The second part of the chapter presents a general overview of the physical laws that govern the phenomenon of superconductivity, and their consequences on the electrodynamics of superconducting devices (section 2.2). The third part delves on how a resonant circuit behaves and how all the aforementioned properties can be exploited to build a radiation detector of very high sensitivities (section 2.3). The chapter is concluded by a description of the model that has been used to estimate the noise levels of the KIDs (2.4).

2.1 Faraday effect

Magnetized plasma, such as the one contained in a fusion reactor, is a birefringent and active medium. Propagation of EM waves inside a magnetized plasma is rather complex, since the presence of magnetic fields translates to highly anisotropic electrical properties [76]. In this scenario, large differences arise between the dynamics of electrons moving parallel to the field with respect to those moving perpendicular to it. Depending on the angle between the direction of propagation of an electromagnetic wave and the magnetic field lines, several effects can therefore manifest. Perpendicular propagation gives raise to the Cotton - Mouton effect, responsible for changing the ellipticity of the polarization, while parallel propagation results in the Faraday effect, a rotation of the polarization plane. In

the following section, the plasma will be treated like a conductive continuous medium governed, however, by the vacuum form of Maxwell equations.

2.1.1 Appleton - Hartree formula

The optical dispersion relation for a magnetized plasma is determined on the basis of the Maxwell field-equations [76]:

$$\nabla \times \mathbf{E} = -\frac{\partial \mathbf{B}}{\partial t} \tag{2.1}$$

and

$$\nabla \times \mathbf{B} = \mu_0 \mathbf{j} + \epsilon_0 \mu_0 \frac{\partial \mathbf{E}}{\partial t} \tag{2.2}$$

where $\mathbf{B}$ and $\mathbf{E}$ are the magnetic and electric fields, respectively. Substituting to eliminate $\mathbf{B}$ yields the differential equation

$$\nabla \times (\nabla \times \mathbf{E}) + \frac{\partial}{\partial t}\left(\mu_0 \mathbf{j} + \epsilon_0 \mu_0 \frac{\partial \mathbf{E}}{\partial t}\right) = 0. \tag{2.3}$$

A solution for $\mathbf{E}$ can be obtained assuming a linear relationship between the current $\mathbf{j}$ and the electrical field $\mathbf{E}$. This means that if a variation of the electrical fields $\mathbf{E_1}$ and $\mathbf{E_2}$ results in a variation of currents $\mathbf{j_1}$ and $\mathbf{j_2}$, respectively, then for the aforementioned linearity $\mathbf{E_1} + \mathbf{E_2} \propto \mathbf{j_1} + \mathbf{j_2}$. Moreover, the plasma is considered to be homogeneous in time and space. By taking these two premises into account, it is possible to make a Fourier analysis of both fields and currents, treating each component separately:

$$\mathbf{E}(\mathbf{x}, t) = \int \mathbf{E}(\mathbf{k}, \omega) e^{i(\mathbf{kx} - \omega t)} \frac{d^3\mathbf{k}}{(2\pi)^3} \frac{d\omega}{2\pi}, \tag{2.4}$$

and to relate $\mathbf{j}$ and $\mathbf{E}$ by means of the Ohm's Law:

$$\mathbf{j}(\mathbf{k}, \omega) = \boldsymbol{\sigma}(\mathbf{k}, \omega) \cdot \mathbf{E}(\mathbf{k}, \omega), \tag{2.5}$$

where $\boldsymbol{\sigma}$ is the plasma conductivity, $\mathbf{k}$ is the wave vector and ω is the wave angular frequency. Eq. 2.3 can be written for a particular Fourier mode taking $\epsilon_0\mu_0 = 1/c^2$, giving:

$$\mathbf{k} \times (\mathbf{k} \times \mathbf{E}) + i\omega \left(\mu_0 \boldsymbol{\sigma} \cdot \mathbf{E} - \epsilon_0 \mu_0 i\omega \cdot \mathbf{E}\right) = 0, \tag{2.6}$$

which becomes

$$\left(\mathbf{kk} - k^2\mathbf{i} + \frac{\omega^2}{c^2}\boldsymbol{\epsilon}\right) \cdot \mathbf{E} = 0, \tag{2.7}$$

where $\boldsymbol{\epsilon} = \left(\mathbf{i} + \frac{i}{\omega\epsilon_0}\boldsymbol{\sigma}\right)$ is the dielectric tensor, with $\mathbf{i}$ representing the unit vector. Expression 2.7 represents a system of homogeneous equations for the components of $\mathbf{E}$ whose non-zero solutions (the plasma dispersion relation) are given by the eigenvalues of the 3x3 matrix

$$\left(\mathbf{kk} - k^2\mathbf{i} + \frac{\omega^2}{c^2}\boldsymbol{\epsilon}\right). \tag{2.8}$$

In the simplest case of an isotropic medium,

$$\boldsymbol{\sigma} = \sigma\mathbf{i} \quad \boldsymbol{\epsilon} = \epsilon\mathbf{i}. \tag{2.9}$$

Taking $\mathbf{k}$ along the z axis and equating the determinant of equation 2.8 to zero leads to

$$-k^2 + \frac{\omega^2}{c^2}\epsilon = 0 \tag{2.10}$$

and

$$\frac{\omega^2}{c^2}\epsilon = 0, \tag{2.11}$$

which represent waves with transverse ($\mathbf{k} \cdot \mathbf{E} = \mathbf{0}$) and longitudinal ($\mathbf{k} \times \mathbf{E} = 0$) polarizations, respectively.

An explicit expression of the plasma conductivity (and, consequently, of its permittivity) can be now introduced, since these quantities are responsible for governing the propagation of electromagnetic waves inside a plasma. In the frame of the cold plasma approximation, the dielectric tensor in the presence of a static magnetic field B_0 can be rewritten as:

$$\boldsymbol{\epsilon} = \begin{bmatrix} 1 - \frac{\omega_p^2}{\omega^2 - \Omega^2} & \frac{i\omega_p^2 \Omega}{\omega(\omega^2 - \Omega^2)} & 0 \\ -\frac{i\omega_p^2 \Omega}{\omega(\omega^2 - \Omega^2)} & 1 - \frac{\omega_p^2}{\omega^2 - \Omega^2} & 0 \\ 0 & 0 & 1 - \frac{\omega_p^2}{\omega^2} \end{bmatrix}, \tag{2.12}$$

where $\Omega \equiv eB_0/m_e$ is the electron cyclotron frequency , and

$$\omega_p = (n_e e^2/\epsilon_0 m_e)^{1/2} \tag{2.13}$$

denotes the plasma frequency. The following dimensionless quantities can be introduced to simplify the notation:

$$X = \omega_p^2/\omega^2, \quad Y = \Omega/\omega, \quad N = kc/\omega. \tag{2.14}$$

By substituting equations 2.12 and 2.14 into equation 2.8, and by choosing the axis so that $k_x = 0$ and $B_0 \parallel z$, the Appleton-Hartree formula for the refractive index is obtained:

$$N^2 = 1 - \frac{X\,(1 - X)}{1 - X - \frac{1}{2}Y^2 \sin^2\theta \pm \left[\left(\frac{1}{2}Y^2 \sin^2\theta\right)^2 + (1 - X)^2\, Y^2 \cos^2\theta\right]^{1/2}}, \tag{2.15}$$

where θ is the angle formed by $\mathbf{k}$ and $\mathbf{B_0}$. In the case of parallel propagation, eq. 2.15 simply becomes

$$N^2 = 1 - \frac{X}{1 \pm Y} \tag{2.16}$$

and the waves have two circularly polarized contra-rotating components with k along the z direction, namely

$$\frac{E_x}{E_y} = \pm i \quad E_z = 0. \tag{2.17}$$

2.1.2 Faraday rotation

An electromagnetic wave in the form given in equation 2.17 presents different refractive indices N_+ and N_- for the two characteristics components, the superposition of which determines the amplitude of the original wave [76]. Since the difference in refractive indices will determine a phase delay between the two components, the polarization of the wave will vary in space. Let's suppose that at $z = 0$ the wave is linearly polarized along the x direction ($E_x = E$ and $E_y = 0$), therefore:

$$\mathbf{E}(0) = \frac{E}{2}\left[(1,-i) + (1,+i)\right], \tag{2.18}$$

which at $z \neq 0$ will become

$$\begin{aligned}\mathbf{E}(z) &= \frac{E}{2}\left[(1,-i)\exp\left(iN_+\frac{\omega}{c}z\right) + (1,+i)\exp\left(iN_-\frac{\omega}{c}z\right)\right] \\ &= E\exp\left[i\left(\frac{N_+ + N_-}{2}\right)\frac{\omega}{c}z\right]\left(\cos\frac{\Delta\phi}{2}, \sin\frac{\Delta\phi}{2}\right),\end{aligned} \tag{2.19}$$

where

$$\Delta\phi = (N_+ - N_-)\frac{\omega}{c}z \tag{2.20}$$

is the phase difference induced by the different refractive indices. The polarization of the wave is still linear, but rotated by $\frac{\Delta\phi}{2}$ after a distance z.
In the case of a magnetized plasma propagation, equation 2.7 needs to be solved for $\mathbf{E}$. In the current coordinate system (k along the z axis, x axis perpendicular to B), the transverse components of the electric field are related by:

$$\frac{E_x}{E_y} = -\frac{iY\sin^2\theta}{2(1-X)\cos\theta} \pm i\left[1 + \frac{Y^2\sin^4\theta}{4(1-X)^2\cos^2\theta}\right]^{1/2} \tag{2.21}$$

which for propagation quasi parallel to the magnetic field ($Y\sin\theta \ll 1$) yields in its lowest order of approximation equation 2.17. The Faraday rotation angle θ_F can then be expressed as:

$$\theta_F = \frac{\Delta\phi}{2} = \frac{1}{2}\left(N_+ - N_-\right)\frac{\omega}{c}z \approx \frac{1}{2}\left[\frac{XY\cos\theta}{(1-X)^{1/2}}\right]\frac{\omega}{c}z. \tag{2.22}$$

If $X \ll 1$, the latter expression can be approximated as:

$$\theta_F \approx \frac{\omega_p^2 \Omega\cos\theta}{2\omega^2 c}z. \tag{2.23}$$

The Faraday rotation is therefore dependent on the electron density (through ω_p), on the parallel component of the magnetic field ($\Omega\cos\theta$) and on the square of the probing wavelength. It is important to know that the latter formula is valid only for a uniform plasma, whereas fusion machines present non-uniform electron-density profiles. In such cases, the electron density $n_e(z)$ and the parallel magnetic field $B_\parallel$ must be integrated along the line of observation of the probing beam, obtaining:

$$\theta_F = \frac{e^3}{2\epsilon_0 m_e^2 c}\frac{1}{\omega^2}\int n_e\left(z\right)B_\parallel\left(z\right)dz. \tag{2.24}$$

Given the strong dependence of the rotation on the frequency of the probing beam, it is mandatory to perform a preliminary evaluation of the expected values for θ_F choosing different sources and density profiles, see chapter 3.

2.2 Superconductivity

Superconductivity is defined as a sharp decrease to zero of the DC resistance of certain materials when their temperature drops below a certain value T_C, called critical temperature [23]. It is a quantum mechanical phenomenon and was first observed by dutch physicist Heike Kamerlingh Onnes in 1911 in mercury, following his successful attempt to liquefy helium [77]. The next big step in this field would come in 1933, when Meissner and Ochsenfeld discovered the effect that carries their name, which is the expulsion of any internal magnetic field from the superconductor [78]. This effect was phenomenologically explained by Fritz

and Heinz London in 1935 [79], establishing the relationship between the super-carriers current densities and the electromagnetic field, while the microscopic explanation was the focus of the theory proposed in 1957 by Bardeen, Cooper and Schrieffer (BCS theory) [80].

2.2.1 London's Theory

The main concept behind London's theory of superconductivity is that electrons in a superconductor are considered as being part of two distinct charge carriers: superconducting and normal electrons. It is therefore convenient to introduce what is known as two-fluid model to fully explain the zero resistivity and perfect diamagnetism [81]. This model was first proposed by Gorter and Casimir in 1934, anticipating the formal description of Cooper pairs by more than two decades [82]. Within these premises, in the context of the two fluid model [71], at any given temperature the charge carrier density n is given by:

$$n = n_n + n_s, \tag{2.25}$$

with n_n representing the normal electron density and n_s the one related to the superconducting charge carriers (figure 2.1). The latter is given by [83]:

$$n_s = n_0 \left\{1 - (T/T_C)^4\right\}, \tag{2.26}$$

with n_0 being the superconducting charge carriers density at $T = 0$. In absence of resistance, electrons in an electric field E will continue to accelerate indefinitely, since:

$$\frac{dv}{dt} = \frac{eE}{m_e}, \tag{2.27}$$

where e, v, m_e are electron charge, velocity and mass. As stated in ref. [83], the following equivalence holds:

$$\frac{d}{dt}\left(n_s e v\right) = \left[\frac{n_s e^2}{m_e}\right] E = \frac{d}{dt}(j_s), \tag{2.28}$$

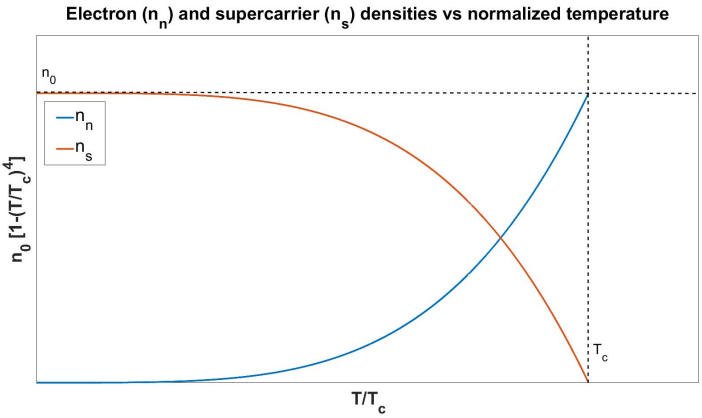

Figure 2.1: Super and Normal Electrons densities as function of temperature.

with j_s being the super-carriers current density.
If an external magnetic field B is present, the electromagnetic flux can be expressed in terms of a vector potential A:

$$B = \nabla \times A \tag{2.29}$$

and

$$E = -\left|\frac{\partial A}{\partial t}\right|. \tag{2.30}$$

From the combination of equations 2.28 and 2.30 the first London equation is obtained:

$$\frac{d}{dt}(j_s) = -\frac{n_s e^2}{m_e}\left[\frac{\partial A}{\partial t}\right], \tag{2.31}$$

which integrated gives an expression for the current density j_s:

$$j_s = -\left(\frac{n_s e^2}{m_e}\right) A. \tag{2.32}$$

By combining the Ampere law

$$\nabla \times B = \mu_0 j_s, \tag{2.33}$$

with expression 2.29 and 2.32, the second London's equation is obtained:

$$\nabla \times (\nabla \times B) = -\left[\frac{n_s e^2}{m_e}\right] \mu_0 B. \tag{2.34}$$

Assuming the external field to be oriented along the z direction, the field inside the superconductor perpendicular to the external one can be expressed as:

$$\frac{d^2 B(x)}{dx^2} = \frac{\mu_0 n_s e^2}{m_e} B(x), \tag{2.35}$$

which presents solutions in the form

$$B(x) = B_0 \exp(-x/\lambda_L). \tag{2.36}$$

The magnetic flux is maximum at the surface of the superconductor, with a value of B_0, and drops exponentially to $1/e$ of its initial value once it penetrated a distance λ_L (London's penetration depth) inside the superconductor. The quantity λ_L can be expressed in terms of n_e, m_e and e:

$$\lambda_L = \sqrt{\frac{1}{\mu_0}\left[\frac{m_e}{n_s e^2}\right]}. \tag{2.37}$$

Taking into consideration equation 2.26, the dependence of the penetration depth from the temperature can be explicitly obtained by substituting n_s into eq. 2.37:

$$\lambda_L = \sqrt{\frac{1}{\mu_0}\left[\frac{m_e}{n_0\left\{1-(T/T_C)^4\right\} e^2}\right]}. \tag{2.38}$$

From equation 2.38 it is apparent how as the temperature increases, the density of supercarriers decreases, allowing a deeper penetration of the field.

2.2.2 BCS Theory

The dynamics of superconductivity implies that the phenomena generating it are cooperative in nature, involving a large number of charge carriers. This postulate opens two additional problems that need to be dealt with. First of all, electrons are fermions, meaning that two of these particles can't share the same quantum energy state at the same time. Coherence between pure electrons is therefore to be excluded. Additionally, the Coulomb repulsion will forbid their relative approach. The first to suggest a solution to this problem was Froelich in 1950 [84] and in the same year Bardeen developed independently a theory about electron-electron interaction through virtual phonon exchange [85]. The basic principle of his theory is that electrons can interact via lattice distortions (phonons) overcoming both the Coulomb repulsion and the limitations of the Fermi - Dirac statistics, since the newly-formed bound quasi-particle is a boson, and therefore capable of forming Bose - Einstein condensates. Since Bose - Einstein statistics is not limited by the Pauli exclusion principle, the particles are allowed to occupy the same quantum state and interact coherently.

2.2.2.1 Cooper pairs

An electron that passes through a lattice induces distortions by attracting the positive ions via Coulomb interaction. Since ions present a much larger inertia than electrons, this distortion will follow the electron at a distance d equal to [83]

$$d \approx v_F \frac{2\pi}{\omega_D} \approx 100 - 1000\ nm, \tag{2.39}$$

where v_F is the Fermi velocity and ω_D is the Debye frequency. This traveling deformation will attract additional electrons, since it represents a local positive polarization, boosting the electrical current and binding the charge carriers. In this way a "weak" distortion is able to overcome a much stronger Coulomb repulsion (see fig. 2.2). Electron couples bind together exchanging lattice phonons, forming the so called Cooper pairs [82]. Their binding energy 2Δ is very low, of the order of $10^{-3} - 10^{-4}$ eV, and at ambient temperature the thermal agitation

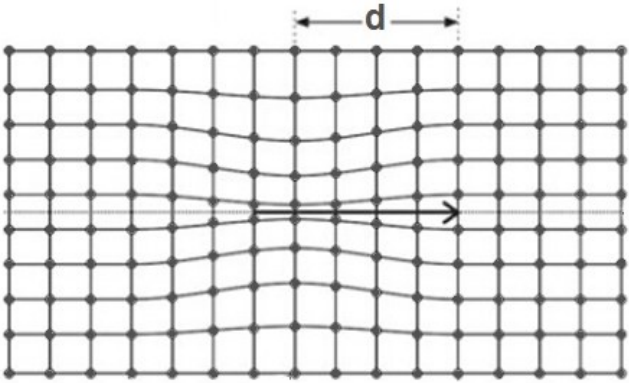

Figure 2.2: Representation of lattice deformation induced by a passing electron.

would immediately destroy them. The energy gap is a function of temperature, decreasing to zero for $T = T_C$. An explicit expression for T_C can be found by taking into consideration a quantum mechanical approach based on the density of electronic states N_0 [23]:

$$\frac{1}{N_0 V} = \int_0^{k_B \Theta_D} \frac{\tanh \frac{\sqrt{\xi^2+\Delta^2(T)}}{2k_B T}}{\sqrt{\xi^2+\Delta^2(T)}} d\xi, \tag{2.40}$$

where V is the electron - phonon interaction potential, Θ_D is the Debye temperature and ξ is the single particle energy. For $\Delta = 0$, the integration of equation 2.40 results in:

$$T_C = 1.14 \Theta_D e^{-\frac{1}{N_0 V}}. \tag{2.41}$$

In most standard superconductors $N_0 V \approx 0.3$ and $T_C \ll \Theta_D$, hence equation 2.40 simplifies to

$$\Delta(T) \approx 1.74\, \Delta(0) \left[1 - \frac{T}{T_C}\right]^{\frac{1}{2}}, \tag{2.42}$$

leading to

$$\Delta(0) = 1.76\, k_B T_C. \tag{2.43}$$

The radius r of a Cooper pair can be estimated from [83]:

$$r = \frac{\hbar v_F}{2\Delta}. \tag{2.44}$$

Assigning typical values of $\Delta = 10^{-3} - 10^{-4}$ eV and $v_F = 10^6$ m/s to the quantities inside the equation 2.44 leads to $r \sim 100 - 1000$ nm, comparable to the values for d and much larger than the typical inter-distance between electrons (~ 0.01 nm). This means that in the space occupied by a single Cooper pair hundreds of thousands of quasi-particles find place and their tendency is to align and be in phase with each other. In this way the energy of the system is minimized and at a given $T < T_C$ there will be a mixture of ground state pairs below the Fermi level and electrons occupying the levels above the energy gap.

2.2.3 Type II superconductors

The material of choice for the production of this iteration of the KIDs is a type II superconductor. Whereas purely metallic superconductors (type I) present a perfect diamagnetism, type II superconductors exhibit a more complex behavior. The distinction can be formalized under the Ginzburg-Landau theory [86] by defining a dimensionless parameter κ as the ratio between the penetration depth λ and the coherence length ξ_{GL}, that reflects the characteristic distance over which Φ, the macroscopic wave function of the superconducting state, presents changes. In a type I superconductor ($\kappa < 0.7$) the electric field penetrates to a depth $\xi_{GL} > \lambda$, since the magnetic field B is destroyed almost immediately by the diamagnetism. To each value of B a certain energy level can be associated. This, when higher than $2\Delta(T)$, determines the transition of the superconductor back to normal state. Given that the energy gap is temperature dependent, the critical (thermodynamic) magnetic field B_C will also present a similar behavior, namely [87]

$$B_C(T) = B_C(0)\left(1 - \left(\frac{T}{T_C}\right)^2\right)\left(1 + \left(\frac{T}{T_C}\right)^{2.5}\right)^{-\frac{1}{6}}, \tag{2.45}$$

with

$$B_C(0) = \sqrt{\mu_0 N_0} \cdot \Delta(0). \tag{2.46}$$

For type II superconductors the magnetic penetration depth becomes larger than the coherence length and the B field can fully enter the material in the form of quantized vortices embedded in the superconductor. To each vortex a magnetic flux quantum $\Phi_0 = \frac{h}{2e}$ generated by a normally conducting core surrounded by Meissner currents can be associated. Radius of the core and of the flux quantum are about equal to λ and ξ_{GL}, respectively. The vortices start to arise when B reaches a critical value B_{C1} up to the second critical magnetic field B_{C2}, above which the distance between vortices becomes equal to their diameter and the material transits back to normal state (cfr. Fig. 2.3). The critical fields of type II superconductors are put into relation with the thermodynamic critical field through the Ginzburg - Landau parameter, by means of the expressions:

$$B_{C1} = \frac{B_C \ln \kappa}{\kappa\sqrt{2}}, \tag{2.47}$$

$$B_{C2} = \kappa\sqrt{2} B_{C1}. \tag{2.48}$$

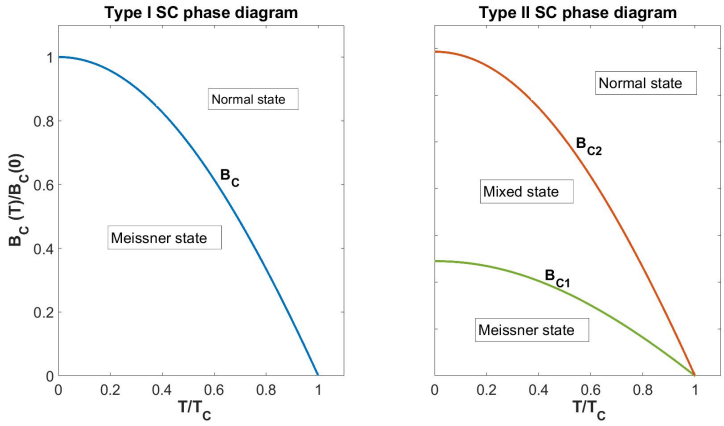

Figure 2.3: State diagrams for Type I and Type II superconductors. Meissner states refers to type I superconductors perfect diamagnetism, while mixed state involves the presence of magnetic vortices inside the film.

Increasing temperature of the type II superconductor determines an increase of the vortices' size while stronger magnetic fields determine a higher spatial density. In case of application of the superconductor in the presence of strong magnetic fields it is therefore necessary to shield the device to avoid unwanted transitions to the normal state.

2.2.4 Complex conductivity and surface resistance

Dealing with alternate currents requires taking into consideration the non-zero surface impedance rising at high frequencies. This impedance depends on the number of quasi particles (normal conducting electrons) in the superconductor. The ratio of quasi-particles n_n vs Cooper pairs n_s therefore depends on the temperature and on the frequency of the incoming radiation. Higher temperatures and higher frequencies lead to changes in the surface conductivity. Using the two fluid model the complex conductivity σ can be defined as [71]:

$$\sigma = \sigma_1 (n_n) - i (\sigma_2 (n_s) + \sigma_2 (n_n)) \tag{2.49}$$

where the real and imaginary part of the complex conductivity can be expressed, respectively, as

$$\sigma_1 = \frac{n_n e^2 \tau}{m_e (1 + \omega^2 \tau^2)}, \tag{2.50}$$

$$\sigma_2 = \frac{n_n e^2 (\omega\tau)^2}{m_e (1 + \omega^2 \tau^2)} + \frac{n_s e^2}{m_e \omega}, \tag{2.51}$$

with ω representing the frequency, τ the electron phonon relaxation time, e and m_e charge and mass of the electron. For superconducting carriers $\tau \to \infty$ (no scattering effects with the lattice), and taking into consideration the definition of London penetration depth $\lambda_L = \sqrt{\frac{m}{\mu_0 n_s e^2}}$, the total conductivity is obtained:

$$\sigma = \frac{n_n}{n}\sigma_n - i\frac{1}{\omega\mu_0\lambda_L^2(T)}, \tag{2.52}$$

where $n = n_s + n_n$ is the total charge carrier density and σ_n is the conductivity of the normal state.
At this point, the complex surface impedance for harmonic plane waves with the general expression

$$Z_s = \sqrt{i\omega \frac{\mu_0}{\sigma}} \tag{2.53}$$

can be re-written in the frame of the two-fluid model by inserting equation 2.52 into 2.53, obtaining:

$$Z_s = \sqrt{\frac{i\omega\mu_0}{\frac{n_n}{n}\sigma_n - i\frac{1}{\omega\mu_0\lambda_L(T)^2}}} = R_s + iX_s, \tag{2.54}$$

which can be approximated to

$$Z_s = \frac{1}{2}\omega^2\mu_0^2\lambda_L^3(T)\sigma_1 + i\omega\mu_0\lambda_L(T). \tag{2.55}$$

Taking the case of very thin superconducting films, where the thickness d $\ll \lambda_L$, the current density can be considered homogeneous along the film cross section and the only significant contribution to the losses come from surface scattering, reducing Z_s to [88]

$$Z_s = \frac{1}{(\sigma_1 - i\sigma_2)\, d}. \tag{2.56}$$

2.2.5 Kinetic inductance

Kinetic inductance is the manifestation of the inertial mass of mobile charge carriers in alternating electric fields as an equivalent series inductance. Kinetic inductance is observed in high carrier mobility conductors and at very high frequencies. When an electrical field in the form $E = E_0 e^{i\omega t}$ is applied to a superconductor, energy is stored in two different ways. The first one is the classical magnetic energy E_{mag} dependent on the geometry of the conductor line, while the second one is the kinetic energy of the charge carriers. Charge carriers, like all objects with mass, tend to manifest inertia undergoing acceleration, leading to a 90 deg lag between the current and the electrical field. In a superconductor, charge

carriers are composed by Cooper pairs and a temperature-dependent amount of excited quasi particles. In such cases, the kinetic inductance L_k can be calculated by equating the total kinetic energy of Cooper pairs with an equivalent inductive energy. For a wire of width w, thickness d and length l, we have [89]:

$$n_s m_e v^2 (lwd) = \frac{1}{2} L_k I^2, \tag{2.57}$$

where v is the average Cooper pair velocity, n_s is the density of Cooper pairs and I the current. Since the current can be expressed as $I = 2evn_s(wd)$, the kinetic inductance can be generally calculated as

$$L_k = \frac{m_e}{2n_s e^2} \frac{l}{wd}. \tag{2.58}$$

It is apparent then that the kinetic inductance increases as the carrier density decreases, since a smaller number of carriers must have a greater velocity than a large one to achieve the same super-current density. As the temperature increases to T_C, the Cooper pairs are progressively destroyed until no pairs are left at $T = T_C$, and losses are dominated by electron-phonon scattering. The detectors working principle is based on the change in kinetic inductance induced by an absorbed photon and the kinetic inductance fraction can be defined as $\alpha = L_{kin}/(L_{kin} + L_m)$. It follows that the detector response is directly related to α, with higher values of the factor leading to larger response. The kinetic energy of Cooper pairs varies in conjunction with the reactance of Z_s, given that their inertia is exactly what gives rise to the kinetic inductance. Therefore

$$Z_s = R_s + i\omega L_{kin} \tag{2.59}$$

and the kinetic inductance can be re-defined through equation 2.56 as

$$L_k = \frac{\sigma_2}{d(\sigma_1^2 + \sigma_2^2)\omega}. \tag{2.60}$$

2.2.6 Pippard's non-locality equations

Although Londons' treatment qualitatively accounts for the infinite conductivity, successive experimental activities, carried on mainly by Pippard [90], outlined the incapability of this theory to take into account non-local electrodynamics within the superconductor. While experimenting with indium impurities in superconducting tin, Pippard noticed how increasing the concentration of the impurities lead to larger penetration depths, while leaving the critical temperature unaltered. Basing his treatment on the non-local generalization of Ohm's law present in Chambers' paper about the anomalous skin effect [91], Pippard assumed that the current density distribution in superconductors is not determined by the local magnetic field but rather by an average value of it [92]:

$$\mathbf{j(r)} = -\frac{n_s e^2}{m_e}\bar{\mathbf{A}}_{\xi_0}(\mathbf{r}) = -\frac{1}{\mu_0 \lambda_L^2}\bar{\mathbf{A}}_{\xi_0}(\mathbf{r}), \tag{2.61}$$

with $\bar{\mathbf{A}}_{\xi_0}$ representing the vector potential averaged over a volume of radius ξ_0, which is the coherence length associated with the average value of the distance between two electrons forming a Cooper pair at T = 0. In first approximation, equation 2.61 can be re-localized by introducing an effective penetration length λ, leading to:

$$\mathbf{j(r)} = -\frac{n_s e^2}{m_e}\bar{\mathbf{A}}_{\xi_0}(\mathbf{r}) = -\frac{1}{\mu_0 \lambda^2}\mathbf{A}(\mathbf{r}). \tag{2.62}$$

At this point, depending on the relative magnitude of the ξ_0 and λ_L, we can identify two limits:

1. London or local limit: valid for $\lambda \gg \xi_0$, where we can ignore electron scattering and non-locality and the penetration depth is the one defined by London equations;

2. Pippard or non-local limit: valid for $\lambda \ll \xi_0$, leading to a larger penetration depth given by $\lambda \approx \left(\lambda_L^2 \xi_0\right)^{1/3}$.

The difference between the effective penetration depth and the London's value is an intrinsic effect of the nature of the Cooper pairs, but it is not the only one, with an important contribution coming from an extrinsic factor like the presence of

impurities in the sample. Such an increased disorder reduces the electron free path ℓ and is therefore opportune to define a new coherence length (Pippard length) ξ_P as:

$$\frac{1}{\xi_P} = \frac{1}{\xi_0} + \frac{1}{\ell}. \tag{2.63}$$

The presence of impurities limits the spatial extent to which the Cooper pairs can form, reducing the value of **j(r)** and leading to a larger λ needed to screen the magnetic field, the so called "dirty limit". Therefore, for $\ell \ll \xi_0, \ell \ll \lambda_L$ we obtain [86]

$$\lambda = \lambda_L \sqrt{\frac{\xi_0}{\ell}}. \tag{2.64}$$

Our superconductor of interest, niobium nitride, falls within this limit, since it is characterized by an electron free path in the order of angstroms [93] [94], magnetic penetration depth of hundreds of nanometers [94][95] and short coherence length of few nanometers [95][96]. This leads to a local response with a contribution of **A** reduced by a factor ℓ/ξ_0 [92]. This aspect of the nature of NbN has an impact on the values of the kinetic inductance of a thin film made with this material, given that L_k can also be expressed as [97]:

$$L_k = \mu_0 \lambda^2 \frac{l}{wd}. \tag{2.65}$$

The increased penetration depth influences the device also when used in bolometric detection mode, given that the quantum efficiency and the time response in this operation regime are heavily influenced by the value of L_k [98].

2.3 Resonator theory

A resonant circuit (also known as RLC circuit or tuned circuit) is an electrical circuit that, in virtue of the presence of an inductor (L) and a capacitor (C), oscillates at its natural resonance frequency. The resistive part (R) of the circuit results in losses and dampening over time of the oscillations. They are extensively used as tunable radio frequency receivers, as band-pass filters and as components inside frequency mixers. Assuming the presence of a voltage across the plates

of a capacitor and connecting it to an inductor, a current will flow to the latter, reducing the potential difference of the former, until no charge is present on the plates. This current flow will induce the build up of a magnetic field around the inductor. At this point, all the energy that was stored in the capacitor electric field has been transferred to the inductor magnetic one, as per Faraday's law of induction [99]:

$$\Phi = \iint_{\Sigma} \boldsymbol{B}(\boldsymbol{r}, t) \cdot dA, \tag{2.66}$$

where Σ is the surface bound by the inductor solenoid and dA its surface element. The current flow will not stop once the charge on the capacitor plates is completely depleted, but according to the Lenz law,

$$\mathcal{E} = -\frac{\partial \Phi}{\partial t}, \tag{2.67}$$

an electromotive force (and therefore, a current) opposite to the one that charged the inductor will rise, once the magnetic field starts to decrease in intensity. This opposite current will charge the capacitor with polarity opposite to the original one, and the cycle will repeat again. The oscillation will last indefinitely in the absence of resistive effects or will be damped to zero in the real case of non ideal conductors, at angular frequency

$$\omega_0 = \frac{1}{\sqrt{LC}}. \tag{2.68}$$

If the circuit is supplied with an AC current of angular frequency equal to that of its natural oscillation, a resonance condition is reached. The energy stored in the resonator can be express by [71]:

$$E_{res} = \frac{1}{2} C V^2 = \frac{1}{2} L I^2, \tag{2.69}$$

while the dissipated power is defined as

$$P_{res} = \frac{1}{2} \frac{V^2}{R} = \frac{1}{2} R I^2. \tag{2.70}$$

The resonant circuit can either be in a parallel or series configuration (cfr. fig 2.4). From the Kirchoff law we obtain the impedance for both parallel and series configuration circuits when they are supplied an AC current at angular frequency ω :

$$Z_p = \left(\frac{1}{R} + \frac{1}{i\omega L} + i\omega C \right)^{-1} \tag{2.71}$$

$$Z_s = R + i\omega L + \frac{1}{i\omega C}. \tag{2.72}$$

The resonance frequency is defined as that frequency at which the inductive and the capacitive reactance have the same value, i.e. the resonance condition imposes that $\mathrm{Im}\{Z_{in}\} = 0$. Apart from their natural resonance frequency, resonators are characterized also by the quality factor Q, describing how many ohmic losses dampen the oscillations, and is defined as:

$$Q = \omega_0 \frac{E_{res}}{P_{res}}, \tag{2.73}$$

which in the parallel resonant circuit becomes

$$Q_p = \omega_0 RC = \frac{R}{\omega_0 L}, \tag{2.74}$$

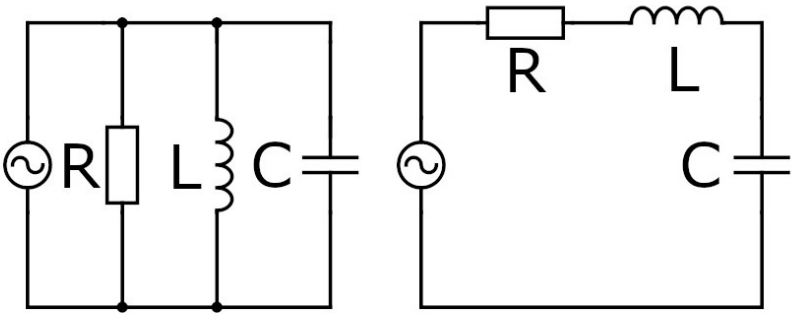

Figure 2.4: Parallel (left) and series (right) resonant circuits.

while in the case of series resonator,

$$Q_s = \frac{\omega_0 L}{R} = \frac{1}{\omega_0 RC}. \tag{2.75}$$

As already stated, KIDs are coupled to an external single feedline that adds an external impedance Z_{ext}. The KID in development for this work is of the Lumped Element type and it can be modeled, in first approximation, as a series resonator (see fig. 2.5). The presence of the external impedance (coupling impedance) leads to the definition of a loaded quality factor Q_L as

$$\frac{1}{Q_L} = \frac{1}{Q_0} + \frac{1}{Q_C}, \tag{2.76}$$

with Q_0 and Q_C quality factors associated with, respectively, the resonator and the coupled external feedline. The quality factors can be derived from the measured scattering parameter S_{21} and, given that $\nu = \frac{\omega_0}{2\pi}$, they can be redefined as

$$Q_L = \frac{\nu_{res}}{\Delta\nu_L} \tag{2.77}$$

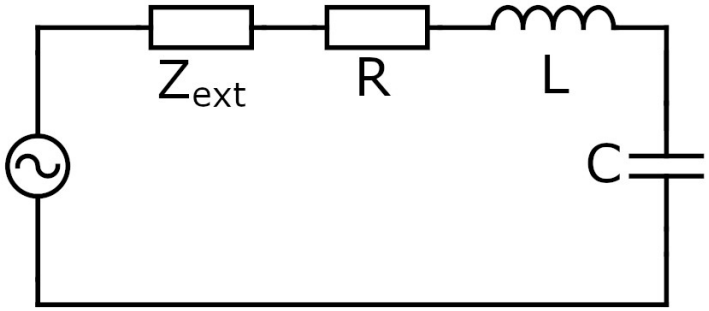

Figure 2.5: Schematic representation of the equivalent circuit for a KID coupled to an external feedline.

$$Q_0 = \frac{\nu_{res}}{\Delta\nu_0}, \tag{2.78}$$

where $\Delta\nu_L$ and $\Delta\nu_0$ are the half power bandwidths for, respectively, the coupled and uncoupled resonators. Inside these frequency ranges, the energy of the resonators is at least half of the peak energy. According to [100] and [101], the correct values of the parameter S_{21} where the bandwidths present in equations 2.77 and 2.78 have to be taken can be calculated as

$$S_{21,L} = \sqrt{\frac{1 + |S_{21,min}|^2}{2}} \tag{2.79}$$

and

$$S_{21,0} = |S_{21,min}| \sqrt{\frac{2}{1 + |S_{21,min}|^2}} \tag{2.80}$$

with $|S_{21,min}|$ taken at the resonant frequency (see fig. 2.6). The coupling factor κ between the transmission line and the resonator can be defined as:

$$\kappa = \frac{|S_{11,max}|}{|S_{21,min}|} = \frac{1 - |S_{21,min}|}{|S_{21,min}|}, \tag{2.81}$$

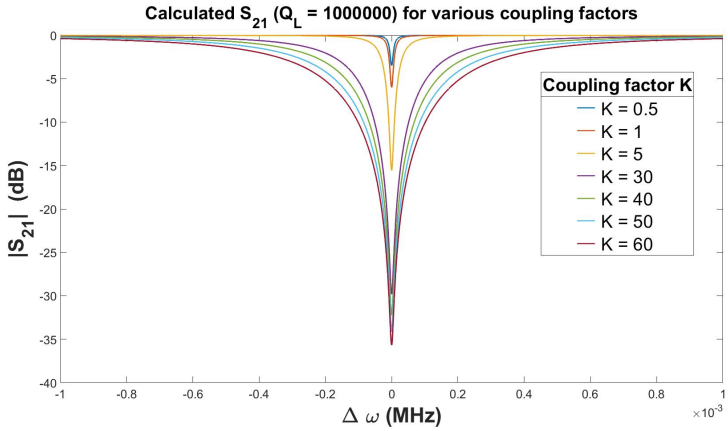

Figure 2.6: Calculated transmission scattering parameter for a fixed quality factor. Higher coupling factor results in deeper and wider dips.

where $|S_{11,max}|$ is the reflection scattering parameter at the resonance frequency. The quality factors can be re-expressed in terms of κ as:

$$Q_0 = Q_L(1+\kappa) = \frac{Q_L}{|S_{21,min}|}, \tag{2.82}$$

$$Q_C = \frac{Q_0}{\kappa} = \frac{Q_L}{1-|S_{21,min}|}. \tag{2.83}$$

A complete set of relations between Q_C, Q_0, Q_L and the scattering parameter $S_{21,min}$ has been obtained. For high coupling factor ($|S_{21,min}| \ll 1$), Q_0 becomes very large and $Q_C \approx Q_L$. In the opposite case, when $|S_{21,min}| \approx 1$, $Q_C \to \infty$ and $Q_L \approx Q_0$, resulting in a very sharp resonance curve. The whole detector performances can be therefore tuned by acting on κ, optimizing the overlapping of adjacent resonance frequencies with the saturation threshold.

2.4 Noise figures of KIDs

Two main noise mechanisms in KIDs can be identified: one arises from the statistical fluctuations in the charge carrier densities for temperatures above the absolute zero (generation-recombination noise, or GR) and the other one is related to the photon power impinging on it (shot noise). In order to estimate these two figures, a few other quantities need to be defined.

2.4.1 Quasi-particles excitations

The number density of thermally excited quasi particles $n_n(T)$ is defined as [74]

$$n_n(T) = 2N_0\sqrt{2\pi k_B T\Delta(0)}e^{\frac{-\Delta(0)}{k_B T}}, \tag{2.84}$$

Eq. 2.84 doesn't account for the absorption of photons with $E > 2\Delta$ and the related excited quasi-particles, that result from the breaking down of Cooper pairs. In the latter case, the number of quasi-particles increases until a new dynamic

equilibrium between number of Cooper pairs generated and destroyed is attained. The quantity associated with this phenomenon is the quasi-particle lifetime τ_{qp}, an estimation of the temporal scale of the aforementioned process. From Kaplan et al. [102] a theoretical value for τ_{qp} can be calculated as:

$$\tau_{qp} = \frac{\tau_0}{\sqrt{\pi}} \left(\frac{k_B T_C}{2\Delta} \right)^{\frac{5}{2}} \left(\frac{T_C}{T} \right)^{\frac{1}{2}} e^{\frac{\Delta}{k_B T}}, \tag{2.85}$$

with τ_0 dependent on the material, and of the order of 10 ps for niobium nitride [103]. The quasi-particles life time can be expressed in terms of quasi particles density n_n by combining equation 2.85 and 2.84, leading to

$$\tau_{qp} = \frac{\tau_0}{n_n} \frac{N_0 (k_B T_C)^3}{2\Delta^2}. \tag{2.86}$$

Quite intuitively, τ_{qp} is inversely proportional to the quasi particle density. Given that the detector will be under constant illumination from photons with $E > 2\Delta$, there will be an excess of quasi-particles present in the super conductor. The number of quasi particles generated by Cooper pair breaking photons can be estimated as

$$N_{qp(\gamma)} = \frac{\eta P_\gamma \tau_{qp}}{\Delta}, \tag{2.87}$$

with P_γ and η representing, respectively, the optical power impinging on the detector and the photon absorption efficiency factor.

2.4.2 Generation-recombination noise

The GR noise represents the fundamental lower noise limit for KIDs and is determined by statistical fluctuations in the number of quasi-particles and Cooper pairs densities that occur at T > 0. From [101]

$$NEP_{gr} = 2\Delta \sqrt{\frac{N_{qp}}{\tau_{qp}}} \propto e^{\frac{-\Delta(0)}{k_B T}}, \tag{2.88}$$

which is proportional to the square root of the number of quasi particles. Given the dependencies expressed by the equations 2.84, 2.86 and 2.87, the GR noise can be reduced either by lowering the temperature at which the detectors are operated or decreasing the volume of the superconductor. From equation 2.58 it is also apparent that the reduction in volume will inevitably lead to an increase of the kinetic inductance and, therefore, to a higher responsivity of the detector. Typical GR noise values for KIDs operated in the astrophysical fields can be as low as $10^{-18}W/\sqrt{Hz}$, with the record being, to date, $3 \cdot 10^{-19}W/\sqrt{Hz}$ for a 50nm thick aluminum film [65].

2.4.3 Shot noise

The GR noise doesn't take into consideration the noise generated by the incoming photons that generally represents the dominating noise mechanism. The photons that impinge on the detector come from both the source and the background and given the extremely noisy background represented by a nuclear fusion plasma, an appropriate band pass filter will be employed to cut the radiation down to a narrow bandwidth centered on the probing frequency. A rough estimation of the shot noise can be calculated with the expression [71]

$$NEP_\gamma \approx \sqrt{4h\nu P_\gamma}. \tag{2.89}$$

If $\nu = 1.3$ THz and a total power of 0.01 mW are chosen, a NEP of roughly $1.8 \cdot 10^{-13}\ W/\sqrt{Hz}$ is obtained, which is much larger than the GR noise and represent the physical limit for the noise of the KIDs.

3 KID Design and Optimization

In the following chapter the design criteria, the simulations and the numerical studies of the detectors are presented. These studies were performed in order to tailor the devices to the foreseen application and to establish a baseline of parameters to be later employed during the production and test of the devices. The investigations carried on include an evaluation of the expected Faraday rotation for plasma scenarios directly extracted from data collected in the ASDEX Upgrade machine [39] and an estimation of the plasma absorbance of the probe beam. Simulations by means of the Sonnet EM simulation suite [26] were performed for impedance matching and detector frequency tuning purposes, for investigating the occurrence of cross-talk between pixels and for studying the coupling of the pixels to the transmission line.

3.1 Plasma density profiles analysis

KIDs must be tuned to the appropriate detection band in order to insure optimal performances. An analysis of plasma-density profiles, which were provided by the team at ASDEX Upgrade (AUG) [17, 39], was performed to determine the optimal probing frequency. The amount of rotation induced on radiation of various wavelengths under different conditions was estimated: given the strong dependency of the Faraday effect on ω (eq. 2.24), it is important to strike a good balance between a wide angular dynamic range and avoidance of rotation angles exceeding $\pi/2$, which would require the usage of phase analysis techniques to discern partial rotations from complete ones [19]. Additionally, one has to consider the competing Cotton - Mouton effect, which arises from the magnetic field components perpendicular to the beam (toroidal field), which scales with

λ^3 and modifies the ellipticity of the beam [3]. Therefore, angles not too large are desirable, otherwise the measured changes in polarization are difficult to interpret, due to the simultaneous influence of the two effects. Two different densities profiles were provided, a 'low' density one, with a maximum value for n_e equal to $3 \cdot 10^{19}\ m^{-3}$ (Fig. 3.1) and 'high' density one, with a maximum value of $9 \cdot 10^{19}\ m^{-3}$ (Fig. 3.2), while a third 'mid' one was calculated by averaging

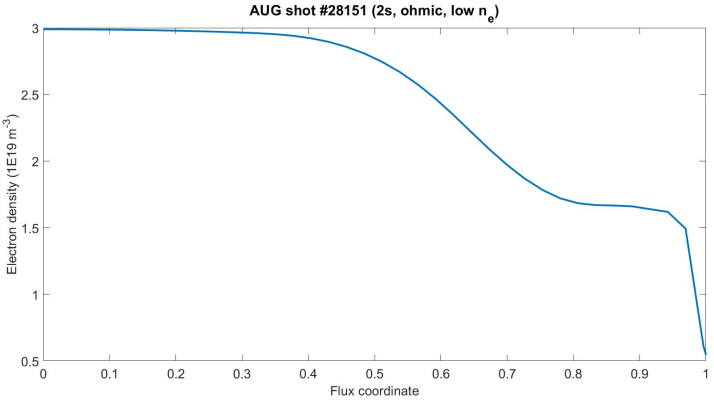

Figure 3.1: 'Low' density profile in an ASDEX UPGRADE (shot nr 28151, 2s, ohmic).

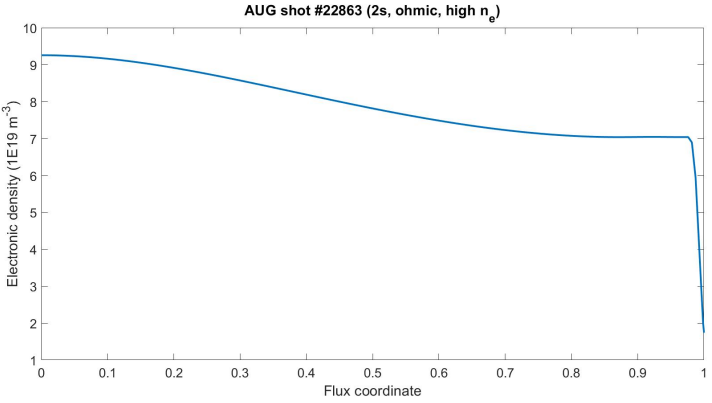

Figure 3.2: 'High' density profile in an ASDEX UPGRADE (shot nr 22863, 2s, ohmic).

the first two. The radial profile of the parallel component of the magnetic field completed the datasets required to run the calculations of the Faraday rotation (Fig. 3.3). It can be seen that the magnetic field is anti-symmetric with respect to the midplane (Z=0), therefore equal but opposite Faraday rotations above and below the central line-of-sight are expected. The Faraday angles were calculated at probing frequencies of 1.3, 1.6 and 1.8 THz, corresponding to 230.6, 187.3 and 166.5 μm wavelengths, respectively (Fig. 3.4). These frequencies were chosen since they lie close to what is used in current polarimetric systems. Additionally, as a cross reference value of the rotation, the AUG DCN polarimeter operating at 195 μm was taken, with roughly a 10 degrees angle expected for a beam passing through the plasma just above the mid-plane [17]. Results of the analysis are summarized in Table 3.1. The low densities regime leads to small angles

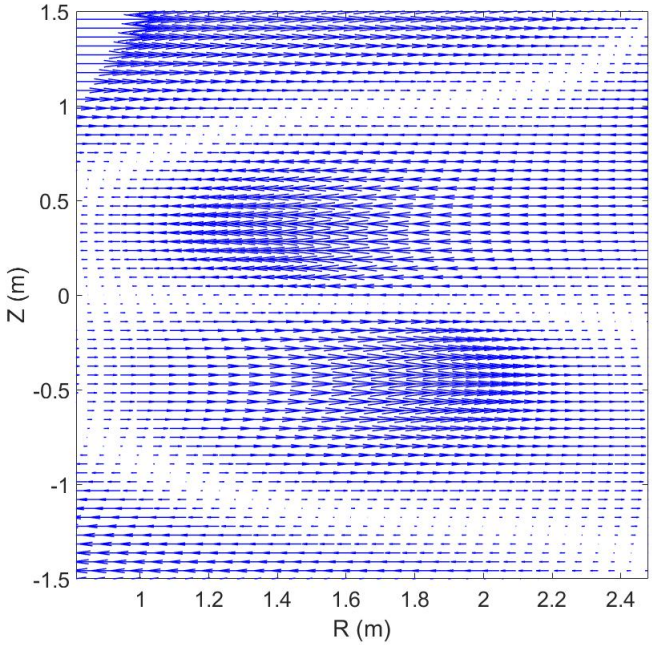

Figure 3.3: Radial profile of the parallel component of the magnetic field in ASDEX Upgrade.

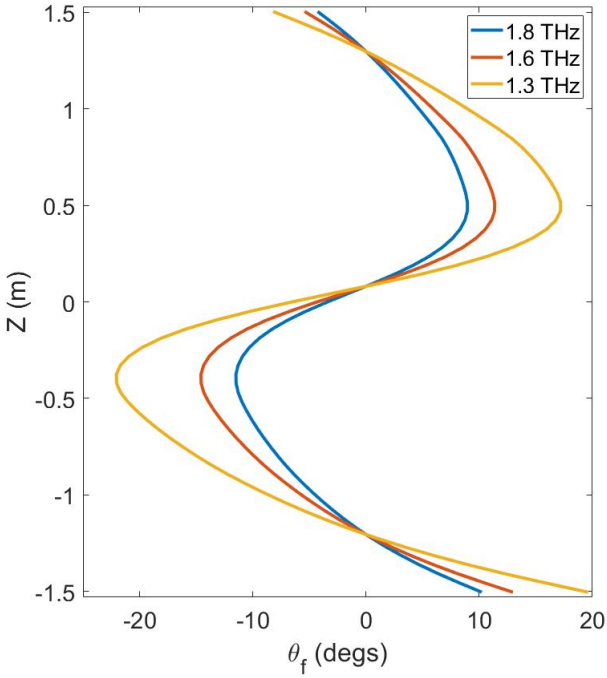

Figure 3.4: Faraday rotation angle along the whole plasma cross-section for three different probing wavelengths for the high density plasma profile.

for the 1.6 and 1.8 THz beams, with values of rotations in the order of 3-5 degrees. At average- and high-density profiles, rotations are still well inside the 90 degrees limit, with a maximum value of about 22 for 1.3 THz. Additionally, the polarimeter is expected to operate at first on small- to medium-size machines, with plasma densities closer to the low- and mid-profile values. Taking into account the necessity to maximize the dynamic range, the KIDs were optimized for the 1.3 THz bandwidth, expecting maximum rotation values in the order of 10-15 degrees once implemented in the machine.

Table 3.1: Faraday rotation angles for low- (LD), mid- (MD) and high-density (HD) profiles.

Frequency	LD	MD	HD
1.3 THz	6.5/-7.3 degs	13/-14 degs	19.6/-22 degs
1.6 THz	4.3/-4.8 degs	8.6/-9.7 degs	12.9/-14.6degs
1.8 THz	3.4/-3.8 degs	6.8/-7.7 degs	10.2/-11.5 degs

3.1.1 Plasma absorption

As a general rule, electromagnetic waves can propagate through an ionized gas given that their frequency is higher than the plasma frequency ω_p (Eq. 2.13), which is a function of the electron density n_e [76]. Pulses with frequencies in the range from 0.1-10 THz can propagate through densities between 10^{19} and 10^{24} m^{-3}, a range that fully covers what can be found in typical fusion applications. In order to estimate the power impinging on the detectors, it is important to evaluate how much radiation is absorbed by the plasma at different values of n_e. Yuan et al. [104] introduced a detailed model for propagation of THz waves in magnetized plasma that was taken as basis for the following analysis. The adopted plasma physical model is composed by a plasma slab of thickness d bound at $z = 0$ by a perfectly transparent lossless plate and at $z = d$ by a perfectly conducting wall. The plasma is immersed in an external magnetic field B, parallel to the z direction, which is also the propagation direction. The radiation is circularly polarized, the dielectric constant expression for a warm magneto plasma will be adopted, namely

$$\epsilon = \frac{\left[1 - \frac{\omega_p^2}{\omega(\omega - i\nu_e \pm \Omega)}\right]}{\left[1 - \frac{\omega\omega_p^2}{(\omega - i\nu_e \pm \Omega)^3}\frac{k_B T}{mc^2}\right]}, \tag{3.1}$$

where ω_p is the plasma frequency, $\Omega = \frac{eB}{m_e c}$ is the electron cyclotron angular frequency, ν_e the electron collisional frequency and $\pm$ identifies right- and left-handed waves. Within these premises, the absorption A is derived by the power balance relation

$$A = 1 - R, \tag{3.2}$$

where

$$R = \left| \frac{\tanh(i2\pi\nu d\sqrt{\epsilon}/c) - \sqrt{\epsilon}}{\tanh(i2\pi\nu d\sqrt{\epsilon}/c) + \sqrt{\epsilon}} \right|^2 \tag{3.3}$$

is the reflection coefficient and ν represents the temporal frequency of the probing beam. Since a linearly polarized wave can be thought as the sum of two contra-rotating circularly polarized waves, the total absorption was calculated as an average between its left- and right-handed components. The calculation was performed taking as reference ASDEX - Upgrade typical operational parameters for the cyclotron frequency Ω (140 GHz), collisionality ν_e (10 GHz), electron temperature T_e (10 keV), and a plasma length l of 1 m. The absorption for the 1.3 THz probe beam is plotted in fig. 3.5 against the electron density together with the analogous parameter for the deuterium cyanide (DCN) laser installed at AUG and operating at 1.53 THz. It can be seen from fig. 3.5 that A varies between 0.14

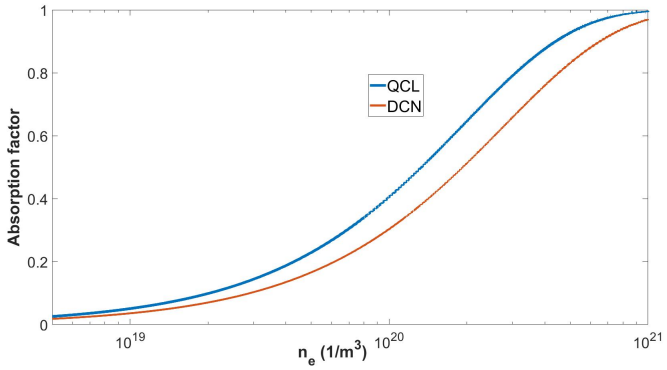

Figure 3.5: Calculated absorption factor as a function of electron density n_e for a QCL (1.3 THz) and DCN laser (1.53 THz) passing through a magnetized ASDEX-like plasma, assuming T_e = 10 keV, ν_e = 10 GHz, ν_c = 140 GHz, l = 1 m.

for a density of 10^{19} m^{-3} and 0.4 for 10^{-20} m^{-3}. Supposing the initial power of the probing beam to be of the order of 0.1 mW [20], it can be expected around 10^{-5} W impinging on the detector, once other losses given by the transmission of the beam through waveguides and its divergence are taken into account.

3.2 KIDs design

A single detector is composed of four LEKID sub-units arranged in a cross-configuration, patterned at 90 degree rotations from each other (Fig. 3.6). The whole detector measures roughly 5x5 mm^2, including the contact pads. Each polarization direction is detected by a pair of diagonally opposed sub-units, resulting in dual polarization sensitiveness and compact dimensions. Each sub-unit is itself a detector, composed by an inductive part (the meandering lines in fig. 3.6) shared among all the pixels and a tunable inter-digital capacitor. Several samples were prepared with a metallization also on the rear side of the substrate in the form of a 400 nm thick layer of Nb or Au, that functioned as both ground plane for the microstrip feedline above and as backshort. This 2x2 configuration

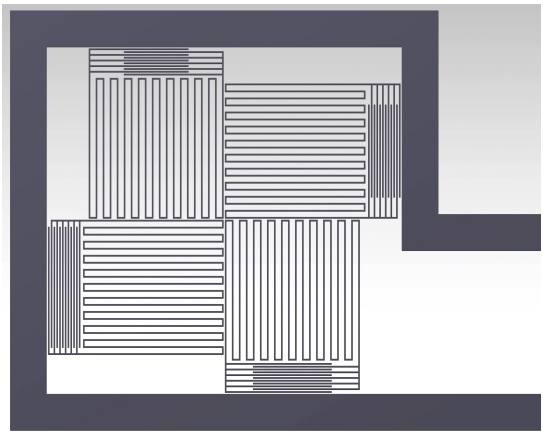

Figure 3.6: CAD rendering of the KID unit. The four LEKID sub-units arranged in cross configuration are visible in the center of the image, and they are surrounded by the feedline.

serves two main purposes, namely to simplify beam alignment and obtain polarization sensitiveness. As it will be shown later in section 3.3.3, the detectors are sensitive mainly in their inductive part, with the capacitors giving much lower contributions. Such configuration makes it possible to obtain uniform illumination of the resonators by simply centering a Gaussian probing beam on the central point of the "cross" formed by the various sub-units adjacent sides. Polarization sensitiveness is obtained in virtue of the orientation of the inductive meandering line. As described later in section 5, such simple solution is effective in avoiding cross polarization detection, since the short segments of NbN film connecting the long ones are small enough that the contribution deriving from the perpendicular polarization is not significant.

3.2.1 Optical impedance matching

The first step to optimize the devices to our application was the study of the coupling between radiation and the detector itself. In particular, two kinds of configurations were investigated, with and without backshort. For this purpose, two simplified models taken from Shu et al. [24] and from Driessen et al. [105] were employed. These models made it possible to study and optimize the matching of the detector impedance to that of free space radiation ($Z_0 = 377\ \Omega$) through the choice of proper geometrical parameters of the device and also to estimate the absorption factor.

3.2.1.1 With backshort

The backshort's function is to reflect back through the substrate waves that are not absorbed by the superconductor at the first passage in the detector, improving the detection efficiency and additionally narrowing down the detection bandwidth. One fundamental parameter when studying such problem is the impedance Z_{KID} of the device, which is defined as

$$Z_{KID} = \frac{1}{\frac{1}{Z_{SC}} + \frac{1}{Z_{Sub}}}, \tag{3.4}$$

with

$$Z_{SC} = \frac{\rho_{NbN} \cdot s}{d_{NbN} \cdot w} \tag{3.5}$$

representing the impedance of the structures forming the detector and

$$Z_{Sub} = iZ_{Eff} \tan(\beta l) \tag{3.6}$$

as the substrate impedance. The parameter w is the width of the NbN tracks, d_{NbN} is the thin film thickness while s indicates the separation between two adjacent lines in the inductive section (Fig. 3.7), while the NbN film properties are represented by the resistivity. The adopted values for these quantities are 120 $\mu\Omega$·cm for ρ_{NbN}, 10 and 40 μm for w and s respectively, and 15 nm for d_{NbN}. On the substrate side, $Z_{Eff} = Z_0/\sqrt{\epsilon_r}$ is the substrate effective impedance, $\beta = 2\pi/\lambda_{Eff}$ is the effective wavenumber of the probe radiation, and l is the thickness of the substrate. Given the presence of the backshort, the latter quantity

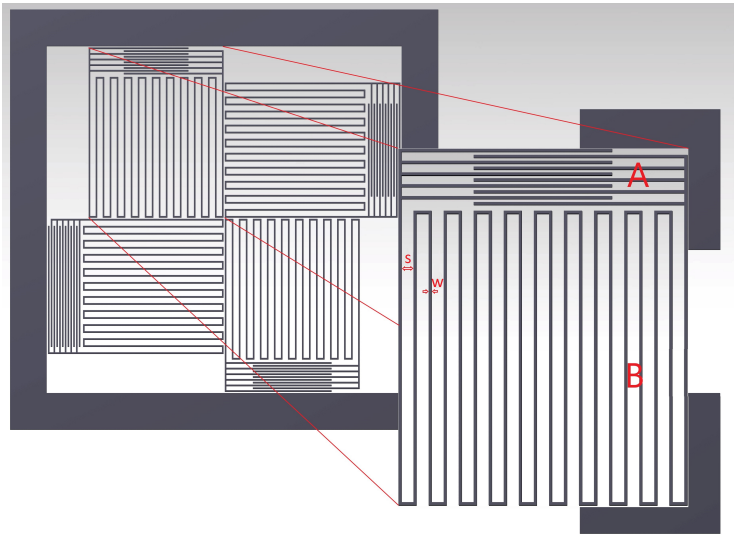

Figure 3.7: CAD rendering of a KID single pixel resonator unit. A and B indicate the capacitor and the inductor, respectively, s represents the separation between two adjacent meandering lines and w is their width.

is chosen to be equal to an odd number of quarters of the effective wavelength to maximize the absorption of radiation:

$$l = \frac{2n+1}{4}\lambda_{Eff}; \quad \lambda_{Eff} = \lambda/\sqrt{\epsilon_r}. \tag{3.7}$$

The detector absorption A is then calculated by means of the following expression [24]

$$A = 1 - \left|\frac{Z_0 - Z_{KID}}{Z_0 + Z_{KID}}\right|^2. \tag{3.8}$$

The backshort distance can be effectively used to select the detection central wavelength, together with the choice of substrate. The values of A for each of the materials studied are plotted vs the thickness of the substrate. As can be seen in the figures 3.8, 3.9 and 3.10, the absorption plotted against the backshort distance is periodic, with several values of the substrate thickness maximizing it. The actual value needs to be chosen by taking into consideration both the mechanical stability of the device and the occurrence of so called substrate events [106]. Since silicon is non transparent, a fraction of the incoming photons that passes through the superconducting thin film can be absorbed by the substrate, generating phonons. Scattering back toward the superconductor, they can break additional Cooper

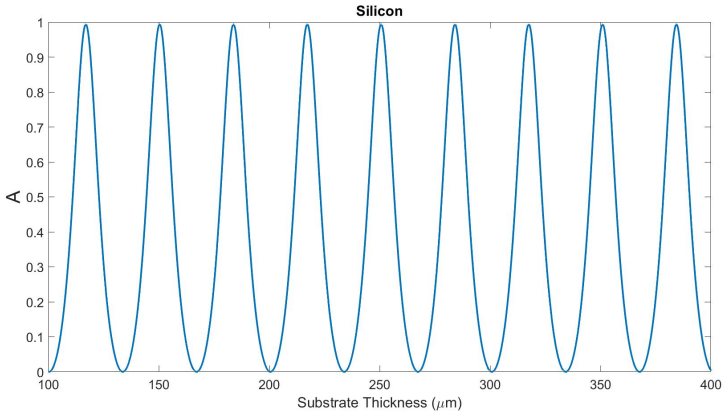

Figure 3.8: Detector absorbance factor A versus the substrate thickness for silicon.

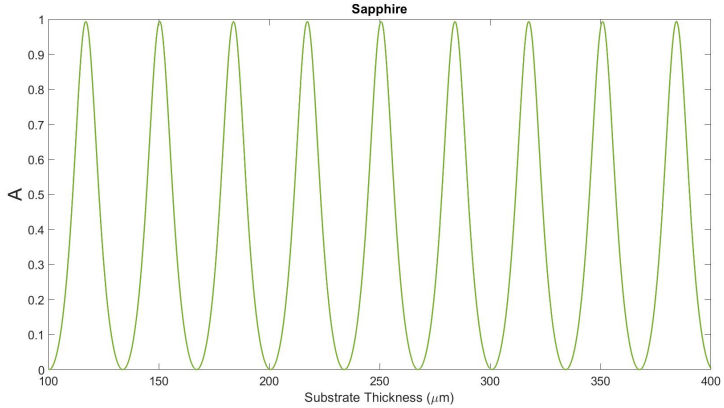

Figure 3.9: Detector absorbance factor A versus the substrate thickness for monocrystalline sapphire.

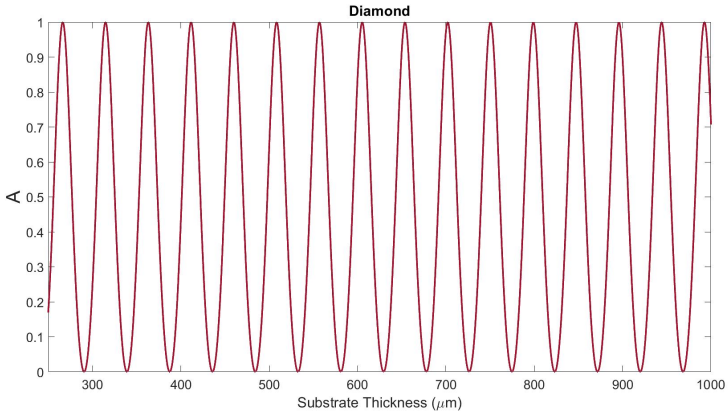

Figure 3.10: Detector absorbance factor A versus the substrate thickness for policrystalline diamond.

pairs, creating false signals. The use of transparent materials like sapphire and diamond can limit this issue. These materials present a much lower loss tangent compared to silicon, with values around 10^{-7} for monocrystalline sapphire and 10^{-5} for policrystalline diamond [107], versus a value around $4 \cdot 10^{-4}$ for silicon.

Diamond is also of particular interest for our application, given its radiation hardness.

3.2.1.2 Without backshort

The starting point of the model we used for the chips that lacked backshort is the absorption of a film with thickness d and complex dielectric constant ϵ_2, sandwiched between two dielectric layers with refractive indices N_1 and N_3, respectively, with the illumination on the thin film coming from the N_1 side. In general, the optical impedance of a medium can be defined as:

$$Z_i = \frac{Z_0}{N_i}, \tag{3.9}$$

which is equivalent to the equation for Z_{Eff} given in the previous section. The reflection R and transmission T coefficients can be defined as

$$R = \left| \frac{Z_{tot} - Z_1}{Z_{tot} + Z_1} \right|^2 \tag{3.10}$$

and

$$T = \frac{Z_1}{Z_3} \left| \frac{2Z_{tot}}{Z_{tot} + Z_1} \right|^2, \tag{3.11}$$

with Z_{tot} combining the impedance of the film and of the substrate. The absorption is simply given by the formula

$$A = 1 - R - T. \tag{3.12}$$

Assume that the film is thin enough to neglect interference effects (namely, $k_0 d \ll 1$), the total impedance can be written as:

$$Z_{tot} \approx \frac{R_\square Z_3}{R_\square + Z_3}, \tag{3.13}$$

with $R_\square \approx Z_0/k_0 d\ \mathrm{Im}[\epsilon_2]$ the sheet resistance for a highly absorbing ($\mathrm{Im}[\epsilon_2] \gg \mathrm{Re}[\epsilon_2]$) medium, while k_0 is the vacuum wave vector of the probing light. Table 3.2 summarizes the transmission, reflection and absorption factors calculated from the values of $R_\square$ recorded in the measurements described in section 5.1. Table 3.2 includes also samples with depositions of NbN thin films of 5 and 30 nm performed on sapphire substrates. The additional thicknesses were deposited to investigate the change in behavior of the detectors for different kinetic inductance values.

Table 3.2: Absorption, transmission and reflection coefficients of backshort-less detectors. The values of the sheet resistance $R_\square$ and refractive index N are also given. Sa-NbN, Si-NbN and Di-NbN refer to sapphire, silicon and diamond substrates respectively, with NbN films deposited at the specified thickness.

Sample	$R_\square$ ($\Omega/\square$)	N	A	T	R
Sa - NbN 15 nm	70.6	1.78 [105]	0.3240	0.1080	0.5681
Sa - NbN 5 nm	273.51	1.78 [105]	0.3188	0.4117	0.2694
Sa - NbN 30 nm	33.5	1.78 [105]	0.2286	0.0362	0.7353
Si - NbN 15 nm	220.6	3.41 [108]	0.1824	0.3637	0.454
Di - NbN 15 nm	118.3	2.378 [109]	0.2958	0.2207	0.4835

3.2.2 Electrical impedance matching

Read-out electronics have a standard impedance of 50 Ω that has to be matched by the detector to avoid signal reflections at the bonding locations. The microstrip feedline responsible for exciting and extracting the signal from the devices must be properly sized. For this purpose, a method based on the Wheeler's formula [110] modified by Hammerstad [111] was employed for the initial estimation of the impedance of the microstrip:

$$Z_{ms} = \begin{cases} \frac{Z_0}{2\pi\sqrt{\epsilon_{eff}}} \ln\left(8\frac{l}{w_{ms}} + \frac{w_{ms}}{4l}\right), & \text{when} \quad \frac{w_{ms}}{l} \leq 1 \\ \frac{Z_0}{\sqrt{\epsilon_{eff}}\left[\frac{w_{ms}}{l} + 1.393 + 0.667\ln\left(\frac{w_{ms}}{l} + 1.444\right)\right]}, & \text{when} \quad \frac{w_{ms}}{l} \geq 1 \end{cases} \tag{3.14}$$

with l the substrate thickness and w_{ms} representing the width of the microstrip line. The silicon detectors were initially designed for a substrate thickness of 250 μm in order to maximize the optical absorption. This lead to a 200 μm wide microstrip, corresponding to an input impedance of 49.83 Ω. At the time of production of the samples the only available substrates were 330 μm thick, resulting in a larger input impedance of 56.11 Ω. On the other hand, sapphire and diamond substrates were available in 330 and 700 μm thicknesses respectively, leading to microstrip widths of 320 and 850 μm and corresponding to impedance values of 49.33 Ω for the sapphire and 53.3 Ω for diamond.

3.3 Electro-magnetic simulations

In the following section, the simulations performed to estimate the response of the detectors to a broadband excitation signal are presented. The tool used is the Sonnet EM software suite [26], and the calculations performed include the broadband analysis of the impedance matching of the feedline, investigating the tuning of the resonance frequency, studying of cross-talk, estimation of the coupling factor between resonators and feedline and, last but not least, simulations of the complete detectors. The results relative the the broadband impedance refer to both 250 μm and 330 μm silicon substrates in addition to the sapphire and diamond ones, while for the rest of the broadband analysis only the results relative to the prototypes later produced (silicon and sapphire both 330 μm thick and diamond 700 μm) are presented.

3.3.1 Transmission line broadband impedance

An analysis of the impedance of the transmission line was performed via Sonnet to study its broadband behavior. Both the 250 and 330 μm silicon substrates were simulated, beside the sapphire (Sa330) and diamond (Di700) ones. The results are reported in fig. 3.11, from which it can be seen that the impedance mismatch of the incorrectly-sized microstrip on the 330 μm silicon substrate increases rapidly with the frequency. The input impedance at 0.8 GHz is 55 Ω and it increases to around 60 Ω at 1.1 GHz, which is the upper frequency limit for pixels on the 330 μm silicon substrate. The increase in impedance with respect to the case of a microstrip with the same width on the 250 μm thick Si substrate is roughly between 10 and 25%, and it will lead to the formation of standing waves trapped inside the microstrip. On the other hand, sapphire and diamond are well matched up along the whole frequencies spectrum.

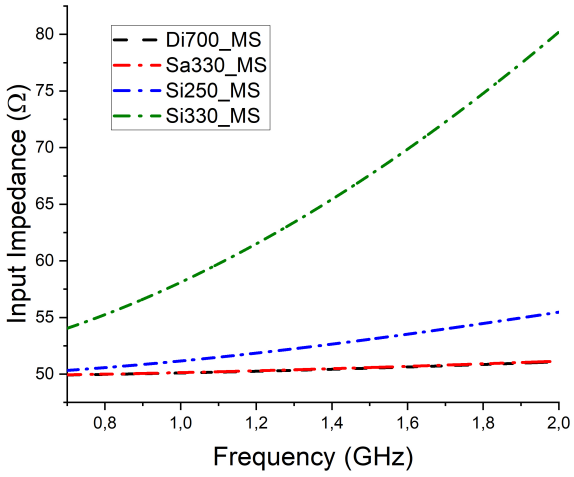

Figure 3.11: Impedance of the microstrip feed-lines for silicon (blue and green lines for 330 and 250 μm, respectively), sapphire (red) and diamond (black) substrates, simulated with Sonnet. Red and black lines overlap.

3.3.2 Resonance frequency

One of the big advantages of KIDs when compared to other technologies, is the possibility to excite the resonators and read their output with a single feedline using frequency division multiplexing (FDM) [21]. In such techniques, the total bandwidth available is divided into non overlapping frequency bands, each one corresponding to a separate signal. In this way multiple signals can share a single conductor and still be read independently. In the case of KIDs, the signals source is the oscillation of the single pixels, and it is therefore necessary to tune each one of them to its own bandwidth. The resonance tuning is performed through modifications of the capacitive section (labeled as A in fig. 3.7), leaving the inductive part (B in fig. 3.7) unaltered. The interdigital capacitors in the single pixels are composed by a number of fingers comprised between 10 and 12, with lengths between 700 and 900 μm that vary in 50 μm steps. The results are visible in figures 3.12, 3.13 and 3.14 for 15nm thick NbN films on the three substrates considered. With the geometrical parameters of the resonators fixed, the resonance frequencies are determined by the permittivity of the substrate

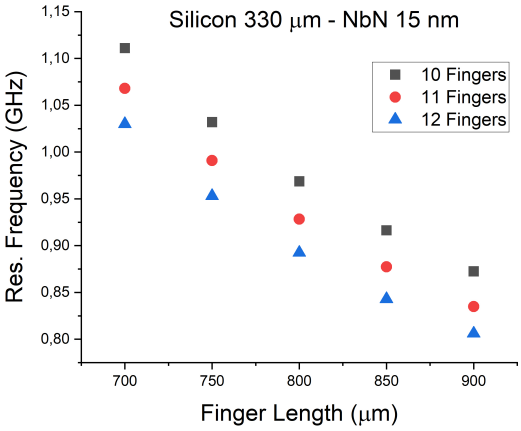

Figure 3.12: Single pixels resonance frequencies, as simulated with Sonnet Software - silicon substrate, 15 nm NbN layer.

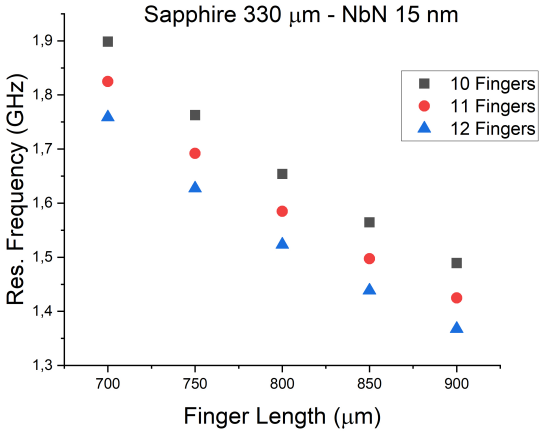

Figure 3.13: Single pixels resonance frequencies, as simulated with Sonnet Software - sapphire substrate, 15 nm NbN layer.

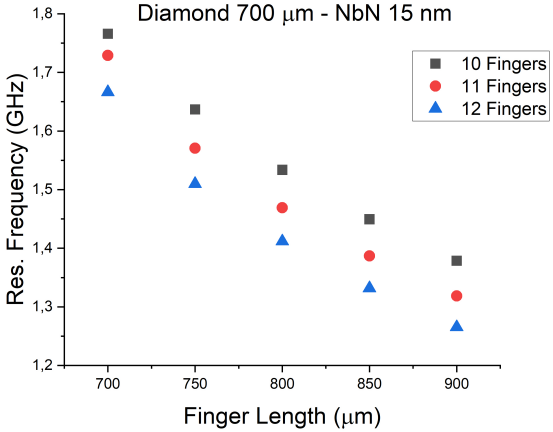

Figure 3.14: Single pixels resonance frequencies, as simulated with Sonnet Software - diamond substrate, 15 nm NbN layer.

materials for the capacitive part of the detector, and by the kinetic inductance associated to the film for the inductive part. Values of the permittivity equal to 11.9 and 5.67 were assumed in the simulations for silicon [108] and diamond [109], respectively. Sapphire is naturally birefringent, with values of ϵ_r equal to 9.3 in the x and y directions and 11.5 along the z direction. The sapphire substrates employed in this work where cut along the r-plane, resulting in an angle of 57.6 degrees between the z direction and the axis perpendicular to the cutting plane. It is therefore possible to define an "isotropized" effective permittivity, relative to an equivalent isotropic substrate that provides the same electrical characteristic as the original anisotropic one, as described by Vendik et al. [112]. The resulting value of the permittivity is then taken as 10.06. The kinetic inductance of the thin films was estimated from the first characterization measurements (see section 5) using the model found in reference [113]. From the simulations it can be seen that the silicon substrate detectors present the lowest resonance frequencies, in virtue of the highest ϵ_r and an L_k value around 26 $pH/\square$. Oscillations occur roughly between 0.8 and 1.1 GHz, with an average separation between adjacent peaks of 20 MHz. Sapphire and diamond show similar resonance frequencies, despite the significant difference in the ϵ_r values, which is compensated by the much higher value of kinetic inductance of the thin film on diamond (22.7 $pH/\square$ vs 7.3 $pH/\square$ for sapphire). The frequency values are in any case higher than what was calculated for silicon, with sapphire showing values comprised between 1.9 and 1.4 GHz, while diamond is slightly lower at 1.8 to 1.3 GHz. For the latter two transparent substrates, the average separation between two adjacent peaks is around 33.3 MHz. Figures 3.15 and 3.16 report the results of simulations of the 30 and 5 nm thick films on sapphire substrates, in which case the effect of the thin film thickness on the superconducting characteristics is immediately apparent. The 30 nm thick film presented the lowest value of kinetic inductance of all the samples at 3 $pH/\square$. Such a detector would have higher dynamic range, compared to the previous ones, but lower responsivity. The 5 nm films show a calculated value of L_k at 30 $pH/\square$, resulting in resonance frequencies comparable with those found for Silicon. The simulations described so far allowed to obtain a consistent set of frequencies across all substrates, allowing to select combinations

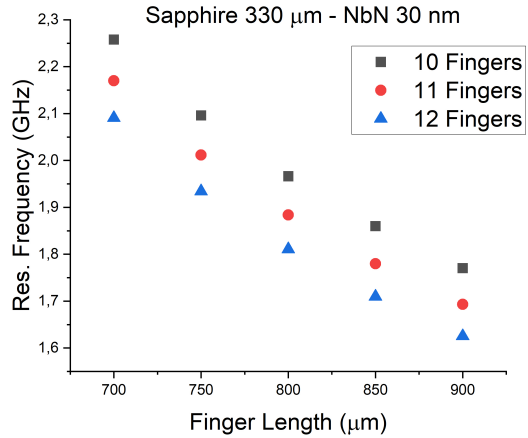

Figure 3.15: Single pixels resonance frequencies, as simulated with Sonnet Software - sapphire substrate, 30 nm NbN layer.

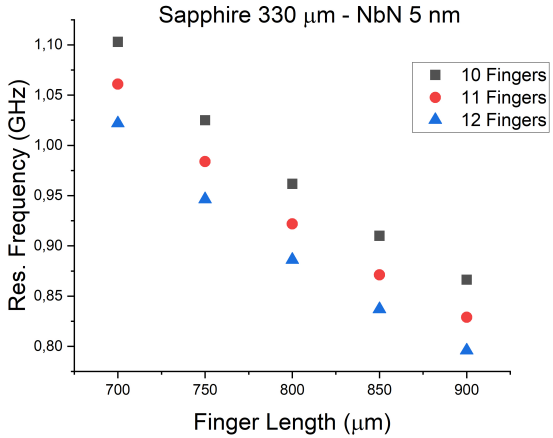

Figure 3.16: Single pixels resonance frequencies, as simulated with Sonnet Software - sapphire substrate, 5 nm NbN layer.

of well separated resonators to compose our detectors and avoid the overlap of adjacent resonances (see table 3.3).

Table 3.3: Summary of the different prototypes/pixels combinations considered for further investigation as obtained from the simulations described above. In the pixels columns, the first number indicates the length of the interdigital capacitor fingers in microns while the second one their amount.

Prot. conf.	Pixel 1	Pixel 2	Pixel 3	Pixel 4
Si330 Proto1	700-10	750-11	800-12	900-12
Si330 Proto2	700-10	850-10	900-11	900-12
Si330 Proto3	750-10	800-11	800-12	900-12
Sa330 Proto1	700-10	750-11	850-11	850-12
Sa330 Proto2	700-11	800-10	800-12	900-11
Sa330 Proto3	700-12	750-12	850-11	900-12
Di700 Proto1	700-10	750-11	850-11	850-12
Di700 Proto2	700-11	800-10	800-12	900-11
Di700 Proto3	700-12	750-12	850-11	900-12

3.3.3 Resonance current analysis

The Sonnet software suite doesn't simulate any kind of optical load on the detector, since it takes into consideration only the frequency response of the resonators excited by a comb of frequencies sent into the transmission line. Nevertheless, some considerations about detector-radiation interactions can be made by looking at the current density flowing inside the pixels when they get excited. As can be seen from fig. 3.17 the value of j is constant on the whole inductive area. When a resonator displays a uniform current distribution, the shift in resonant frequency due to a Cooper pair breaking will be the same independently from

the point on the surface where the event took place. This is different from what happens with distributed resonators like, for example, the quarter-wave resonator, historically the most investigated resonator configuration for this kind of applications before the advent of LEKIDs. With these premises, it is not necessary to direct photons toward a particular zone of the detector to maximize responsivity, but they can be let naturally fall on it [114]. There's no need, therefore, to design antenna structures, since the detector works analogously to a common CCD sensor. The lack of current in the capacitor, on the other hand, means that this portion of the detector is not expected to give a significant contribution to the signal, with previous works [115] showing the cross-polarization signal absorbed by the capacitor to be less than 10%, lowering the risk of cross polarization detection. We also expect the cross detection contribution of the short segments of the inductive part to be negligible, given the 25:1 ratio in length between them and the long sides of the meandering line.

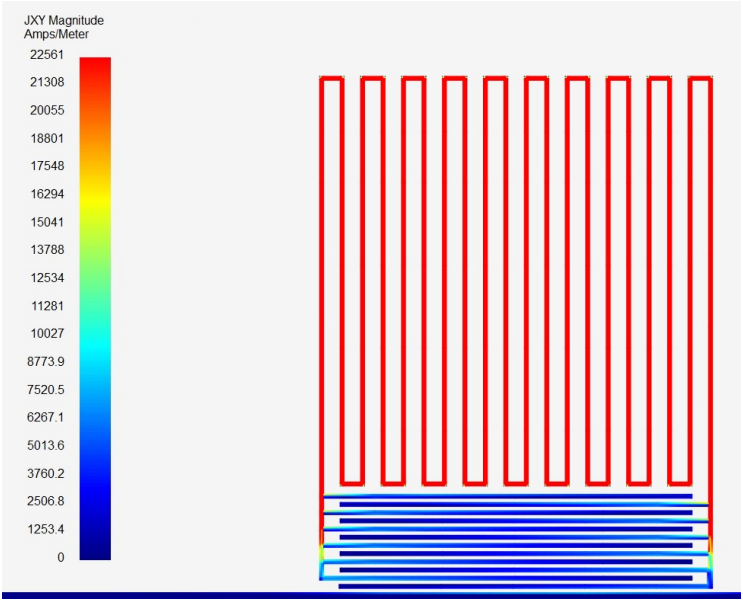

Figure 3.17: Sonnet simulation of the current density flowing inside one of the pixels at the resonance.

3.3.4 Cross-talk

The read-out principle of KIDs allows for a very large number of pixels to be excited and read with a single (or a very small number of) transmission line. While this is a big advantage during both the design and manufacturing phases, it also demands particular attention to avoid pixel cross talk. This effect acts on the resonances by introducing parasitic coupling between pixels that modify the shape, number and position of the resonances. A typical sign of cross-talk is given by the presence of additional resonance peaks in the signal waveform [71, 116, 117], as can be seen in the example shown in Figure 3.18. The bigger the separation between the double resonance peaks, the stronger the effect. To study the occurrence of this phenomenon, identical-pixels systems were simulated: in the absence of cross talk, the simulation would deliver a single resonance peak. The calculations were performed at different inter-pixels distances (10-100 μm in 10 μm steps), and with different shielding configurations: bare, open-box and box. In the latter two, a 10 μm wide NbN strip surrounds either three or four sides of a single resonating unit, as shown in fig. 3.19. In

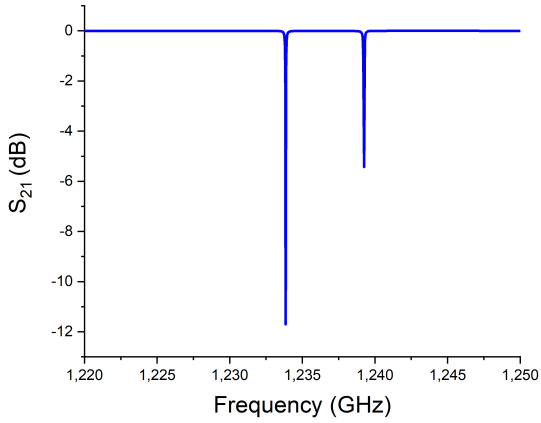

Figure 3.18: Example of cross-talk resonances.

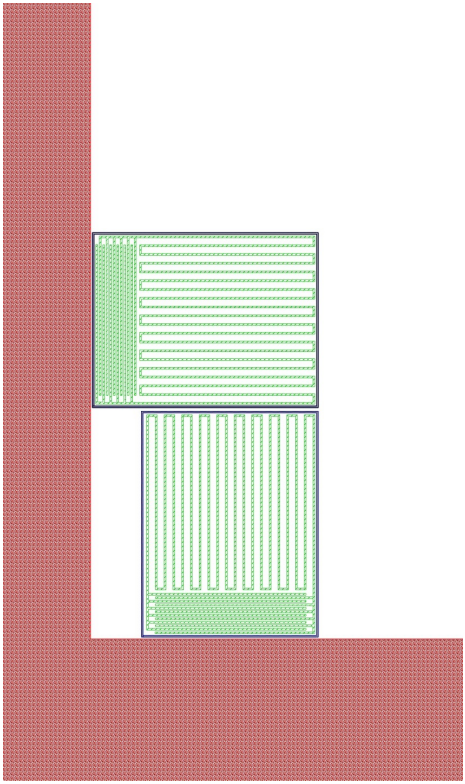

Figure 3.19: Example of Sonnet 2D model of a two pixel boxed system for the study of cross-talk. In red, the transmission line, in blue the shielding, and in green the resonators

the case of the open-box configuration, the open boundary is on the capacitor side, directly facing the microstrip. This was done to investigate the possibility of implementing shielding while keeping a good coupling between pixels and transmission lines. The simulated systems are all based on the 12 fingers, 900 μm long pixel. The results of the simulations can be seen in the figures 3.20, 3.21, 3.22. The performances of the substrates are consistent and it is immediately apparent that the shielding actually increases the effect of cross-talk on the pixels, with the resonances further separated in the presence of the additional structures. The results are in direct contrast with what can be found in literature [24, 71, 117],

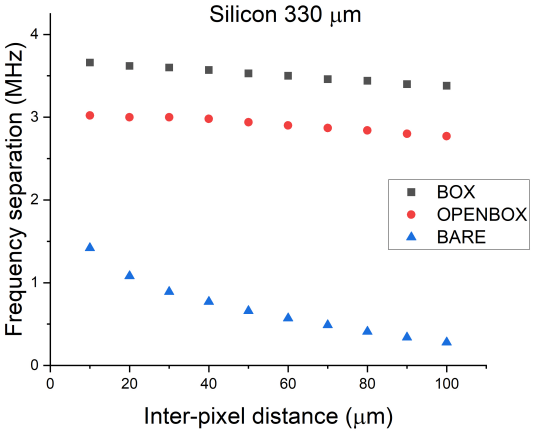

Figure 3.20: Peaks frequency difference as a function of pixel distance from each other - Silicon substrate 330 μm thick.

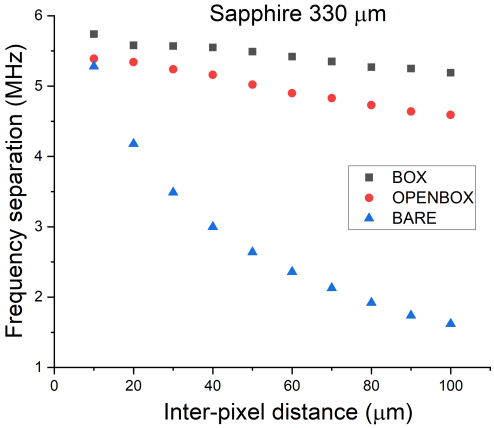

Figure 3.21: Peaks frequency difference as a function of pixel distance from each other - Sapphire substrate 330 μm thick.

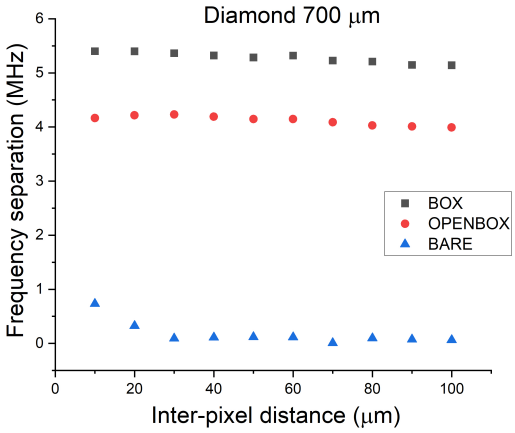

Figure 3.22: Peaks frequency difference as a function of pixel distance from each other - Diamond substrate 700 μm thick.

where such structures are successfully used to limit this effect. This difference can be attributed to the geometrical configuration of the LEKIDs polarimetric arrays: in the iteration of this technology discussed in this work, the pixels are tilted by 90 degs with respect to each other. Since the capacitors are far away from each other and facing different directions, the cross coupling interests mainly the inductive portion of the resonators. The long, uninterrupted, side of the pixel inductor couples with the much shorter segments at the bottom side of its neighbors, whereas in the previous works the pixels where placed side by side in a parallel configuration. Adding the shielding results in long continuous structures facing each other, improving the coupling and inducing stronger currents in the boxes. The shieldings extend in both the box and open box configuration to cover the long side of the inductor, and effectively act as coupling boosters. Increasing the pixel separation, on the other hand, helps with mitigating the effect, especially in the case of sapphire and silicon, where a higher optical density dampens the penetration of electrical fields into the substrate material but doesn't completely solve the problem.

3.3.5 Coupling factor

In the fourth batch of simulations, the coupling between the KIDs and the feedline was investigated. Results for Q_C are reported in the figures 3.23, 3.24 and 3.25. The coupling is mainly inductive through a mutual inductance M between feedline and the meandering part of the resonator. The energy exchange between the resonator and the feedline depends on the magnetic field flux from the microstrip threading the loops formed by the meandering section of the resonators [114]. As mentioned in section 2.3, a good balance between depth and width of the dips is desirable, since saturation of the detector and the overlap between adjacent resonances curves are both to be avoided. The devices are also foreseen to operate with a high probing power and with a low number of pixels per detectors, hence a strong coupling is preferable. A high κ (Eq. 2.81) corresponds to a low resonator quality factor, allowing the energy deposited in the detector to be extracted out of it quickly. Single pixels systems with and without the shielding structures, in a range of feedline - pixel distances from 10 to 100 μm, in 10 μm steps were simulated. The quality factors values were calculated through equations 2.77 and

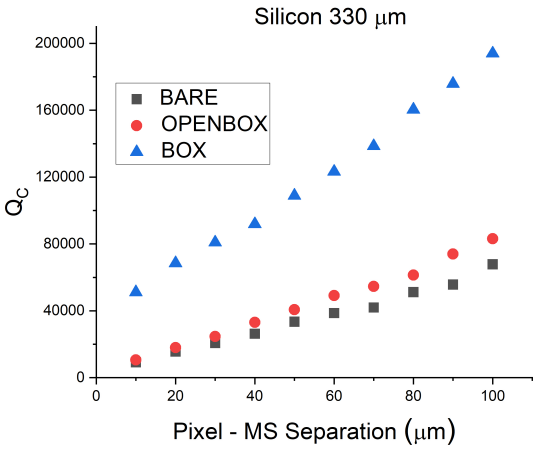

Figure 3.23: Coupling quality factor as a function of the distance between resonator and microstrip - silicon substrate 330 μm thick.

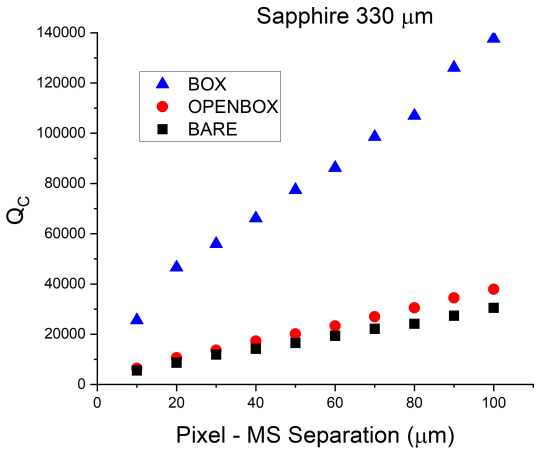

Figure 3.24: Coupling quality factor as a function of the distance between resonator and microstrip - sapphire substrate 330 μm thick.

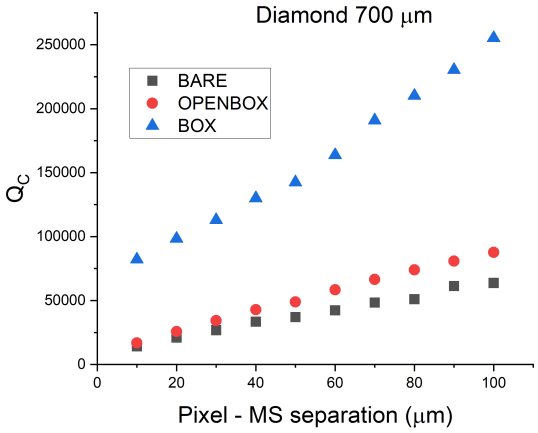

Figure 3.25: Coupling quality factor as a function of the distance between resonator and microstrip - diamond substrate 700 μm thick.

2.83, with the -3dB method [114] used to estimate the loaded fractional bandwidth $\Delta\nu_L$. The internal factors Q_0 of the detectors, originally in the $10^5 - 10^6$ range, are expected to drop to around $10^3 - 10^4$ once illuminated [118]. The detector response is maximized for $Q_L = Q_C$ [119] and it is therefore important to design the structures of the resonators so that the coupling and loaded Q lie within similar value ranges. As can be seen from the figures 3.23, 3.24 and 3.25, the box configuration limits the coupling even for very short separation distances, pushing the values of Q_C outside the desired range of around 10^4. The numbers for Q_L closely mimic those of Q_C, as can be seen from the plots in figures 3.26, 3.27 and 3.28. The condition for the maximization of the responsivity of the detector is therefore satisfied. The open-box design has a limited effect on the coupling as expected, with Q_C values lying in the same range as the bare model ones. The simulations point to the fact that even with open-box and bare configurations, placing pixels at more than 50-60 μm distance should be avoided to limit both the Q values and the detector footprint. Being able to pack the resonators closely together makes beam alignment over the detector easier and more resilient to successive misalignments.

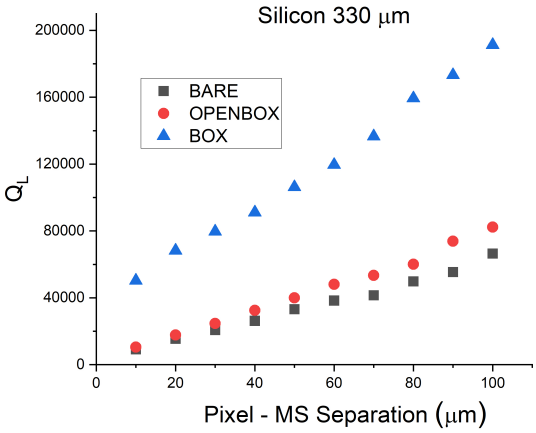

Figure 3.26: Loaded quality factor as a function of the distance between resonator and microstrip - silicon substrate 330 μm thick.

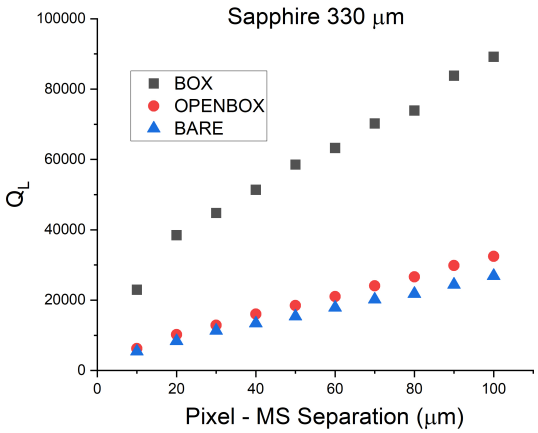

Figure 3.27: Loaded quality factor as a function of the distance between resonator and microstrip - sapphire substrate 330 μm thick.

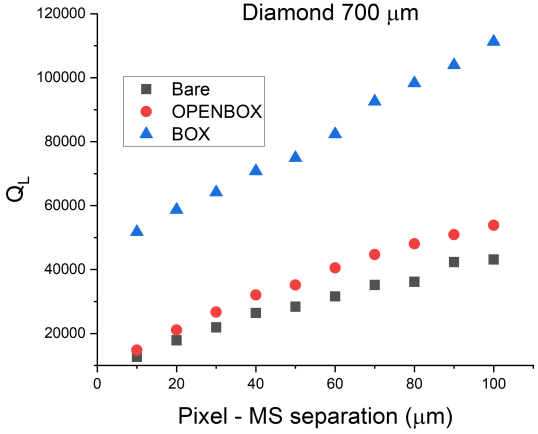

Figure 3.28: Loaded quality factor as a function of the distance between resonator and microstrip - diamond substrate 700 μm thick.

3.3.6 Prototype simulations

The last batch of simulations was dedicated to the study of complete detectors. The input for the Sonnet Suite were the pixels combinations reported in table 3.3. In this section the simulations relative to only one combination per substrate and film thickness are shown. The complete set of simulations can be found in the appendix A. Simulations for the 15nm thick NbN films over silicon, sapphire and diamond substrates are shown in figures 3.29, 3.30 and 3.31 respectively. Figures 3.32 and 3.33 show the simulations for the 5 and 30 nm thin films over sapphire. The absence of multiple resonance peaks denotes a general lack of cross-talk. The separation in frequencies between the KIDs composing the prototypes is sufficiently wide to avoid this effect. Therefore, additional shielding structures are deemed not necessary, simplifying the design and production phases and ensuring a strong coupling. The pixel-to-pixel and pixel-to-feedline distance was chosen to be 10 μm, taking into account the considerations exposed in section 3.3.5.

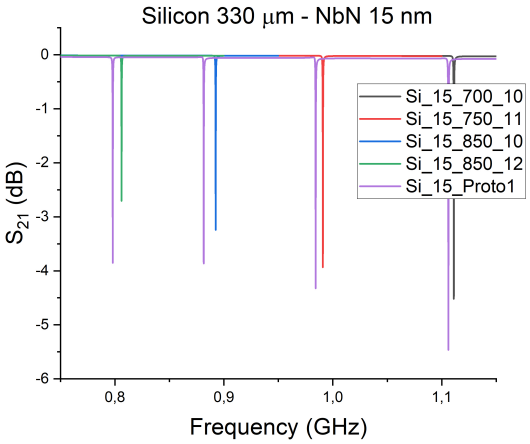

Figure 3.29: Sonnet simulation of the Proto1 configuration on 330 μm thick silicon substrate (15 nm NbN), showing the resonances of the single pixels composing the complete detector.

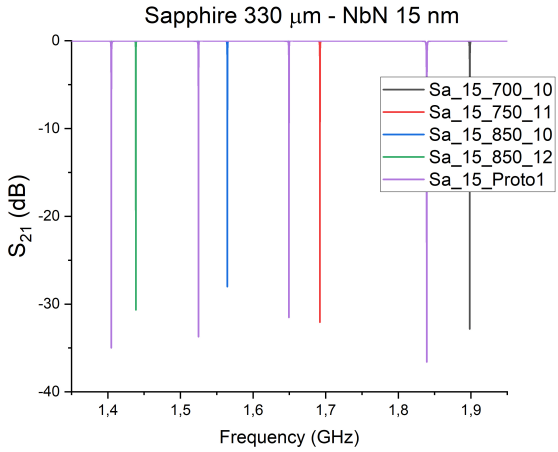

Figure 3.30: Sonnet simulation of the Proto1 configuration on 330 μm thick sapphire substrate (15 nm NbN), showing the resonances of the single pixels composing the complete detector.

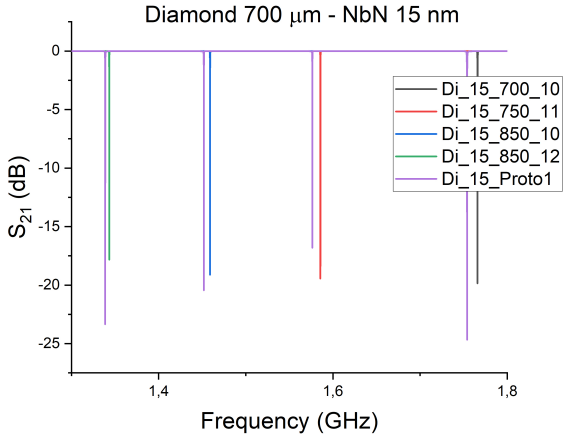

Figure 3.31: Sonnet simulation of the Proto1 configuration on 700 μm thick diamond substrate (15 nm NbN), showing the resonances of the single pixels composing the complete detector.

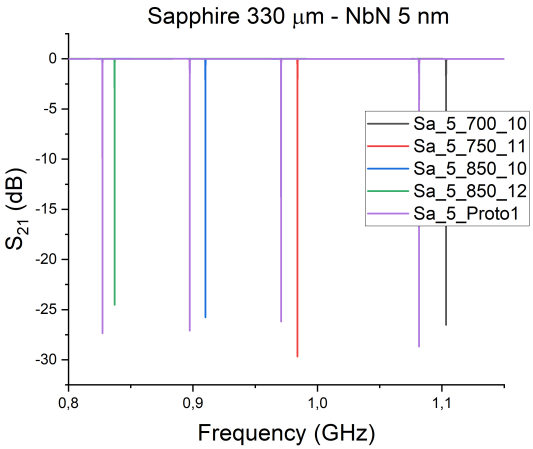

Figure 3.32: Sonnet simulation of the Proto1 configuration on 330 μm thick sapphire substrate (5 nm NbN), showing the resonances of the single pixels composing the complete detector.

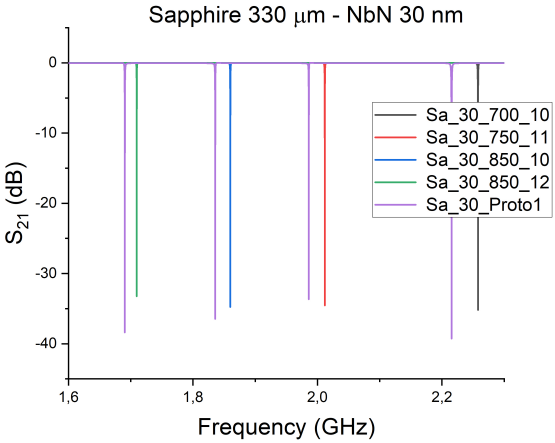

Figure 3.33: Sonnet simulation of the Proto1 configuration on 330 μm thick sapphire substrate (30 nm NbN), showing the resonances of the single pixels composing the complete detector.

It can also be noticed how there is a general shift of the four resonances of the detector lower values when compared to results by simulating the single resonators. This effect can be explained by taking into consideration the modified geometry of the feedline and the capacitive effects deriving from it. In light of the results presented so far, all the prototypes described above and shown in the appendix were manufactured, in an effort to validate the simulations and to measure a wide range of different combinations of substrates, geometries and configurations and to optimize the obtained devices for the application at hand.

4 Sample Preparation

The performance of a KID depends not only on its geometrical characteristics, but also on the properties of the deposited superconductor. The kinetic inductance depends on the film volume, with smaller volumes leading to larger values of L_K, but also to increased surface losses. While a larger kinetic inductance increases the responsivity of the detector, at the same time the losses lower the resonators internal quality factors and reduce the sensitivity. The quality and uniformity of the deposited film has also a big impact on its superconducting characteristics, with highly disordered films showing lower critical temperatures and wide, often multi-step transitions. Additionally, the film should be thinner than the London penetration depth for a given superconductor (100-200 nm for NbN [94][95]) and narrower than the Pearl length Λ [23][97], the effective magnetic field penetration depth defined as

$$\Lambda = \frac{2\lambda^2}{d}, \tag{4.1}$$

where $d \ll \lambda$ is the film thickness. With these conditions satisfied, the current density across the superconductor is homogeneous, resulting in detectors with uniform sensitivity across their surface. It is therefore mandatory to operate with a very well controlled and repeatable deposition process. All the thin films presented in this work have been deposited via DC reactive magnetron sputtering, patterned with UV-photolithography and finally etched with Reactive Ion Etching (RIE). In this chapter all three processes will be described and the adopted parameters given.

4.1 DC reactive magnetron sputtering

DC magnetron sputtering is a very well established physical vapor deposition technique for high quality superconducting film. The main actors involved in the process are electrons, positively charged "working gas" ions and the target atoms. Electrons are generated at the cathode (the magnetron itself) normally through a thermal process and accelerated by the DC bias in the order of kilovolts. They subsequently impact working gas atoms, ionizing them (fig. 4.1). Typical working atmospheres for this techniques are composed by noble gases like argon. The plasma so formed is accelerated by the DC static electrical field toward the target where the highly energetic gas atoms knock target material atoms away, which deposit on the substrate as thin film. In case of superconducting nitrides as is the case with NbN, the necessary nitrogen is added to the working atmosphere, and reacts with the surface of the target to form the desired compound. At that point, the sputtered molecules are free to fall onto the substrate. Given that the whole process is performed at very low pressures (usually, $10^{-3} - 10^{-2}$ mbar), the electron mean free path can be larger than the distance between target and the substrate. Under these conditions, the electron-working gas scattering cross

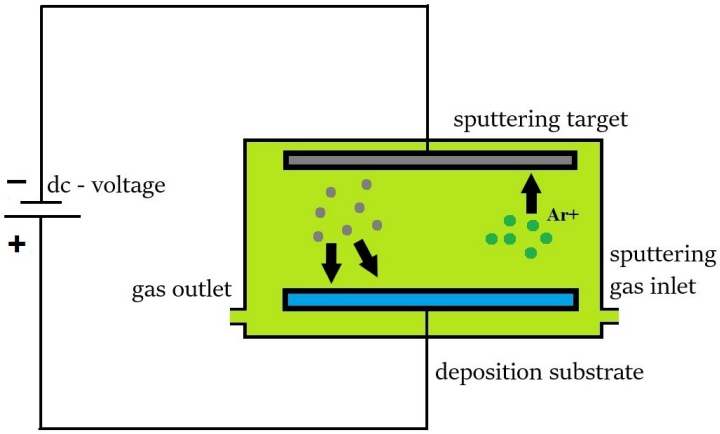

Figure 4.1: Schematic representation of DC magnetron sputtering process.

section is very small and would result in non-sufficient interaction between the two species. Therefore a magnetic field, perpendicular to the static DC potential, is introduced. Such magnetic field causes the electrons to undergo spiraling orbits, increasing the probability of interaction with the working gas and improving the sputtering speed. Increasing the intensity of the magnetic field leads to tighter electron gyration radii and has also an influence on the ionization volume. The substrate is often placed on a heater that can reach several hundreds of degrees. This is helpful to reduce the crystalline structural defects in the deposited films, improving the uniformity and the adhesion of material onto the substrate.

4.1.1 Deposition procedure

Different temperatures were chosen for the silicon, sapphire and diamond substrates, given their different properties. Sapphire substrates were heated at the highest temperature, 850°C, with silicon following at 800°C and diamond, at 750°C. Whereas the processes on silicon and sapphire are well established and repeatable, the same can't be said for the deposition on diamond, given the lack of literature on superconducting films deposited on this material. On the other hand, graphitization of diamond has been observed in vacuum environments at temperatures as low as 900°C [120], with some reporting the occurrence of this effect at an even lower temperature of around 600°C for non-inert environments [121]. This process is often preceded by thermal decomposition of various chemical groups (mainly oxygen) that can be trapped on the substrate surface [122]. Since we had at our disposal only one 10x10 mm^2 diamond substrate, equivalent to three detectors plus a test strip for the thin film characterization measurements, the deposition temperature was lowered out of caution to avoid the aforementioned phenomena. For all the deposition processes, a 40 minutes long warm up to the desired temperature at a starting total pressure around $1.8 \cdot 10^{-7}$ mbar was performed, followed by a target cleaning phase in a pure Ar atmosphere at a pressure of $1.8 \cdot 10^{-3}$ mbar. The magnetron voltage and current were set to 300 V and 100 mA, respectively. At this point the nitrogen was let into the deposition chamber, increasing the total pressure to $2.16 \cdot 10^{-3}$ mbar. The whole system was given enough time in between the various phases to stabilize under the thermal and

barometric point of view. With these parameters, a deposition rate of 0.065 nm/s was estimated.

4.2 Photolithography and reactive ion etching

Photolithography is the process used to pattern structures on a thin film deposited onto a substrate by using light to impress the geometry of the required circuit on it. There are several substances (so-called photo-resist) that, following the absorption of light, are induced into undergoing chemical reactions and molecular modification. The end result can be either the destruction of chemical bonds and the creation of new, smaller molecules or the other way around. The first case correspond to positive resist lithography, while the second is called negative. Once the photo-resist has been impressed with an image of the patterned structures (or its negative, depending on the type of resist), it is developed with the use of a liquid chemical solution, that reacts with the short, less stable molecules, eliminating them from the surface of the sample. The light source used to expose the resist is generally a collimated UV beam coming from a lamp coupled to a photomask containing the geometry to be impressed (fig. 4.2). In case of positive photolithography, the photomask contains the exact image of what is going to be the end product, so that the underlying resist layer is impressed only in the zones that will need to be removed afterward. The use of short wavelength light is necessary to stimulate the chemical reaction and has the added advantage of lowering the diffraction limit of the system, improving resolution. This technique is capable of resolutions in the order of 0.5 μm and is therefore perfectly suited for applications that require structures with dimensions in the order of tens of micrometers, like is the case for the polarimetric KIDs. In Fig. 4.3 a magnified portion of the mask is shown. Since the substrates at disposal for this work all consisted in 10x10 mm^2 wafers, the available space on the mask was split accordingly. Each subdivision contains the three prototypes and a test strip that was used for the thin film characterization measurements (see section 5.1). The test strips are 2.5 mm long and 20 μm wide, with 1 mm square contact pads.
There are several methods employed to remove the material of a film using the

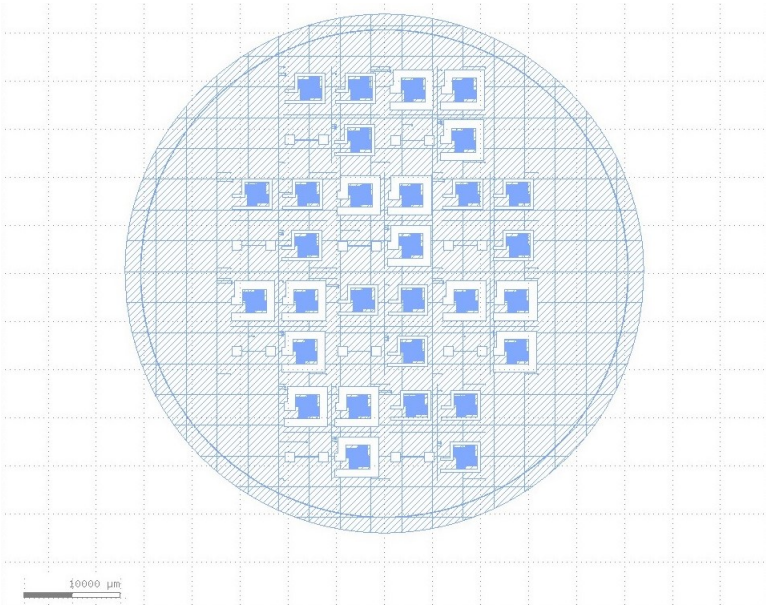

Figure 4.2: Design of the two inches-diameter photomask used for the production of the prototypes on sapphire (thin transmission line) and diamond (thick transmission line).

patterned resist as a mask. For the production of all the prototypes Reactive Ion Etching (RIE) was employed. It consists in a plasma assisted dry-etching technique that allows the removal of material without the use of chemical solutions ("wet" etching), which leaves residuals on the surface of the sample, and water, which can degrade the quality of the superconducting thin film. In such technique, the sample is placed inside a vacuum chamber equipped with a controllable gas inlet valve and a high power RF-emitter. The starting base pressure is around 10^{-6} mbar and, as the name suggests, a gas containing a reactive element (fluorine for Nb based thin films) is let in. The RF power ionizes the gas molecules, creating an extremely reactive plasma of F radicals that end up interacting with the metallization left exposed after the development phase. The volatile metal-fluorine compounds are then pumped away from the chamber. The gas used in the process was SF_6 with a flow of 30 sccm together with 6 sccm of pure oxygen added to increase the anisotropy of the process, for a total operating pressure of

roughly 0.35 mbar. The chamber was preconditioned for a few minutes before the actual etching process, using the same parameters.

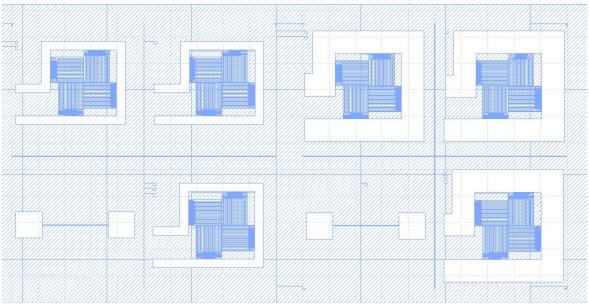

Figure 4.3: Zoomed-in section of the photomask used in the lithography of sapphire (left) and diamond (right) prototypes. Each wafer subdivision is 10x10 mm and encases the three prototypes and an additional test strip used for the thin film characterization measurements

5 Results and Discussion

In the following sections, the results of the tests performed on the deposited thin films and the prototype KIDs are presented and discussed. The experimental activity consisted in three different kinds of measurement, with the purpose of characterizing multiple aspects of the manufactured samples. The first step involved the measurement of resistance-temperature (R/T) and current-voltage (I/V) characteristics of the thin films. The recorded curves allow to evaluate the quality of the deposited superconductors and to extrapolate considerations about the performances of the detectors in the successive measurements. Additionally, the values of kinetic inductance extracted from the R/T curves were used as cross reference and refinement tool for the simulations shown in chapter 3. The second step of the experimental activity consisted in measuring the response of the resonators to a comb of frequencies injected in and extracted from the microstrip transmission line by a Vector Network Analyzer (VNA). The resonance curves were compared with those that were simulated and provided a methodology to estimate, among others, the effective loss tangent of the substrates that were employed [123]. The last round of measurements consisted in the optical response of the detectors to THz radiation. With these last tests it was possible to estimate the detector responsivity, noise level, response time and cross polarization rejection capabilities.

5.1 Superconducting thin film characterization

5.1.1 Equipment and procedure

The R/T and I/V profiles were recorded with a LabView-based automated control system, connected to a Keithley Nanovoltmeter Model 2182A, a Keithley 6220 Low Noise Precision DC Current Source and a LakeShore PID 335 Cryogenic Temperature Controller. The samples were bonded with 25 μm thick aluminum wires to a chip carrier (Fig. 5.1). Once bonded, the chip carrier is inserted in a multi channel socket (Fig. 5.2b) at the end of a dipstick connected to the acquisition system (Fig. 5.2a). The top of the dipstick is equipped with a filter box to block all the external signals that the dipstick connection cable, acting as an antenna, could

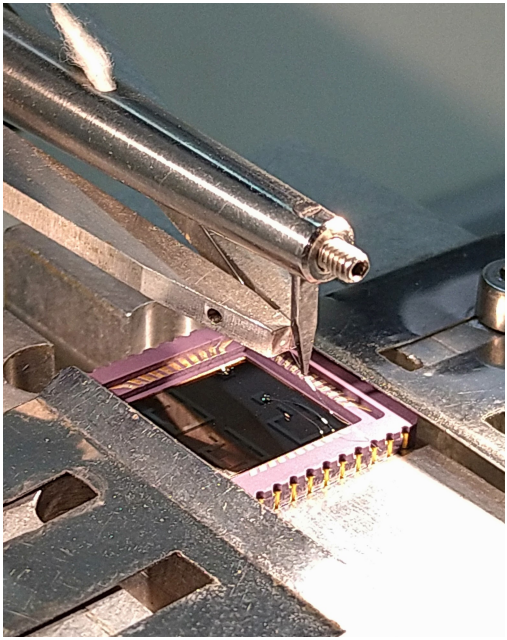

Figure 5.1: One of the samples test strip being bonded to the chip carrier. The bonding wires are 25 μm thick and made of aluminum. The chip was uncut, and the three detector prototypes are also visible.

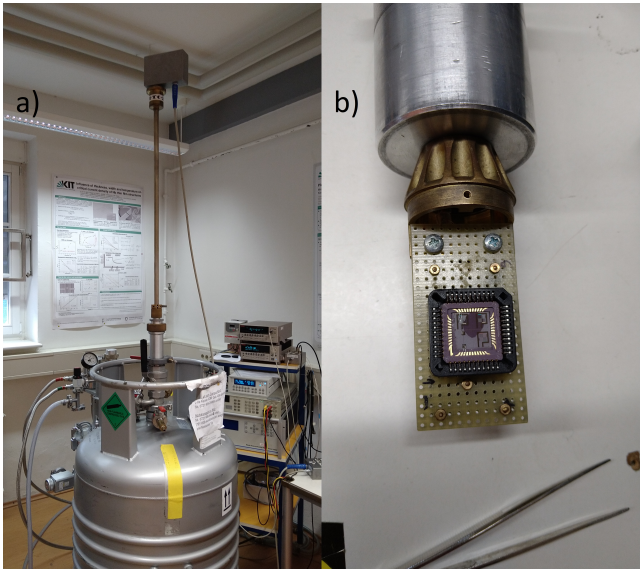

Figure 5.2: a) Thin film characterization dipstick ready to be inserted into the LHe dewar for measurements. In the background the temperature controller, the current source and nanovoltmeter can be seen. b) One of the sapphire samples already bonded to the chip carrier, mounted on the dipstick socket. During the bonding procedure, a small quantity of vacuum grease (visible as a darker area) was used as sticking agent between the carrier surface and the bottom of the substrate to increase adhesion and improve stability during the bonding process.

pick up. The R/T measurement is performed by manually inserting the dipstick deeper and deeper in the dewar, until a temperature of 4.2 K is reached. Particular attention was given to insert the dipstick not too fast, to avoid sudden evaporation of the liquid helium and also obtain good number of temperature points recorded. The adopted speed of insertion figure of merit is around 0.2 K/s of temperature drop. Once the 4.2 K point is reached, the system can be switched to I/V mode and the critical current can be measured. The estimate of the Residual Resistance Ratio (RRR) was performed taking onto consideration values of R at 300 K and at 20 K, while the width of the superconducting transition ΔT_C and the value of T_C were estimated between 10 and 90 $\%$ of R(300K).

5.1.2 Measurements

Figure 5.3 shows the R/T curves of the two silicon wafers employed for the first depositions of NbN. These samples are all equipped with a backshort, as described in section 3.2.1, in the form of a 400 nm thick NbN layer on the backside. This additional deposition procedure was performed at room temperature to avoid damages and degradation of the already patterned thin film on the top. As it can be seen, the two curves overlap almost perfectly, indicating a good repeatability of the deposition process. A critical temperature around 11 K and a transition width ΔT_C of roughly 0.5 K were measured. The values are in line with what can be found in literature for DC sputtered films of the same thickness [116]. Critical current densities of 3.25 and $3.31 \cdot 10^6$ A/cm^2 were measured at 4.2 K. The values of the RRR were determined to be 0.88 and they indicate a disordered and granular film, with a semiconductor-like behavior above the transition. The non optimal quality of these thin films can be explained as due to a mismatch in the lattice constants of the two materials. As a matter of fact, silicon has a diamond FCC lattice structure, with a constant equal to 5.431 Å [124], while NbN

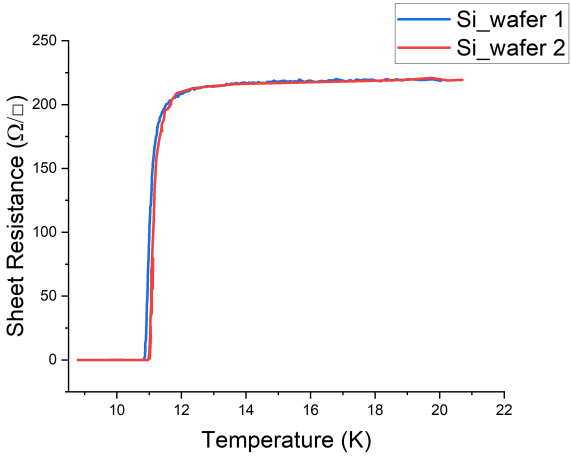

Figure 5.3: R/T curves for the 15nm NbN thick films deposited on silicon wafers at 800°C.

has a rock-salt (halite) cubic structure and a smaller unit cell at 4.446 Å [72]. This difference induces mechanical stresses in the thin film, worsening its uniformity and leading to lower critical temperatures and wider transitions. Sapphire has a rhombohedral trigonal structure and, with a lattice parameter a equal to 4.785 Å [125], represents a much better match for the NbN unit cell, leading to improved superconducting transition characteristics. This can be observed in figure 5.4, that shows the R/T curves for the 5, 15 and 30 nm thick films deposited onto a sapphire substrate at 850°C. The recorded values of the critical temperatures are 12.5, 13.5 and 13.9 K, with transition widths in the order of 0.27 K, 0.18 K and 0.09 K for the 5, 15 and 30 nm films, respectively. The critical temperature is lower for thinner films, because of the proximity effect [126, 127]. This phenomenon consists in the mutual influence between two different materials and it is particularly strong in the case of a superconductor deposited over a normal metal. It occurs at the interface between the two materials, where gradients of the electrons and Cooper pairs induce diffusion: of the former in the superconductor, and of the latter in the normal metal. In our case, the process is intrinsic in nature and occurs between the superconducting core of the film and its outer, non superconducting layers (Fig.

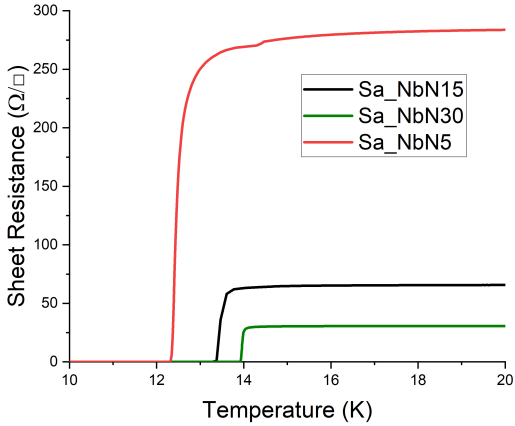

Figure 5.4: R/T curves for the thin films with thicknesses of 5, 15 and 30 nm deposited on sapphire substrates at 850°C.

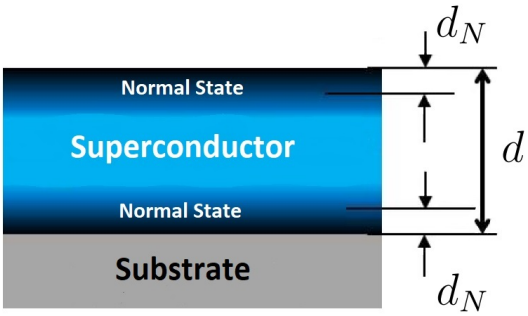

Figure 5.5: Schematic representation of intrinsic proximity effect in a superconductor. d represent the thin film total thickness, while d_N indicates the thickness of the outer layers, where superconductivity is suppressed as a consequence of lower film quality.

5.5). These layers revert to normal state as a consequence of degraded film quality mainly caused by the lattice mismatch with the substrate and oxidization of the surface exposed to air. The end result is a decrease of the average superconducting strength and a delay of the onset of the transition to lower temperatures. This effect is proportionally stronger for smaller volume films. Additionally, the thinnest film shows a two step transition at around 14.3 K, sign of a highly disordered film. The values of critical current density are $2.28 \cdot 10^6$ and $9.3 \cdot 10^6$ A/cm^2 for the 5 and 15 nm thick films, respectively. It was not possible to measure the critical current density of the 30 nm thick sample, since it was above the maximum current value of the available source. The computed RRR values are consistent with the critical temperature measurements, with the 5 nm film showing a sub-unit residual ratio equal to 0.96. The two other film thicknesses show a metallic behavior with RRR values equal to 1.07 and 1.09 for 15 and 30 nm thick films, respectively. Figure 5.6 shows the R/T curves recorded for the sapphire samples that have been endowed with a backshort. The deposition of the NbN layer on these samples resulted in slightly thinner films, 25.5 and 13.3 nm, respectively. This is due to the fact that the process was carried out just after maintenance of the deposition chamber and the subsequent reconditioning, which led to lower deposition rates with the parameters previously employed. Additionally, deposition conditions

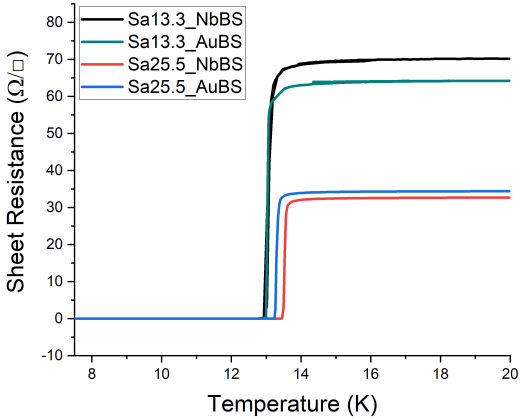

Figure 5.6: R/T curves for the thin films with thicknesses of 13.3 and 25.5 nm deposited on sapphire substrates at 850°C. The substrates underwent an additional room temperature deposition process on their backside for the creation of a backshort. The backshort materials were pure niobium and gold.

for thin films (under 30 nm) differ substantially from those for thick (> 100 nm) ones, the re-optimization of which would have required several weeks. This fact led to the choice of alternative backshort materials for which these conditions were readily available. We therefore decided to employ gold and pure niobium (max $T_C \approx 9.2$ K [128]) backshorts. A large room-temperature conductivity ground-plane also helps to limit the losses at the higher operating frequencies that characterize the sapphire samples. The sputtering of the backshorts was performed in different deposition chambers than the one used for the NbN. These chambers lacked a heater for the substrate, but the deposition would have been in any case performed at ambient temperature, given the arguments about film quality degradation expressed for the silicon samples. Taking into consideration the smaller thickness of these films, the performances of these samples are in line with the backshort-less samples. T_C is around 13 K for the thinner film with a width of 0.27 K and 0.3 K for Nb and Au backshorts respectively. The thicker films have a slightly higher T_C at 13.3 and 13.5 K for Au and Nb, with

widths of 0.18 K and 0.2 K respectively. The RRR is in all the cases above unity, comprised between 1.08 and 1.12. Critical current densities are also very similar for the thinner films, at 6.65 and $6.78 \cdot 10^6$ A/cm^2 for Au and Nb backshorts, respectively. The critical currents of the thicker films exceeded the capabilities of the employed source, analogously to what happened with the backshort-less samples.

For the diamond substrates the considerations done on lattice compatibility for the silicon samples led to the investigation of an alternative superconductor in addition to NbN that would better match the crystalline structure of diamond. The crystal structure of the carbon allotrope is cubic hexoctahedral with a unit cell that measures 3.567 Å [129] and therefore induces compressive stress in the larger crystal structure of NbN. On the other hand pure Nb, characterized by a body-centered cubic structure, has a lattice constant of 3.3 Å [130], making it a good match for diamond. Fig. 5.7 shows the R/T curves for Nb and NbN films deposited on diamond. The Nb film was sputtered at ambient temperature, while the NbN 15 nm thin film was deposited at 750°C. Pure niobium is a transition metal with good conductive properties ($\rho_{Nb} = 15.2$ $\mu\Omega$·cm at 0°C for bulk

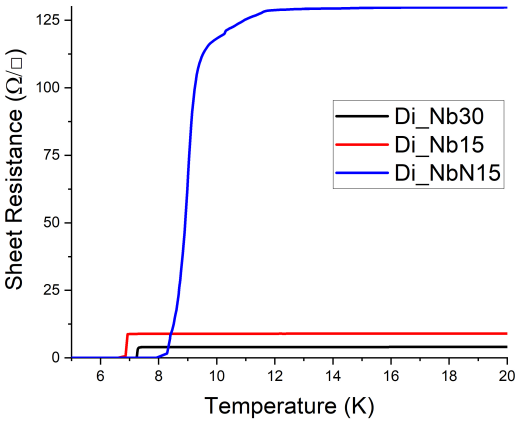

Figure 5.7: R/T curves for the thin films of pure Nb (15 and 30 nm) and of NbN (15 nm).

material) and behaves as such, as can be seen from the R/T curves for 15 and 30 nm thick films. The RRR are 1.79 and 2.04, respectively, while the value for the 15 nm thick NbN film on the same substrate is sub-unitary at 0.91. As previously mentioned, the maximum critical temperature of Nb (9.2 K) is lower than that of NbN (16 K), an aspect reflected in the measured curves that put the transitions at 7.27 K for the 30 nm thick film and at 6.85 K for the 15 nm one. The main factor lowering the film quality is in this case the deposition performed at ambient temperature. The transitions are nevertheless very sharp with widths of 0.08 and 0.1 K, respectively, sign of a good film uniformity. In contrast, the NbN film transits to the superconducting state at 9.05 K, almost 4.5 K less than the 15 nm film on sapphire, with a multi step and very wide ($\Delta T_C = 1.24$ K) transition, all signs of an disordered film. The difference in quality of the NbN film on different substrates is immediate under a simple visual inspection with an optical microscope. The film deposited on diamond captured in Fig. 5.8(a) shows spots and irregularities, while the film on sapphire (Fig. 5.8(b)) shows a much cleaner image. The use of a dielectric buffer layer with intermediate lattice constant (i.e. MgO, halite structure and lattice parameter a = 4.21 Å) could represent a viable solution to relieve stress and obtain a better quality film. The measurements of the critical current density for the NbN film support these considerations, with a value of $5.67 \cdot 10^5$ A/cm^2, more than one order of magnitude lower than measured for

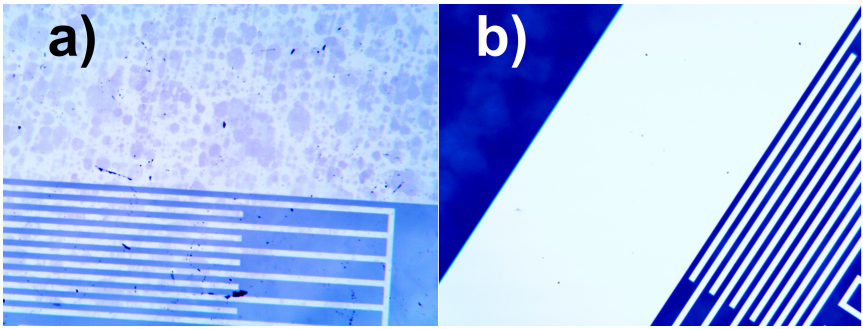

Figure 5.8: Optical microscope image of the 15 nm NbN film on diamond (a) and on sapphire (b). The irregularities of the NbN film deposited over the carbon allotrope are immediately evident.

both silicon and sapphire substrates. Once the critical temperatures of the various films were determined, it was possible to estimate the value of the corresponding kinetic inductance. The expression used for the calculation was taken from the works of Annunziata et al. [89] and Mauskopf et al. [113] and is equal to:

$$L_k = \frac{\hbar R_s}{\pi \Delta}. \tag{5.1}$$

In table 5.1 the values of the various measured and calculated parameters are summarized. The data extracted from the R/T and I/V characterization was then used to refine the simulations of section 3.3, which up to that point were based on values obtained by literature and therefore not always consistent with the deposition procedures and parameters employed in this work.

Table 5.1: Calculated and measured thin film parameters.

Sub-Film.	T_C (K)	ΔT_C (K)	j_C (MA/cm^2)	RRR	Δ	L_k (pH/□)
Si-NbN15-1	11.2	0.5	3.25	0.88	1.71	28.5
Si-NbN15-2	11	0.47	3.21	0.88	1.67	27.4
Sa-NbN15	13.4	0.18	9.3	1.07	2.03	7.28
Sa-NbN30	13.9	0.09	n.a.	1.09	2.11	3.33
Sa-NbN5	12.48	0.27	2.28	0.96	1.89	30.33
SaAu-NbN13.3	13.04	0.3	6.65	1.11	1.98	7.57
SaNb-NbN13.3	13.05	0.27	6.78	1.08	1.98	8.34
SaAu-NbN25.5	13.53	0.18	n.a.	1.12	2.05	3.76
SaNb-NbN25.5	13.295	0.2	n.a.	1.1	2.02	3.96
Di-NbN15	9.05	1.24	0.567	0.91	1.44	22.77
Di-Nb15	6.85	0.1	n.a.	1.79	1.04	3.25
Di-Nb30	7.27	0.08	n.a.	2.04	1.1	1.57

5.2 Resonators high frequency response

The measurements performed to check the presence of the pixels resonances are conceptually similar to what was done for the DC tests, with a dipstick equipped, this time around, with semi-rigid SMA cables and connectors. A custom detector box was machined out of a block of electrolytic copper while the impedance-matched microstrip visible in fig 5.9(a) was realized out of a double-sided PCB through photolithographic techniques. Depending on the presence or not of a backshort on the backside of the sample, either electrically conductive silver-based grease or vacuum grease was employed to improve the adherence of the detector to the ground plane of the detector box and facilitate the bonding process, similarly to what has been done for the chip carriers employed in the R/T measurements. A pair of SMA connectors feed-through soldered to the microstrip and a cover, also made out of copper and with a look-through window, complete the box (Fig.

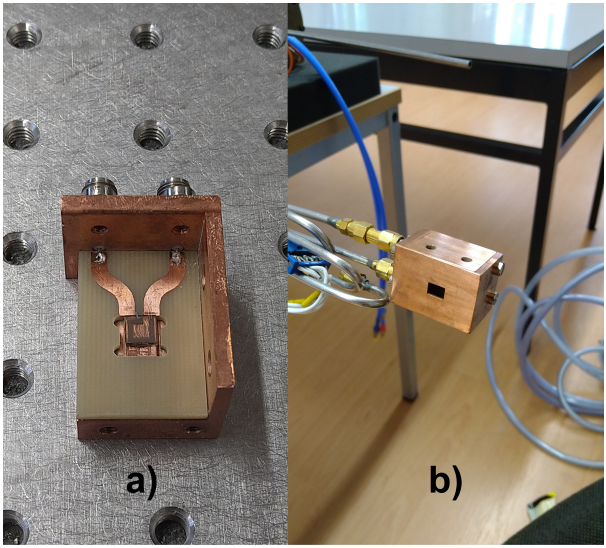

Figure 5.9: a) Detector box with a bonded detector installed (diamond substrate). The SMA connector feed-troughs and the PCB microstrip are also visible. b) the assembled detector box connected to the end of the dipstick.

5.9b). The VNA used to excite the detectors and read the output was set to -20 dB power in all the measurements, in order to avoid potential saturation of the resonators. Additionally, a -20 dB attenuator was attached to port 1 to limit the input noise. The dipstick was, at that point, slowly inserted inside the dewar, letting it regularly thermalize, once again to avoid excessive helium evaporation and pressure buildup. The transition to superconductivity was marked by a jump in the signal baseline from roughly -60dB to roughly -40 dB. At that point the resonances start to appear, shifting toward higher frequencies and growing in depth as the temperature of the sample decreases. Once stable, they were recorded in the VNA internal memory. The IF bandwidth of the analyzer was set to 1 kHz to limit the noise of the acquirement and each wide-band measurement of the whole resonance spectrum was followed by high-resolution single peaks measurements that would later be used to estimate the quality factors relative to the resonators.

5.2.1 Silicon substrate

Figure 5.10 shows the measured and simulated values of the scattering parameter S_{21} for the Prototype1 configuration for the silicon substrates. The first resonance peak is shallower than the corresponding simulated one, an additional indication of a less than optimal film quality and uniformity. Nevertheless, the frequencies simulated taking the calculated L_k values as reference are in accordance with the measurements. The baseline signal shows a ripple-like structure, indicating the presence of stationary waves along the transmission line due to impedance mismatch. As mentioned in section 3.2.2, whereas the detectors were designed around a 250 μm substrate for optimal coupling with incoming radiation, the NbN thin films were deposited on a 330 μm thick substrate. The baseline presents also a monotonically decreasing behavior, explainable with the strong frequency dependence of the input impedance of the mismatched transmission line shown in fig. 3.11. As the frequency of the excitation tone increases, a bigger portion of the signal is reflected at the input location instead of being transmitted to the feedline. In fig. 5.11 the third peak from the left from the very same measurement is shown together with the Lorentzian fit used to extract the values of the quality factors. This peak corresponds to the pixel adopted in the simulations performed

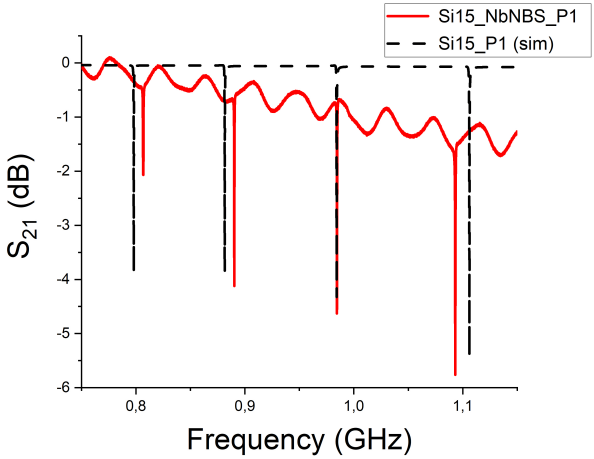

Figure 5.10: Measured (red) and simulated (black dashed) resonances of the Prototype 1 configuration deposited on the 330 μm silicon substrate - 15 nm NbN thick film.

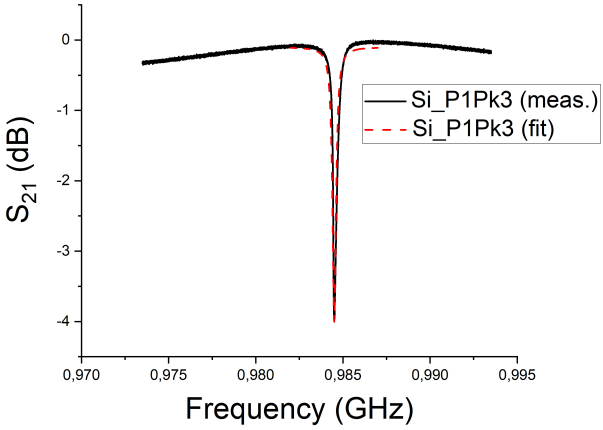

Figure 5.11: Silicon Prototype 1 peak nr. 3 as measured and corresponding Lorentzian fit used to extract the Q values associated with the resonator.

to estimate the quality factors. The slight asymmetry is due to the standing wave regime. The value for Q_C is approximately $1.1 \cdot 10^4$, quite close to the calculated one equal to $9.1 \cdot 10^3$ (Fig. 3.23). This difference in values can be explained by taking into consideration that the simulations for the estimate of the coupling presented in section 3.3.5 involved single pixels systems, in which the resonance characteristics are not influenced by additional capacitive effects induced by the modified feedline geometry of the complete detectors. The general shallowness of the resonances can be explained as due to losses in the substrate and in the resonators, given the non optimal film quality. Additionally, the silver based conductive paste used to have a good thermal and electrical contact between the backshort and the copper ground plate on which the detector rests also influences the outcome of the measurements, as it will be shown in section 5.2.2.1. As a last note, the measurements were performed at relatively high temperature. KIDs are typically operated at $T_C/4$ to reduce the presence of quasi-particles in the superconductor [24]. The higher the temperature, the higher the contribution to the resonator losses given by the superconductor electron population. An improvement of the KID performance can therefore be achieved by moving to a transparent, low losses substrate, with a better mechanical match between the different crystal lattices.

5.2.2 Sapphire substrate

Figures 5.12 and 5.13 confirm the considerations exposed at the end of the previous section by showing much deeper resonance dips. The NbN thin film on sapphire has also a higher transition temperature, hence lowering the quasi-particle population present in the superconductor at the measurement temperature. Both the ripple-like structures and the monotonic decreasing baseline are present, albeit to a smaller extent. The transmission line is better matched to the readout electronics and its impedance shows a weaker dependence on frequency. A value for Q_C of 3730 has been extracted from the measured data, while the simulated one is equal to 5532, a factor of about 1.5 difference. Figure 5.14 presents the measurements performed on the 5 nm thick films sapphire prototypes. The effect of the higher

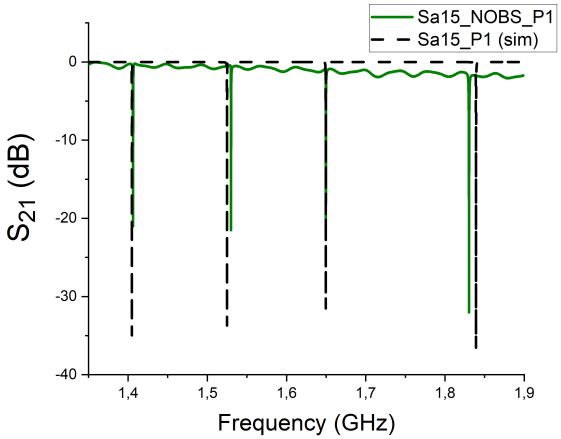

Figure 5.12: Measured (green) and simulated (black dashed) resonances of the Prototype 1 configuration deposited on the 330 μm sapphire substrate - 15 nm NbN thick film.

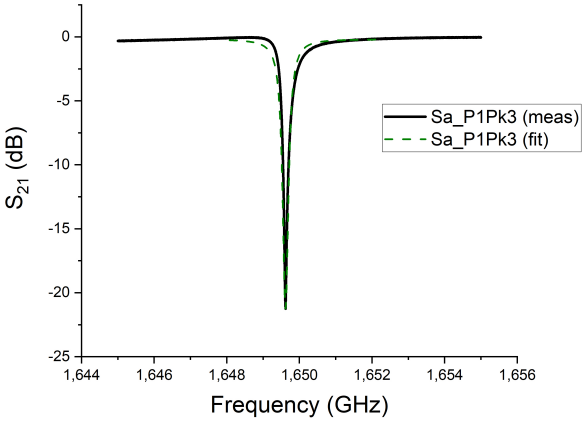

Figure 5.13: Sapphire Prototype 1 Peak nr. 3 as measured and corresponding Lorentzian fit used to extract the Q values associated with the resonator.

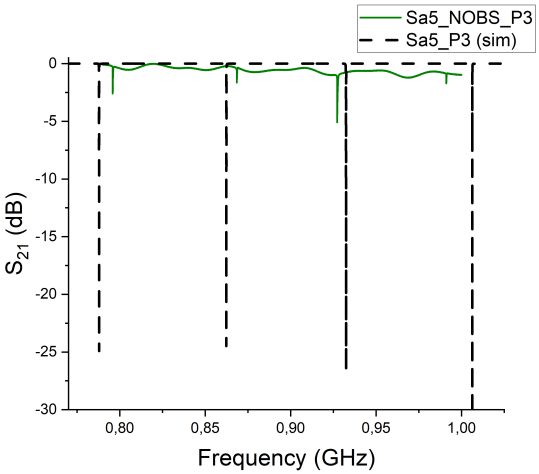

Figure 5.14: Measured (green) and simulated (black dashed) resonances for the Prototype 3 configuration deposited on the 330 μm sapphire substrate - 5 nm NbN thick film.

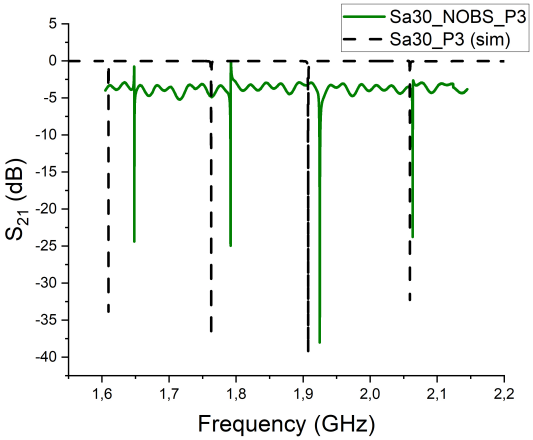

Figure 5.15: Measured (green) and simulated (black dashed) resonances for the Prototype 3 configuration deposited on the 330 μm sapphire substrate - 30 nm NbN thick film.

kinetic inductance value and the general lower quality of the thin film is immediately apparent, with much shallower resonances occurring at lower frequency when compared to the thicker deposition samples. The 5 nm films present the highest value of L_k among all the produced detectors at 30.33 $pH/\square$, analogous to 28.5 $pH/\square$ associated to the thicker films deposited on silicon. Their resonance frequencies are within comparable ranges as are their depths. Figure 5.15 shows the measurements performed on the 30 nm thick film sample. In this case, the resonances are deeper and the frequencies are shifted toward higher values. The calculated L_K is 3.33 $pH/\square$ and represents the lowest value associated to the deposited NbN films. The baseline signal structure is nevertheless rougher than what can be observed in fig. 5.12, indication of a stronger impedance mismatch at the input of the feedline. In any case, the simulations were able to correctly predict the resonance frequencies of the resonators within a good margin of precision.

5.2.2.1 Backshort detectors

As previously mentioned, four different batches of backshort detectors were produced, each with different thickness of the NbN film and the composition of the underlying ground plane. The deposition was performed at room temperature, at a thickness of 400 nm. The preparation of the samples for the measurements include a cleaning phase into ultrasonic baths of hexane first and then acetone, followed by rinsing with 2-propanol to remove any residue of the solvent. During this phase, the Nb layer started to flake away, leaving large portions of the backside of the detectors uncovered. The room temperature deposition in addition to the lattice mismatch between Nb and sapphire resulted in the backshort starting to peel off under the vibrations induced by the ultrasonic bath. The Au backshorts, on the contrary, displayed a good adherence to the substrates with no flaking. Even though the deposition of gold was also performed at room temperature, this material has a lattice constant equal to 4.065 Å, which represents a closer match to that of sapphire when compared to niobium. The measurements were therefore performed only on the gold sputtered samples. Figure 5.16 shows the resonances of one of the 13.3 NbN nm thick film sapphire prototypes endowed with a gold backshort. When compared to the measurements performed on the backshort-less

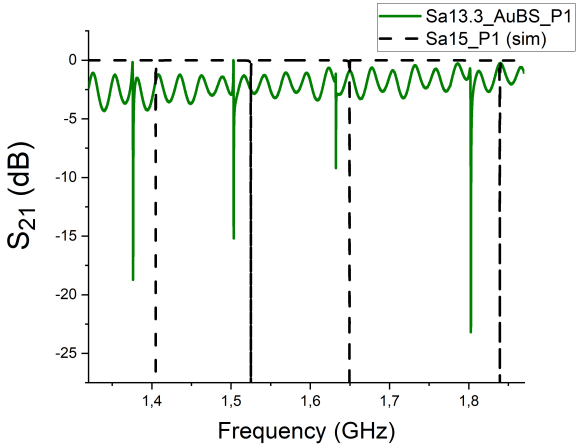

Figure 5.16: Measured (green) and simulated (black dashed) resonances of the Prototype 1 configuration deposited on the 330 μm sapphire substrate - 13.3 nm NbN thick film, Au backshort.

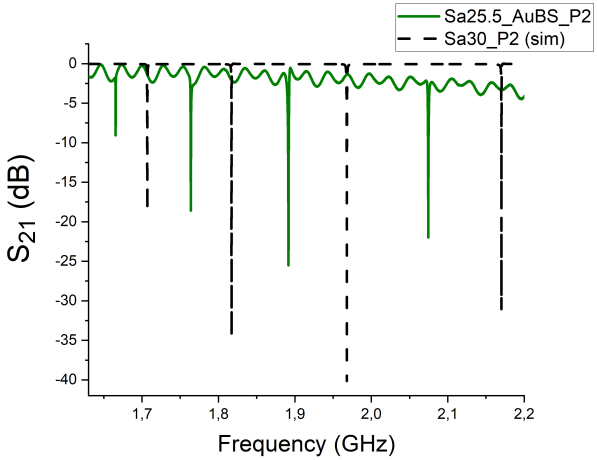

Figure 5.17: Measured (green) and simulated (black dashed) resonances for the Prototype 2 configuration deposited on the 330 μm sapphire substrate - 25.5 nm NbN thick film, Au backshort.

prototype (Fig. 5.12), a larger difference between the simulated and measured values can be observed. Additionally, the resonances have a reduced depth and the baseline signal shows a stronger presence of the periodic structures associated with the impedance mismatch. These aspects can be partially explained by taking into consideration the increased kinetic inductance of the thinner film, 7.57 pH/□ for 13.3 nm vs. 7.28 pH/□ for 15 nm, leading to increased impedance mismatch. An additional factor to take into consideration is the presence of a conductive sticking agent in the form of electrically conductive silver-based grease in-between the backshort and the copper ground base of the detector box. Analogous measurements on the rest of 13.3 nm samples and on the 25.5 nm ones (Fig. 5.17) confirm this general degradation of the performances. To verify this hypothesis the measurements of the backshort-less prototypes, previously carried on with non-electrically conductive vacuum grease, were repeated, this time with the silver paste as contact medium. Results for the 15 nm and 30 nm films can be observed in figs. 5.18 and 5.19. The difference in performances between the measurements with the two different thermal interface media is immediately

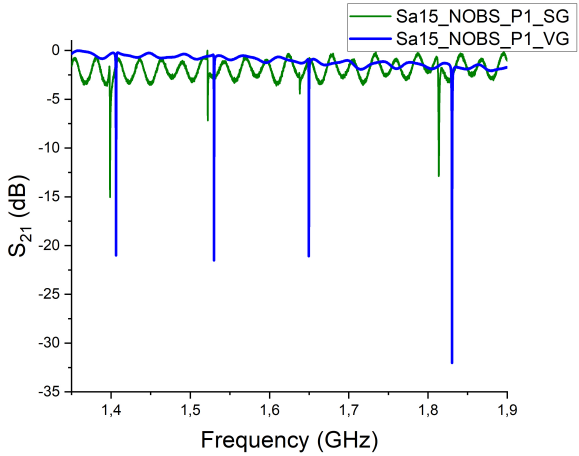

Figure 5.18: Measured resonance response for sapphire prototype 1 - 15 nm thick film interfaced with the detector box through dielectric vacuum grease (VG, blue line) and silver-based thermo-electro conductive paste (SG, green line).

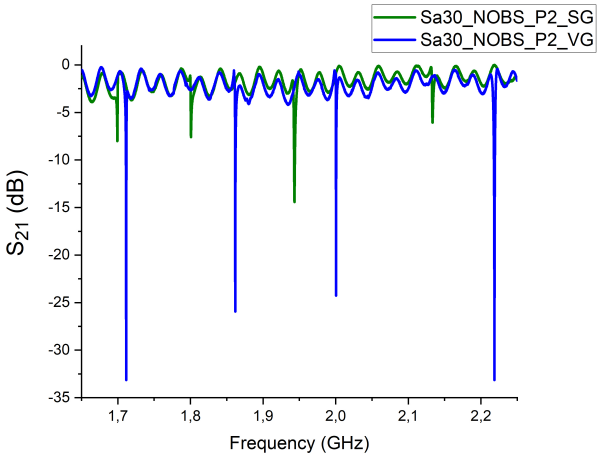

Figure 5.19: Measured resonance response for sapphire prototype 1 - 30 nm thick film interfaced with the detector box through dielectric vacuum grease (VG, blue line) and silver based thermo-electro conductive paste (SG, green line).

apparent, especially in the case of the thinner films. Silver based thermal compounds have high thermal transmission properties, and consist of micronized silver, boron nitride, zinc oxide and aluminum oxide particles suspended in ester oil blends [131]. The presence of metals in the contact medium, while boosting the thermal properties, also allows for the conduction of electrical currents. On the other hand, by their own nature, they introduce large capacitances between the backshort and the grounded base of the detector box, decreasing the resonators frequency and altering the dynamics of the equivalent circuit. A possible solution to be employed in the future is represented by highly ductile indium foils [132]. While the latter technique foregoes the problems related to parasitic capacitances, it requires a substantial clamping force (in the order of 450 N) to insure a good mechanical contact between the surfaces to be interfaced and the indium, requiring a re-design of the the detector box.

5.2.3 Diamond substrate

Figure 5.20 shows the results of the resonance measurements performed on the diamond substrate prototype (configuration 3) with the NbN thin film, together with the predicted dips obtained from the simulations in Sonnet. It can be immediately seen how in the measurements the first order resonances that characterize the simulations are completely missing. While the bandwidth of the VNA was initially limited to a range that was meant to encompass the predicted resonance values (roughly between 1.2 and 1.65 GHz), the frequency scanning range was extended for these measurements, finding the peaks between 3.6 and 4 GHz. These higher order modes present very shallow and wide resonances, with very low Q values in the order of the hundreds (table 5.2), well below those predicted by the simulations shown in chapter 3 (fig. 3.25 and 3.28). A Sonnet analysis extended toward 6 GHz (fig. 5.21) shows the presence of high order modes roughly between 5.1 ad and 5.35 GHz, well above the measured ones. Fig. 5.22 shows the current density distribution obtained from the Sonnet analysis relative to the four higher mode resonances. It is evident that these resonances are collective, involving all

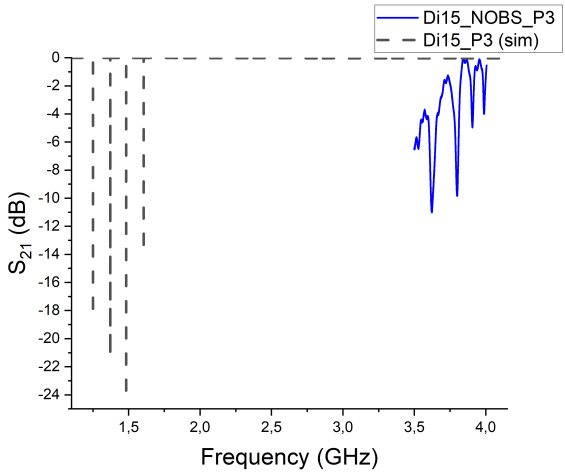

Figure 5.20: Measured (blue) and simulated (black dashed) resonances for the Prototype 3 configuration deposited on the 700 μm diamond substrate - 15 nm NbN thick film.

Table 5.2: Measured quality factors of the four resonance peaks of the Prototype 3 configuration deposited on the 700 μm thick diamond - 15 nm NbN film.

Peak	Q_L	Q_C	Q_0
1	106	192	238
2	117	117	315
3	147	371	245
4	478	1295	757

the detectors at the same time. It can also be seen how the resonators are excited by a standing wave regime within their inductive structures, analogously to what happens, for example, with quarter-wavelength resonator. In these conditions, the detectors lose their lumped elements qualities and behave like distributed detectors, with a position-dependent response [133]. In order to explain the differences between the measured and simulated resonances, the validity range of equation 5.1 needs to be taken into account: the equation represents an approximation for $T \ll T_C$. While with the sapphire and silicon samples this condition is satisfied, resulting in a 10-15 $\%$ difference between the values calculated and those used in the final simulations, the same cannot be said for the films on diamond, given their much lower transition temperature. Therefore, eq. 5.1 underestimates the kinetic inductance. A new set of parametric simulations revealed higher order resonances in the same position of the measured ones for L_k equal to 40.5 pH/$\square$, almost double of what was previously computed. With this new value, the simulated first order resonances end up shifting to a range between 0.9 and 1.2 GHz. Measurements applied to this new frequency interval did not return any visible dip. Their disappearance can be attributed to high resonator internal losses due to the increased population of quasi-particles, resulting in dips so shallow to end up embedded within the base signal and, therefore, undetectable.
The diamond prototypes with the 15 and 30 nm pure niobium thin films were also measured, but didn't show any detectable resonance, given the even lower transition temperatures measured during the characterization measurements (Fig. 5.7) and the associated higher internal losses.

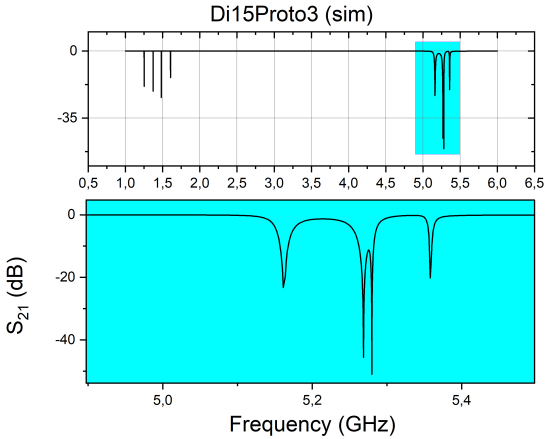

Figure 5.21: Extended-band simulation of the prototype 3 configuration over diamond substrate - 15 nm thick NbN film. The upper panel shows the entire frequency range of the simulation, while the lower panel shows a zoom of the higher order mode resonances. The two central resonances partially overlap.

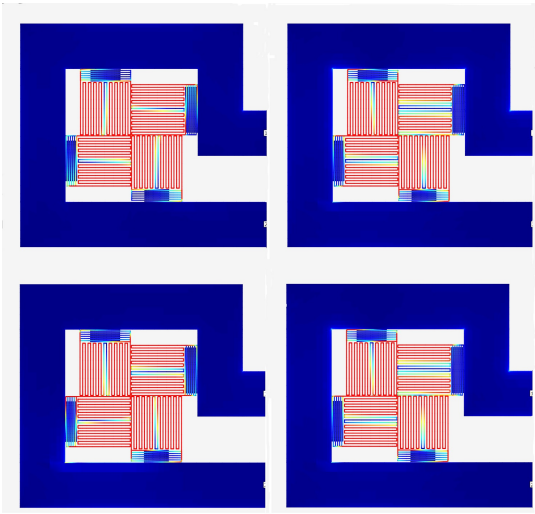

Figure 5.22: Qualitative representation of the current density distribution of the four higher order modes shown in fig. 5.21. Dark blue elements present no current, with increasing values of j associated to yellow and red zones.

5.3 Detectors optical response

The last batch of measurements performed on the KIDs consisted in recording the response of the detectors to incoming radiation in the THz range. The measurements aimed at estimating the responsivity of the detectors, checking the cross-polarization rejection factor and evaluating the noise level of the detectors. In the following sections, the employed setup is first described in detail, and the results of the measurements are then shown.

5.3.1 Setup

The source employed consisted in a backward wave oscillator (BWO) coupled to a Schottky diode frequency tripler, capable of fully tunable emission from 650 GHz up to 1.16 THz. The source was operated at 900 GHz, since it corresponds to the maximum emitted power with the tripler installed (Fig. 5.23). A maximum emitted power of around 47 μW was measured, significantly lower than the 61 expected from the data sheet provided by the source manufacturer but deemed sufficient to induce a response from the prototypes. The quasi-optical system consisted of 5 main elements: the source, two elliptical focusing mirrors, a chopper operated at 23 Hz and the cryostat (Fig. 5.24). The cryostat itself was placed on a manual XYZ linear translation stage for fine position tuning. A room temperature signal amplifier was interposed between the output of the cryostat and the VNA. The cryostat is a two-stage, single chamber model with a reservoir of approximately 2 liters capacity. The radiation input window had an effective aperture of approx 2.54 cm and was equipped with a teflon IR low-pass filter with a cut-off frequency of 10 THz. For the cross-polarization measurements, a wire grid polarizer was employed. After being pumped down to a base pressure of around 10^{-6} mbar, a pre-cooling phase with liquid nitrogen was performed, letting the whole system thermalize for a night. Once an internal temperature of 77 K was reached, the reservoir was emptied of the liquid nitrogen and refilled with liquid helium. Particular care was taken to completely dry out the reservoir in between the two cooling phases to avoid the formation of nitrogen ice that would

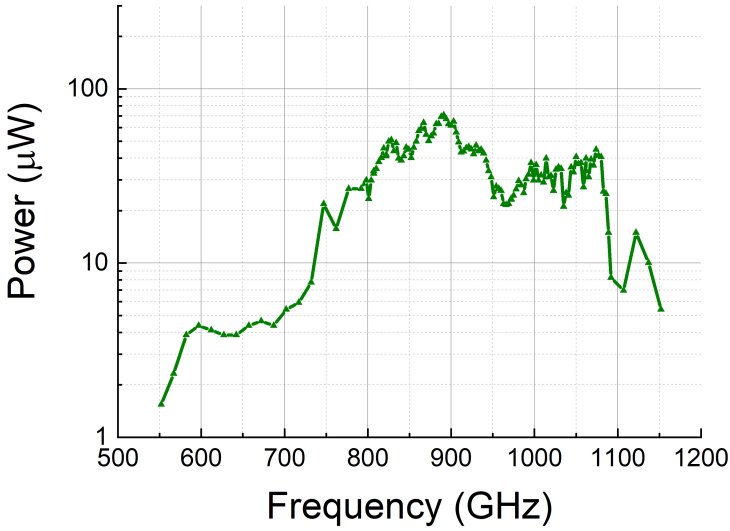

Figure 5.23: Emission power spectrum of the employed BWO source.

have greatly degraded the thermal properties of the device. The copper cold plate of the cryostat consisted in a 10x10 mm^2 M4 grid onto which the various components were secured with screws. The detector box was mounted in a vertical position, with the box cover in direct contact with an adapter plate, necessary to raise the center of the box window on the same level as the center of the cryostat window (Fig. 5.25). A heater and a thin film RTD ceramic temperature sensor were placed on opposite sides of the detector box. Thermally conductive vacuum grease on the various contact surfaces existing between the various components of the system was employed to obtain good thermal interfaces. Two cryogenic attenuators (-10 and -20 dB) were attached to the input SMA plug to limit thermal noise from the 300 K stage. A cold 27 dB amplifier, with a 1 - 6 GHz operational bandwidth was then inserted at the output port of the detector box through a semi-rigid SMA cable.

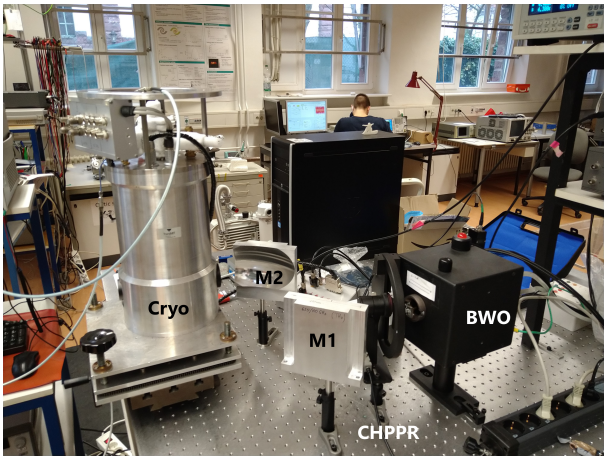

Figure 5.24: Quasi-optical setup employed in the measurements. Visible in the photo, the BWO source, the chopper (CHPPR) and the two mirrors (M1 and M2) used to steer the beam toward the cryostat (Cryo).

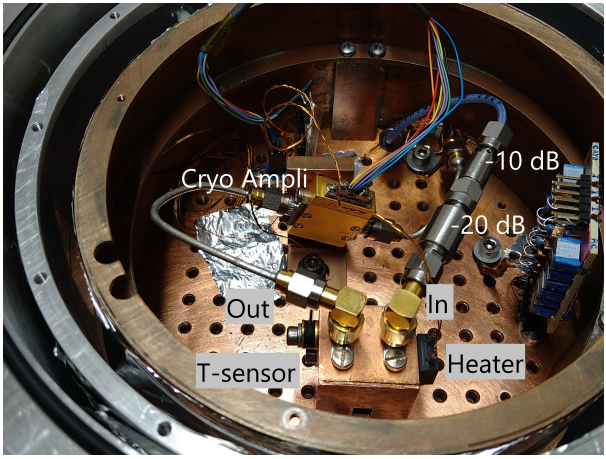

Figure 5.25: Photo of the inside of the cryostat used for the quasi-optical characterization of the KIDs. Visible are the attenuators (upper right), the detector box equipped with temperature sensor and heater (bottom center) and the cold amplifier (top center).

5.3.2 Measurements and discussion

The optical measurements were performed on two samples, one with the sapphire substrate and one with a diamond one. Taking into consideration the previous resonance measurements, the backshort-less sapphire prototype 1 and the diamond prototype 3, both with 15 nm thick NbN films, were chosen. With the setup described in section 5.3.1 and after assessing the losses due to filtering and alignment, a total power of 20 μW at 900 GHz falling on the detector was estimated. Figures 5.26 and 5.27 show the resonances measured before the actual optical response characterization of the samples. The detectors were also under illumination from the background shining through the cryostat window. While the sapphire prototype shows very sharp and well defined resonances, the same cannot be said for the diamond detector, with a very shallow and extremely wide single resonance peak. The measurement on the diamond prototype was performed at a temperature of 5.5 K, the minimum temperature that was possible to reach during the test. This additionally increased the losses of the resonators and made it so that all the resonances except one disappear into the baseline of the signal, similarly to

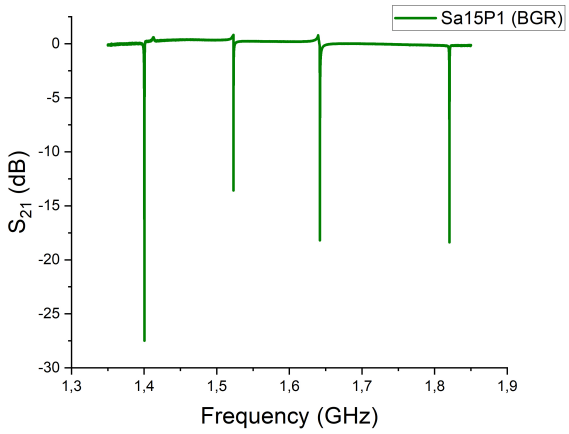

Figure 5.26: Resonance measurements of the sapphire prototype 1 - 15 nm thick NbN film under optical background load.

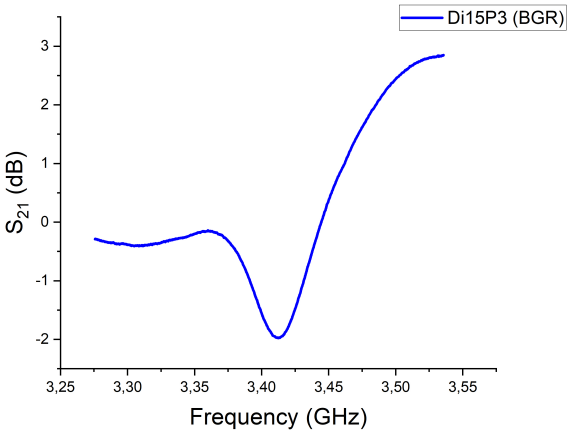

Figure 5.27: Resonance measurements of the diamond prototype 3 peak 1 - 15 nm thick NbN film under optical background load.

what happened to the first order peaks during the measurements shown in section 5.2.3.

Fig. 5.28 shows the response obtained by one of the pixels of the sapphire prototype, while in fig. 5.29 the analogous measurement performed on the diamond sample is reported. The measurement on the sapphire sample was performed at the temperature of 4.5 K. The responsivity is in the order of 0.1 degs/ μW, while the response time scale is in the order of 6 ms, as determined by an exponential decay fit over the recorded trace. The dynamics of generation and recombination of Cooper pairs is generally much faster, with time constant as low as a few nanoseconds [23]. For superconducting micro-resonators, an indication of the detector response time is given by the ring down time τ, itself a function of the resonance frequency ν_0 and loaded quality factor Q_L:

$$\tau = \frac{Q_L}{\pi \cdot \nu_0} \tag{5.2}$$

The pixel to which fig. 5.28 refers to has a resonance frequency equal to 1.4 GHz and a measured Q_L in the order of 2000. Substituting this into eq. 5.3.2

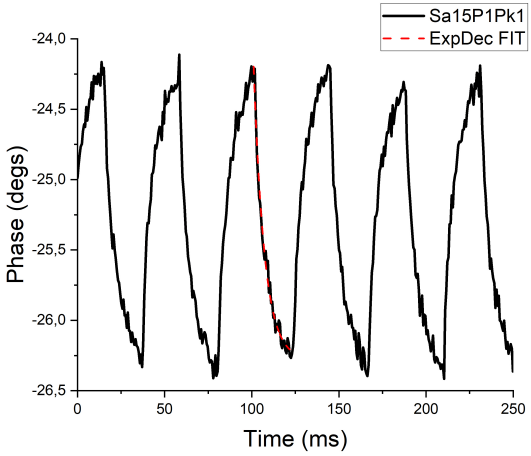

Figure 5.28: Phase response of one of the pixels of the Prototype 1 realized on a sapphire substrate - 15 nm thick NbN film. The red dashed line indicates the exponential decay fit performed on one of the peaks to determine the ring-down time of the resonator.

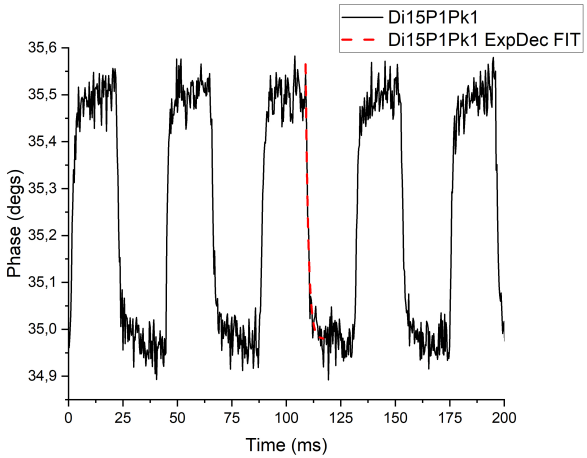

Figure 5.29: Phase response of one of the pixels of the Prototype 3 realized on the diamond substrate - 15 nm thick NbN film. The red dashed line indicates the exponential decay fit performed on one of the peaks to determine the ring-down time of the resonator.

leads to a response time around 440 ns. The time scales measured are more in line with a bolometric effect than a kinetic inductance one [134]. The change in quasi particle density is due to the heat up - cool down cycle induced by the radiation impinging onto the detector rather than to the direct breakage of the Cooper pairs. This hypothesis is confirmed by the measurements performed on the diamond sample, showing a time scale in the order of 1 ms. These results demonstrate the compliance of the produced detectors with the ITER requirement of having a measurement of the plasma-current profile with a time resolution better than 10 ms [61]. The responsivity shown by the diamond sample is lower than what we recorded with the sapphire sample, with a value of roughly 0.03 degs/ μW, due to the additional losses related to the lower quality NbN film and higher measurement temperature. Noise measurements can be seen in figures 5.30 and 5.31. The noise level is higher than expected and mainly due to a higher generation-recombination events frequency in the superconductor, result of the measurements being performed, in both cases, at relatively high temperatures.

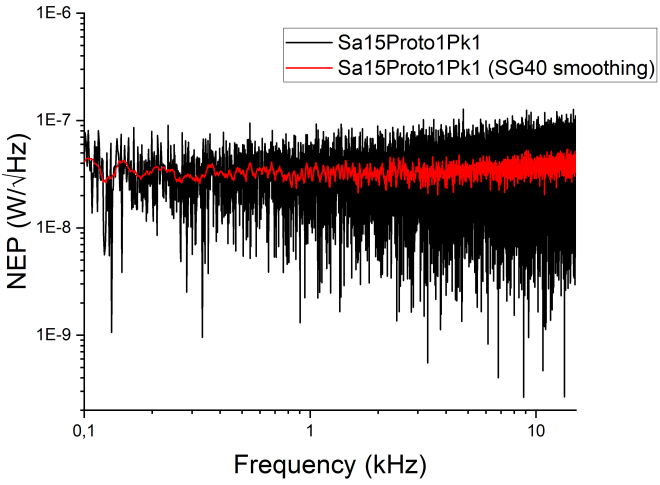

Figure 5.30: Noise power spectrum for the sapphire prototype 1 - 15 nm NbN film sample. In black, the measured values and in red the corresponding Savitzky-Golay smoothing.

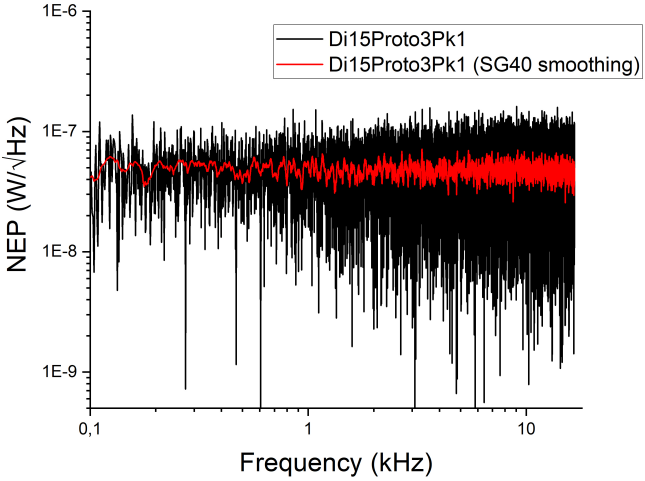

Figure 5.31: Noise power spectrum for the diamond prototype 3 - 15 nm NbN film sample. In black, the measured values and in red the corresponding Savitzky-Golay smoothing.

Noise levels are in any case low enough to allow the detection of power levels much lower than what is expected to be implemented in the final instrument (see section 2.4). Figure 5.32 shows the response of a single pixel of the sapphire prototype 1 to two perpendicular polarization directions of the incoming light. The polarization selector was composed by the wire grid polarizer, preceded by a wave-plate, since the BWO is a coherent light source. As can be seen from fig. 1.8, to every 'long' element of the inductive part, a short connecting segment is associated. The ratio between the lengths of these two elements is 25:1, therefore the contribution to the absorption of the small transverse elements is negligible. The design of the detectors is effective in rejecting cross-polarizations and therefore the concept of a polarimeter based on this technology is valid. This also serves as proof that the bolometric response is taking place in the thin film and not in the substrate. If the substrate was the main radiation absorber, radiation would be detected independently from the presence of a polarizer, since the substrate itself is not polarization selective.

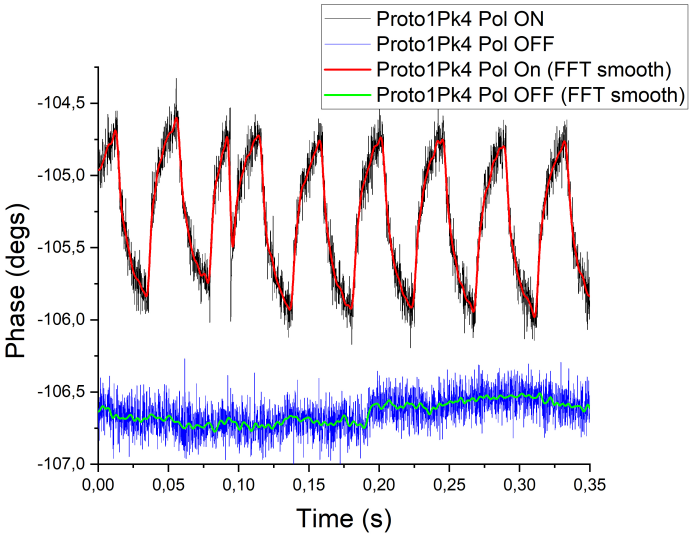

Figure 5.32: Phase response of the sapphire prototype 1 - 15 nm NbN film to two different polarization states. In black, the response for polarization with direction parallel to the inductance main lines, in blue the one for perpendicular polarization. Both tracks were smoothed out with a FFT algorithm for clarity purposes.

6 Polarimeter Configuration Outlook

In this chapter, the general configuration of the polarimeter is presented. Polarimetric systems may, analogously to interferometric systems, come in a wide variety of configurations. A few examples include the dual photo-elastic modulator system installed at the JT-60 machine [135], the Dudel-Kunz method of contra-rotating circularly-polarized beams found in the Large Helical Device (LHD) [136] and a hybrid interferometric-polarimetric system installed at the Joint European Torus (JET) [137]. Recently, a much simpler scheme based on a rotating waveplate method was proposed by Imazawa et al. [61] for installation at the upcoming ITER machine. In general, the chosen design should maximize reliability and stability, while minimizing the down-time required for inspection and maintenance. The main issues for current polarimetric systems are the reliability of the laser employed as source and of its mechanical components. Additionally, hybrid interfero-polarimetric systems, like those installed on JET and LHD, suffer from the presence of vibrations and need to be placed on active vibration damping platforms.

Given these premises, a pure polarimetric system with few moving parts and inexpensive, easily replaceable components was selected. One of the main requirements for such an instrument is its capability to cover multiple lines of sight in order to characterize the plasma current profile along the whole cross section of the torus. For multiple devices to be installed without an excessive footprint, a compact design is necessary. The QCL is an inexpensive and virtually maintenance-free source operating in the THz region, with dimensions in the order of the square millimeter. The KIDs themselves are extremely simple devices, requiring only a single deposition process on the substrate and hundreds of such

pixels can be produced in a single photolithographic process. Their polarization sensitiveness also means that a polarization selection stage is not necessary, further simplifying the hardware requirements. Fig. 6.1 shows a schematic view of the envisioned device. Its basic components are the source (QCL), a detector (KID), a chopper and a retro-reflector installed on the inner wall of the tokamak chamber. The only mechanical component present is the chopper electric motor. The 10 ms maximum time resolution specified by the ITER requirements [61] translates to rather low chopping frequencies. Low-RPM motors, less subject to mechanical stress, can therefore be used. The laser itself can be operated in either continuous wave (CW) or pulsed regime, giving an additional degree of freedom when it comes to modulating the intensity of the probe beam. As can be seen in fig. 6.1, the beam performs a complete round trip inside the plasma, bouncing from the retro-reflector back to the detector. A back-and-forth passage through a circularly birefringent medium would only in appearance result in a net rotation equal to zero, but this is not the case, since the Faraday effect is a rare case of non-reciprocal optical propagation [138]. In an optically-active medium, like a linearly birefringent crystal, the rotation is only dependent on the direction of propagation. Therefore after reflection a counter clock-wise motion becomes clock-wise and vice versa, returning the polarization to its original state. The Faraday effect, on the other hand, is dependent on the presence of a magnetic field and its orientation relative to the propagation vector. Upon plane reflection, the wave experiences opposite rotation sense relative to the direction of propagation, that is also reversed. The end result is that after a round trip inside the plasma, a double rotation is obtained.

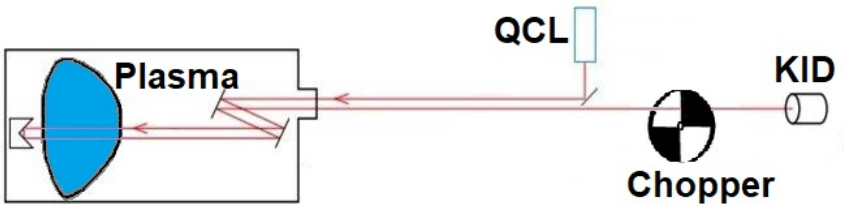

Figure 6.1: Simplified schematic representation of the single detector polarimeter.

Given the placement and orientation of the KIDs resonators (section 3.2), it is of the maximum importance to have a uniform beam profile density precisely centered at the center of the pixels. The beam emitted by QCLs is normally characterized by large divergences at the output and highly non-Gaussian spatial modes, given that the lasing structures inside the laser and the generated wavelengths are of comparable dimensions. In these conditions, diffraction effects are dominating, resulting in divergence angles as large as 120° [139] and very disordered far-field modes. A way to improve the beam pattern of the QCL is to use collimating silicon lenses [139–141] coupled to the output side of the laser chip (fig. 6.2 [139]). The beam quality must be preserved as the radiation travels first toward the plasma and then toward the KID.
Transmission and beam delivery of THz signals was first performed through free-space quasi-optical systems. This has two notable drawbacks in the bulk of the required optical elements and in the absorption of THz radiation from the water vapor present in the air [142]. Since the THz radiation is placed in-between the microwaves and IR-optical ranges, both very well understood and characterized by the presence of established technological tools, the first attempts to manufacture dedicated THz transmission lines drew inspiration from these technologies, scaling up or down devices dedicated to the mm-wave or optical regimes. Hollow-core metallic waveguides are plagued by heavy ohmic losses due to the high frequency

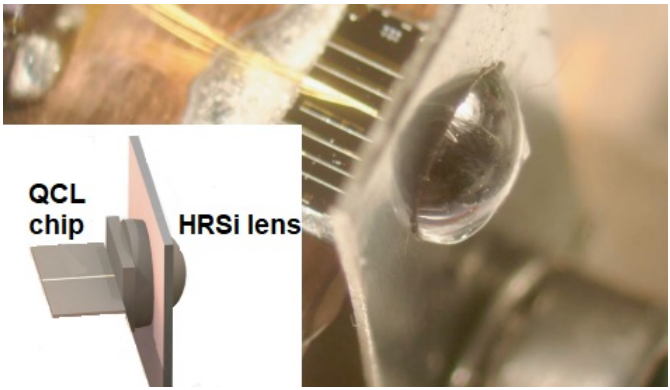

Figure 6.2: Double metal waveguide QCL THz quantum cascade laser coupled to a collimating silicon lens.

of the radiation being transmitted. While increasing the dimensions of the metal structures composing the transmission line can mitigate the problem, it opens the door to the presence of parasitic higher order modes that end up lowering the beam profile quality. On the other end, fiber optics suffer from losses in the dielectric composing their core. In an effort to find a balanced trade-off between flexibility, single-mode operation and attenuation of the signal, a wide variety of metallic and dielectric waveguides were designed and studied [143], showing promising features. Nazarov et al. [144] have recently demonstrated the improvements in beam quality of QCL radiation when injected into a specially designed micro-structured hollow-core polymer waveguide (tube lattice fiber, TLF). The TLF is shown to have a very good transparency (7 dB/m), low dispersion and high rejection of side-bands and parasitic modes. These fibers are capable of transmitting narrow-band frequency signals with a Gaussian like profile and represent an ideal solution to be implemented in the system.

7 Summary and Conclusions

This work was aimed at designing, studying and producing the first prototypes of kinetic inductance detectors specially tailored for polarimetric applications in the terahertz range. The final application of these proof-of-concept devices is to be the detecting component of a polarimeter to be employed as plasma diagnostic for a nuclear fusion reactor. Two well established substrate materials (silicon and sapphire) and additionally diamond were looked into in this study. Diamond was considered and investigated in this innovative role for the first time, potentially widening the detectors properties range. Superconducting thin films were obtained with depositions of NbN and Nb. The first step that was undertaken consisted in a numerical modelization of the plasma and its interaction with electromagnetic waves. This led to an estimate of both the optical density of the medium under investigation and the magnitude of the Faraday rotation induced in a probe beam at different wavelengths. The plasma parameters adopted in the first calculations were based on data-sets extracted from ohmic shots performed at the ASDEX Upgrade tokamak in Garching. It was shown that the optimal frequency of a probe beam traveling through a medium with these characteristics was in the low-THz range (sec. 3.1), and the plasma itself maintains a good degree of transparency leading to low absorption factors (sec. 3.1.1). The KIDs were designed as polarization sensitive, four-pixel arrays, with each detecting element tuned to a unique resonance frequency, in order to extract the signal through frequency division multiplexing techniques (sec. 3.2). Detectors with and without backshorts were modeled in order to correctly match them to the incoming radiation and to estimate the required substrate thicknesses (sec. 3.2.1). A wide range of electromagnetic simulations was performed to guide the design of the detectors. The simulations included a study of the tunability of the resonators, an investigation into the potential occurrence of the cross-talk effect and possible employable

methods to limit it and an estimate of the coupling strength between the resonators and the read-out microstrip. A wide range of resonance frequencies was obtained by modifying the interdigital capacitors present in the KIDs, enabling the design of several configurations with good spacing between the various resonance peaks (sec. 3.3.2). This aspect is confirmed in the simulations used to investigate the cross talk effect, with the aforementioned resonance peak spacing limiting the influence of one oscillating resonator onto its neighbors (sec. 3.3.4). This made the use of shielding structures superfluous, also considering the heavy impact that these solutions would have had on the feedline-pixel coupling strengths, as outlined in sec. 3.3.5.

Prototypes of the detectors were produced for proof-of-concept experimental studies. The experimental activity included the characterization of deposited superconducting thin films, an investigation of the response of the detectors to the read out tones and, as last step, a measurement of the response of the detectors to radiation. The characterization of the deposited superconductors shown in sec. 5.1 evidences a large dependence of the thin film characteristics on parameters like the deposition temperature and the lattice mismatch between the deposited NbN layers and the underlying substrate materials. As a consequence, silicon and diamond substrates have shown lower film quality when compared to the sapphire sample. The extracted values of L_k were then used to improve the initial simulations, that were then able to predict the resonance frequencies at the correct position, as is evidenced in sec. 5.2. The resonance measurements served as a confirmation of the data shown in section 3.3.6, with strong influences in the resonances depth and with the quality factors of the resonators being influenced by both the values of the kinetic inductance and the losses occurring in the substrate. The takeaways of the measurements of detector responsivity shown in section 5.3 are the general validity of the polarimetric KID concept as a polarization-sensitive device with sufficient sensitivity for the application it was conceptualized for, even if here it was possible to induce only a bolometric response rather than a process involving direct break-down of Cooper pairs. Sapphire samples displayed the best performances, which is partially due to the vast knowledge about the deposition of thin films on this substrate and the easily replicable, well understood process. The diamond samples showed reduced responsivity performances and suffered mainly

from the low grade of the deposited films. Diamond is nevertheless a promising candidate as substrate for a superconducting detector, given also the superior radiation hardness, thermal, mechanical and optical qualities of this material. This makes it an especially ideal choice in those working environments saturated with radiation that require the detection of low power signals, such as polarimetry as diagnostic for fusion plasmas. Additionally, both sapphire and diamond detectors comply with the requirement for ITER to have a maximum response time of 10 ms.

A future comprehensive additional investigation leading to improved performances of diamond based detectors cannot refrain from, first of all, finding more fitting superconducting materials for the deposition or a dielectric interface layer between the NbN thin film and the substrate to reduce the mechanical strains that result from lattice mismatches. A study of the deposition parameters will have to be performed to identify the range necessary to ensure good film quality and avoid problems like low adhesion and flaking. This work represents, nevertheless, a first investigation of diamond as a substrate for superconducting detectors, and is a first step toward the optimization and final application of this technology.

A Prototypes Simulations

In this section the simulations performed on the pixel combinations not reported in chapter 3 are shown. Table A.1 summarizes the numerical values of the parameters of the substrates and of the thin films that have been employed in the simulations. For the film deposited on diamond, both the parameter extracted from the R/T measurement and the one corrected to take into consideration the lack of validity of Eq. 5.1 are given. Shown in the graphs are the resonances of the complete detectors prototypes together with the resonance peaks relative to the stand-alone pixel. The frequency mismatch is due to additional capacitive effects associated to the surrounding feed-line.

Table A.1: Parameters used to define the substrates and the thin films in the simulations performed within this work. Tanδ indicates the loss tangent, ϵ_r is the dielectric relative permittivity of the substrates and L_k is the value of the kinetic inductance of the film.

Substrate/Film	tanδ	ϵ_r	L_k (pH/□)
Si330-NbN15	10^{-4}	11.9	26
Sa330-NbN15	$5 \cdot 10^{-6}$	10.06	7.3
Sa330-NbN5	$5 \cdot 10^{-6}$	10.06	30
Sa330-NbN30	$5 \cdot 10^{-6}$	10.06	3
Di700-NbN15	10^{-5}	5.67	22.7/40.5

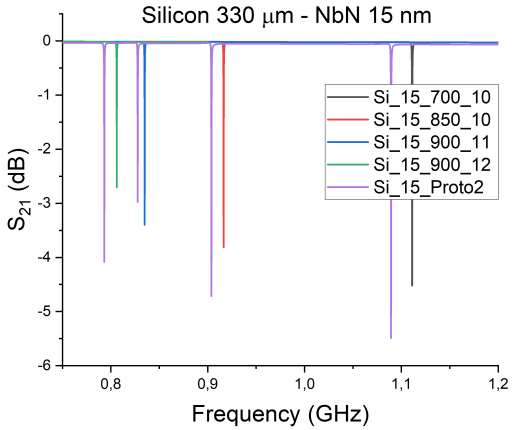

Figure A.1: Sonnet simulation of the Proto2 configuration (purple) on 330 μm thick silicon substrate (15 nm NbN) and of the single pixels composing the complete detector (colored dips).

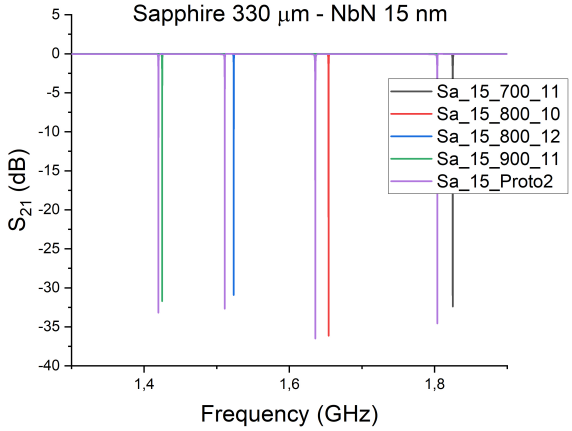

Figure A.2: Sonnet simulation of the Proto2 configuration (purple) on 330 μm thick sapphire substrate (15 nm NbN) and of the single pixels composing the complete detector (colored dips).

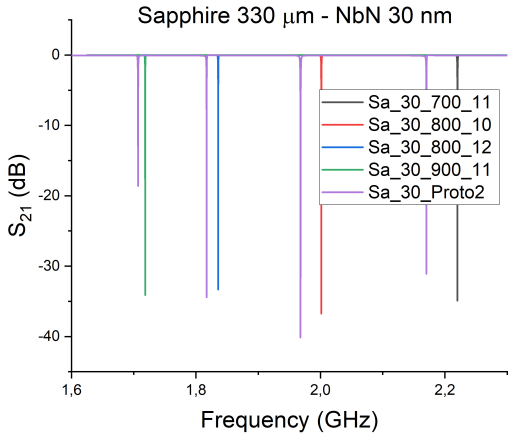

Figure A.3: Sonnet simulation of the Proto2 configuration (purple) on 330 μm thick sapphire substrate (30 nm NbN) and of the single pixels composing the complete detector (colored dips).

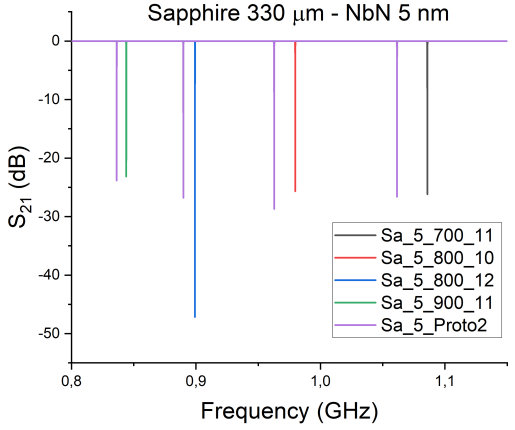

Figure A.4: Sonnet simulation of the Proto2 configuration (purple) on 330 μm thick sapphire substrate (5 nm NbN) and of the single pixels composing the complete detector (colored dips).

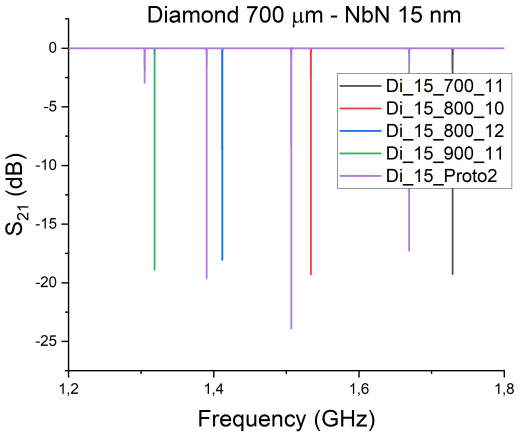

Figure A.5: Sonnet simulation of the Proto2 configuration (purple) on 700 μm thick diamond substrate (15 nm NbN) and of the single pixels composing the complete detector (colored dips).

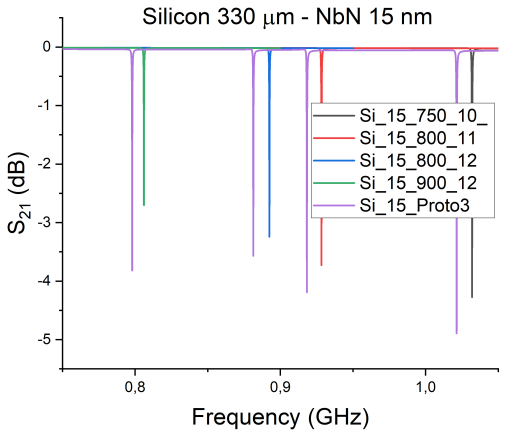

Figure A.6: Sonnet simulation of the Proto3 configuration (purple) on 330 μm thick silicon substrate (15 nm NbN) and of the single pixels composing the complete detector (colored dips).

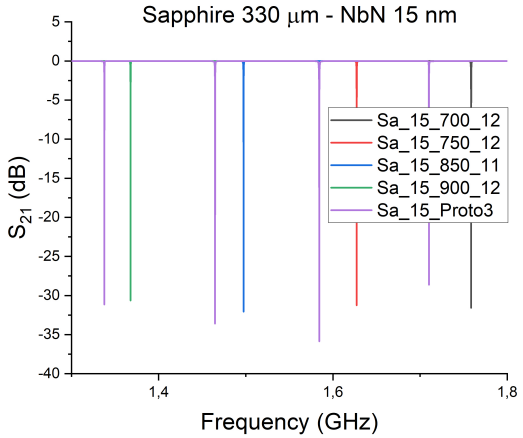

Figure A.7: Sonnet simulation of the Proto3 configuration (purple) on 330 μm thick sapphire substrate (15 nm NbN) and of the single pixels composing the complete detector (colored dips).

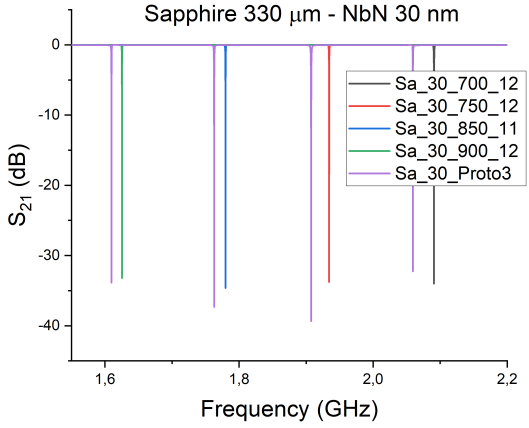

Figure A.8: Sonnet simulation of the Proto3 configuration (purple) on 330 μm thick sapphire substrate (30 nm NbN) and of the single pixels composing the complete detector (colored dips).

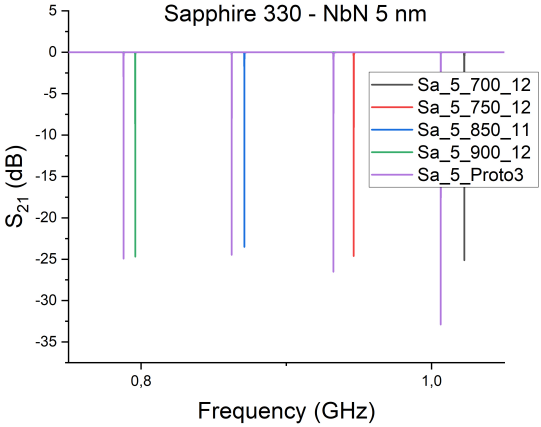

Figure A.9: Sonnet simulation of the Proto3 configuration (purple) on 330 μm thick sapphire substrate (5 nm NbN) and of the single pixels composing the complete detector (colored dips).

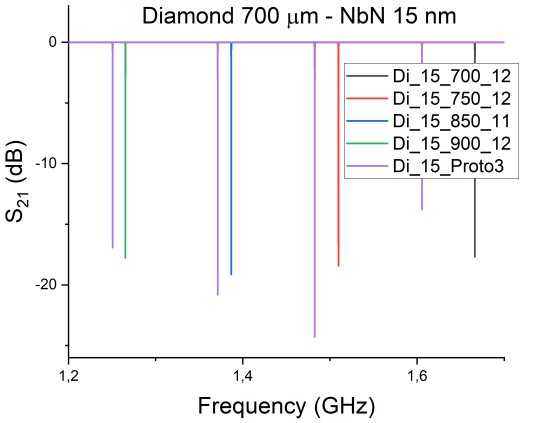

Figure A.10: Sonnet simulation of the Proto3 configuration (purple) on 700 μm thick diamond substrate (15 nm NbN) and of the single pixels composing the complete detector (colored dips).

B Resonance Measurements

In this section the performed resonance measurements that weren't reported in section 5.2 are shown. AuBS refers to the gold backshort of certain prototypes, while SG indicates backshort-less prototypes measured with silver-based vacuum grease as contact agent between the detector and the detector box copper base.

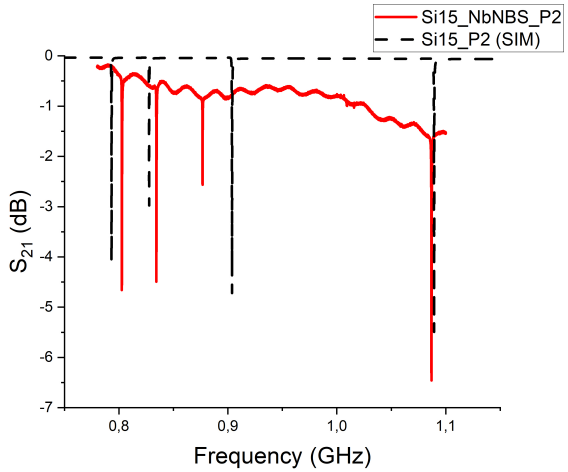

Figure B.1: Measured (red) and simulated (black dashed) resonances of the Prototype 2 configuration deposited on the 330 μm silicon substrate - 15 nm NbN thick film, 400 nm NbN backshort.

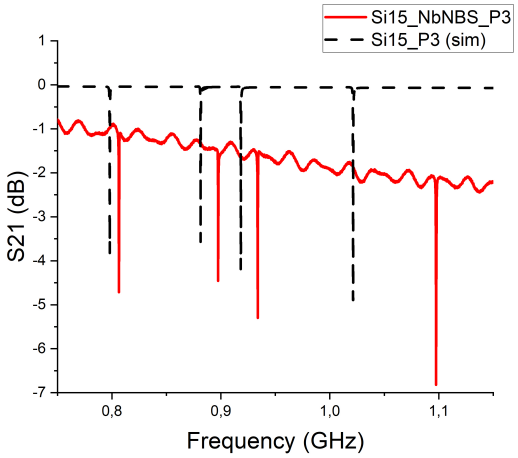

Figure B.2: Measured (red) and simulated (black dashed) resonances of the Prototype 3 configuration deposited on the 330 μm silicon substrate - 15 nm NbN thick film, 400 nm NbN backshort.

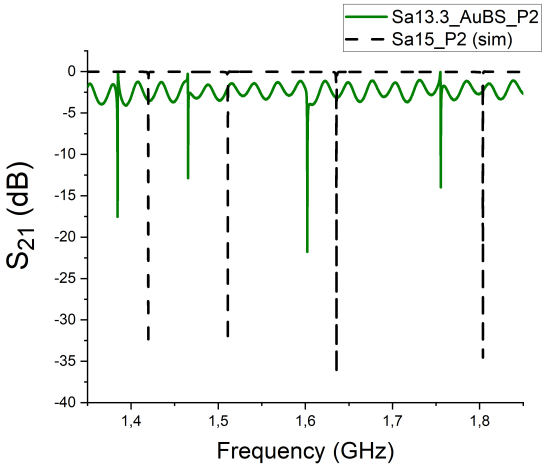

Figure B.3: Measured (green) and simulated (black dashed) resonances of the Prototype 2 configuration deposited on the 330 μm sapphire substrate - 13.3 nm NbN thick film, 400 nm Au backshort.

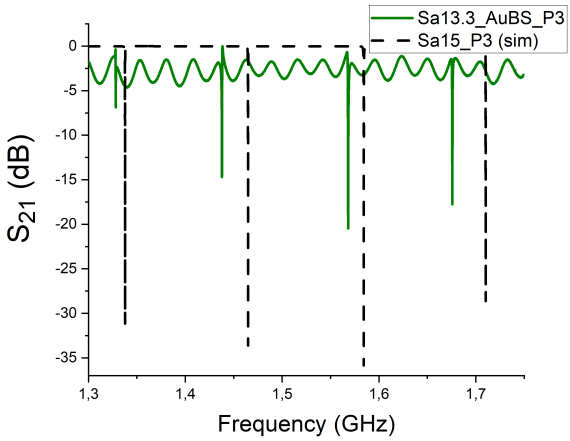

Figure B.4: Measured (green) and simulated (black dashed) resonances of the Prototype 3 configuration deposited on the 330 μm sapphire substrate - 13.3 nm NbN thick film, 400 nm Au backshort.

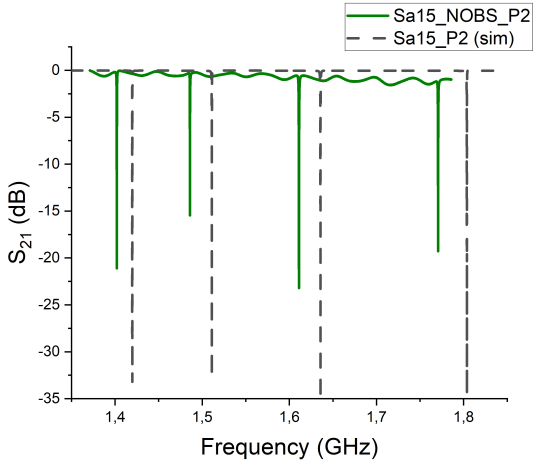

Figure B.5: Measured (green) and simulated (black dashed) resonances of the Prototype 2 configuration deposited on the 330 μm sapphire substrate - 15 nm NbN thick film.

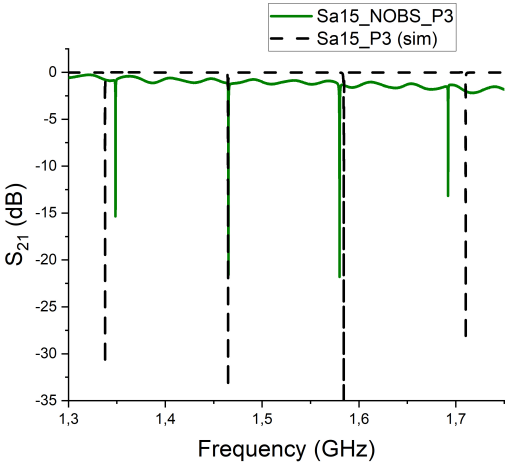

Figure B.6: Measured (green) and simulated (black dashed) resonances of the Prototype 3 configuration deposited on the 330 μm sapphire substrate - 15 nm NbN thick film.

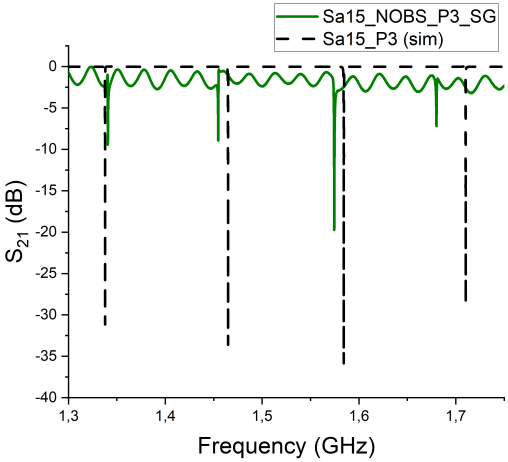

Figure B.7: Measured (green) and simulated (black dashed) resonances of the Prototype 3 configuration deposited on the 330 μm sapphire substrate - 15 nm NbN thick film, silver-based grease contact agent.

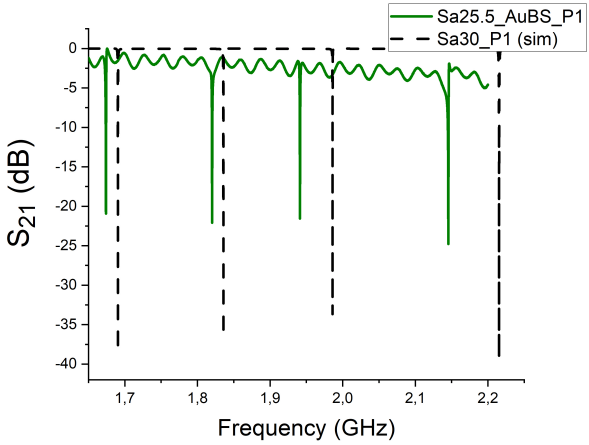

Figure B.8: Measured (green) and simulated (black dashed) resonances of the Prototype 1 configuration deposited on the 330 μm sapphire substrate - 25.5 nm NbN thick film, 400 nm Au backshort.

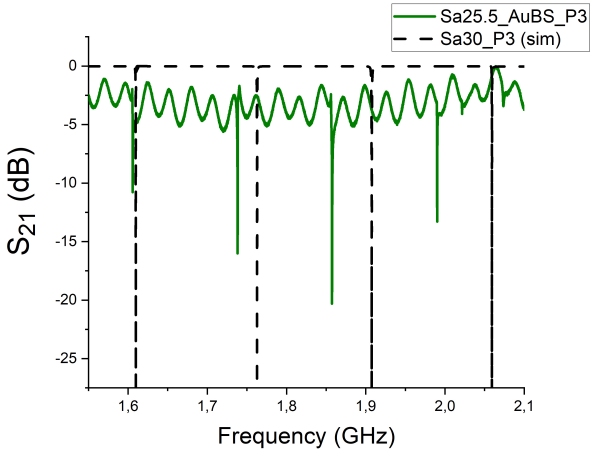

Figure B.9: Measured (green) and simulated (black dashed) resonances of the Prototype 3 configuration deposited on the 330 μm sapphire substrate - 25.5 nm NbN thick film, 400 nm Au backshort.

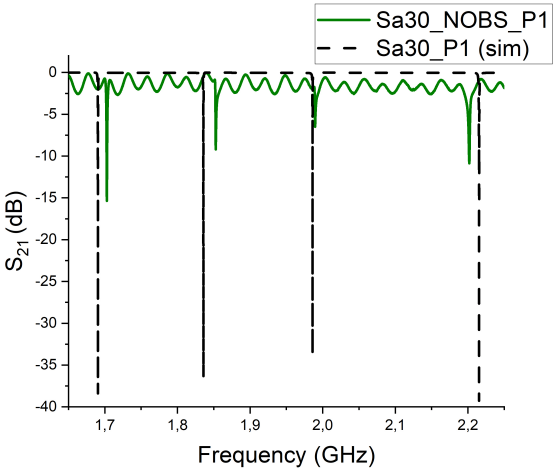

Figure B.10: Measured (green) and simulated (black dashed) resonances of the Prototype 1 configuration deposited on the 330 μm sapphire substrate - 30 nm NbN thick film.

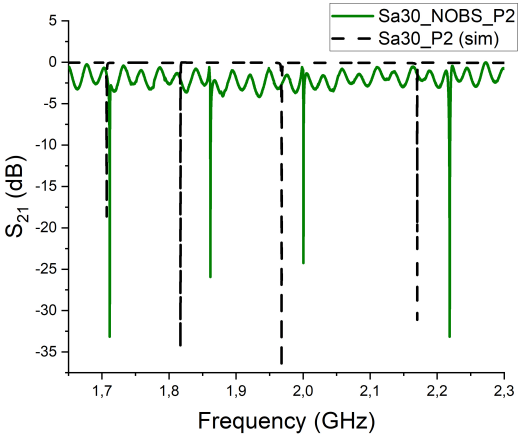

Figure B.11: Measured (green) and simulated (black dashed) resonances of the Prototype 2 configuration deposited on the 330 μm sapphire substrate - 30 nm NbN thick film.

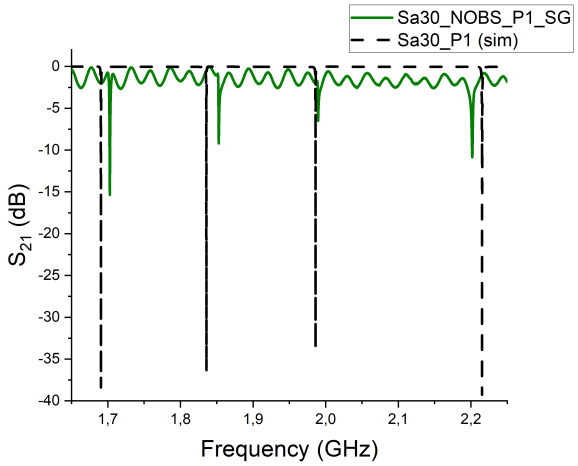

Figure B.12: Measured (green) and simulated (black dashed) resonances of the Prototype 1 configuration deposited on the 330 μm sapphire substrate - 30 nm NbN thick film, silver-based grease contact agent.

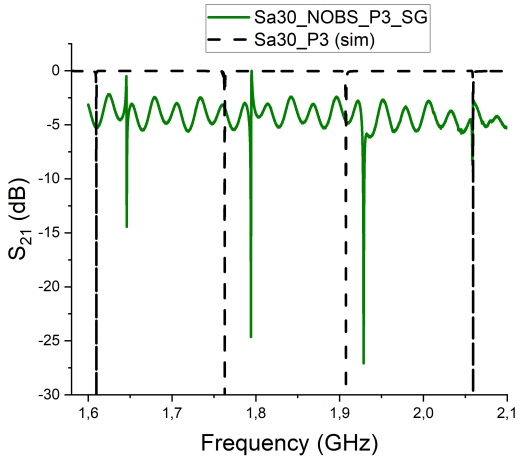

Figure B.13: Measured (green) and simulated (black dashed) resonances of the Prototype 3 configuration deposited on the 330 μm sapphire substrate - 30 nm NbN thick film, silver-based grease contact agent.

List of Figures

List of Tables

List of Publications

Journal Articles

- H. Yamada, A. Meier, F. Mazzocchi, et al., *Dielectric properties of single crystalline diamond wafers with large area at microwave wavelengths.*, Diamond and Related Materials, 58:1–4, 2015.
- F. Mazzocchi, S. Schreck, D. Strauß, et al., *Diamond windows diagnostics for fusion reactors—updates of the design.*, Fusion Engineering and Design, 123:820–824, 2017.
- F. Mazzocchi, G. Grossetti, A. Mlynek, et al., *THz multi line-of-sight polarimeter for fusion reactors.*, Fusion Engineering and Design, 130:1–5, May 2018.
- F. Mazzocchi, E. Driessen, S. Shu, et al., *Design of nbn based kinetic inductance detectors for polarimetric plasma diagnostics.*, IEEE Transactions on Applied Superconductivity, 31(7):1–7, 2021.

Conference Contributions

- F. Mazzocchi, T. A. Scherer, A. Meier, et al., *Loss tangent measurement on synthetic single crystalline diamond (scd) samples.* In 2014 39th International Conference on Infrared, Millimeter, and Terahertz waves (IRMMW-THz), pages 1–2, 2014.

- F. Mazzocchi and T. Scherer, *Diamond window – high power rf transmission and diagnostics*. In 2015 9th international conference on New Diamonds and Nano Carbons (NDNC), 2015.
- F. Mazzocchi, G. Grossetti, A. Mlynek, et al., *Thz qcl based polarimeter for fusion plasma diagnostics.*, in 2017 42nd International Conference on Infrared, Millimeter, and Terahertz Waves (IRMMW-THz), pages 1–1, 2017.
- F. Mazzocchi, G. Grossetti, A. Mlynek, et al., *Thz multi line-of-sight polarimeter for fusion reactors.*, in 2017 2nd European Conference on Plasma Diagnostics, 2017.
- F. Mazzocchi, G. Grossetti, D. Strauß, and T. Scherer. *Thz diagnostics for fusion - a new challenge for dielectric windows.*, in 2017 DPG Frühjahrstagung - Sektion Kondensierte Materie, 2017.
- F. Mazzocchi, E. Driessen, S. Shu, et al., *Development of nbn polarization sensitive kid for fusion applications.*, in 2018 43rd International Conference on Infrared, Millimeter, and Terahertz Waves (IRMMW-THz), pages 1–2, 2018.
- F. Mazzocchi, E. Driessen, S. Shu, et al., *Detailed design of nbn based kinetic inductance detectors for polarimetric diagnostics (invited).*, in 2019 44th International Conference on Infrared, Millimeter, and Terahertz Waves (IRMMW-THz), pages 1–2, 2019.
- F. Mazzocchi, E. Driessen, S. Shu, et al., *Development of kinetic inductance detectors for polarimetric applications in plasma diagnostics.*, in 2019 DPG Frühjahrstagung - Sektion Kondensierte Materie, 2019.
- F.Mazzocchi, D. Strauß, and T. Scherer., *First measurements of nbn based kids for polarimetric plasma diagnostics.*, in 2020 45th International Conference on Infrared, Millimeter, and Terahertz Waves (IRMMW-THz), pages 1–1, 2020.

- F. Mazzocchi, E. Bruendermann, D. Strauß, et al., *Thz detection techniques (invited).*, in IBIC 2020 9th International Beam Instrumentation Conference, 2020.
- F. Mazzocchi, D. Strauß, and T. Scherer, *Development of diamond based kinetic inductance detectors (invited).*, in 2021 DPG Frühjahrstagung - Sektion Kondensierte Materie, 2021.

Bibliography

[1] D. Meadows, J. Randers, and D. Meadows. *Limits to Growth: The 30-Year Update*. Chelsea Green Publishing, June 2004.

[2] K.M. Young and A.E. Costley. An overview of ITER diagnostics. *Review of Scientific Instruments*, 68(1):862–867, 1997.

[3] W. Kunz. First measurement of poloidal-field-induced Faraday rotation in a tokamak plasma. *Nuclear Fusion*, 18(12):1729, 1978.

[4] H. Soltwisch. Current density measurements in tokamak devices. *Plasma physics and controlled fusion*, 34(12):1669, 1992.

[5] Y. Kawano, S. Chiba, and A. Inoue. Infrared laser polarimetry for electron density measurement in tokamak plasmas. *Review of Scientific Instruments*, 72(1):1068–1072, 2001.

[6] A.J.H. Donné. High spatial resolution interferometry and polarimetry in hot plasmas. *Review of scientific instruments*, 66(6):3407–3423, 1995.

[7] W.F. Bergerson, P. Xu, J.H. Irby, et al. Far-infrared polarimetry diagnostic for measurement of internal magnetic field dynamics and fluctuations in the C-MOD tokamak. *Review of Scientific Instruments*, 83(10):10E316, 2012.

[8] L. Zabeo, A. Murari, E. Joffrin, et al. A versatile method for the real time determination of the safety factor and density profiles in JET. *Plasma Physics and Controlled Fusion*, 44(11):2483–2494, October 2002.

[9] H.R. Koslowski and H. Soltwisch. Electron density and q profile measurements with the far-ir interferometer-polarimeter on the TEXTOR tokamak. *Fusion engineering and design*, 34:143–150, 1997.

[10] V. V. Mirnov, D. L. Brower, D. J. Den Hartog, et al. Electron kinetic effects on interferometry, polarimetry and Thomson scattering measurements in burning plasmas (invited). *Review of Scientific Instruments*, 85(11):11D302, November 2014.

[11] P. Belland, D. Veron, and L.B. Whitbourn. Mode study, beam characteristics and output power of a cw 377 μm HCN waveguide laser. *Journal of Physics D: Applied Physics*, 8(18):2113, 1975.

[12] M. Kawamura, I. Okabayashi, and T. Fukuyama. A capacitively coupled RF-excited cw-HCN laser. *IEEE Journal of Quantum Electronics*, 21(11):1833–1837, 1985.

[13] J.B. Zhang, X.C. Wei, H.Q. Liu, et al. Output power stability of a HCN laser using a stepping motor for the EAST interferometer system. *Journal of Instrumentation*, 10(11):C11004, 2015.

[14] Y.G. Li, Y. Zhou, Y. Li, et al. First electron density fluctuation measurement via the HCOOH laser far-forward collective scattering on HL-2A tokamak. *Journal of Instrumentation*, 11(02):C02002, 2016.

[15] C.H. Ma, D.P. Hutchinson, and K.L. Vander Sluis. A modulated submillimeter-laser polarimeter for the measurement of the Faraday rotation by a plasma. *Applied Physics Letters*, 34(3):218–220, 1979.

[16] Y. Zhou, Z.C. Deng, Y.G. Li, and J. Yi. Multi-channel far-infrared HL-2A interferometer-polarimeter a. *Review of Scientific Instruments*, 83(10):10E336, 2012.

[17] A. Mlynek, L. Casali, O. Ford, and H. Eixenberger. Fringe jump analysis and implementation of polarimetry on the ASDEX Upgrade DCN interferometer. *Review of Scientific Instruments*, 85(11):11D408, November 2014.

[18] G. Braithwaite, N. Gottardi, G. Magyar, et al. JET polari-interferometer. *Review of scientific instruments*, 60(9):2825–2834, 1989.

[19] F. Mazzocchi, G. Grossetti, A. Mlynek, et al. THz multi line-of-sight polarimeter for fusion reactors. *Fusion Engineering and Design*, 130:1–5, May 2018.

[20] B. S. Williams. Terahertz quantum-cascade lasers. *Nature Photonics*, 1(9):517–525, September 2007.

[21] Peter K. Day, Henry G. LeDuc, Benjamin A. Mazin, et al. A broadband superconducting detector suitable for use in large arrays. *Nature*, 425(6960):817–821, October 2003.

[22] J.W.M. Baars, B.G. Hooghoudt, P.G. Mezger, and M.Jz. de Jonge. The iram 30-m millimeter radio telescope on pico veleta, spain. *Astronomy and Astrophysics*, 175:319–326, 1987.

[23] M. Tinkham. *Introduction to Superconductivity*. Courier Corporation, January 2004. Google-Books-ID: VpUk3NfwDIkC.

[24] S. Shu, M. Calvo, S. Leclercq, et al. Prototype High Angular Resolution LEKIDs for NIKA2. *Journal of Low Temperature Physics*, 193(3):141–148, November 2018.

[25] G. N. Ramachandran and S. Ramaseshan. Crystal Optics. In S. Flügge, editor, *Crystal Optics · Diffraction*, Handbuch der Physik / Encyclopedia of Physics, pages 1–217. Springer, Berlin, Heidelberg, 1961.

[26] T. G. Campbell, R. A. Nicolaides, and M. D. Salas. *Computational Electromagnetics and Its Applications*. Springer Science & Business Media, December 2012. Google-Books-ID: u7_8CAAAQBAJ.

[27] R. Schneider, B. Freitag, D. Gerthsen, et al. Structural, microchemical and superconducting properties of ultrathin NbN films on silicon. *Crystal Research and Technology*, 44(10):1115–1121, 2009.

[28] J. Baselmans, S. J. C. Yates, R. Barends, et al. Noise and Sensitivity of Aluminum Kinetic Inductance Detectors for Sub-mm Astronomy. *Journal of Low Temperature Physics*, 151(1):524–529, April 2008.

[29] P.J. Koh, W.C.B. Peatman, and T.W. Crowe. Millimeter wave tripler evaluation of a metal/2-DEG Schottky diode varactor. *IEEE Microwave and Guided Wave Letters*, 5(3):73–75, March 1995.

[30] K.S. Krane. *Introductory Nuclear Physics*. Wiley and Sons, 3rd edition, 1987.

[31] R. Aymar. The ITER project. *IEEE Transactions on Plasma Science*, 25(6):1187–1195, December 1997.

[32] J. D. Lawson. Some Criteria for a Power Producing Thermonuclear Reactor. *Proceedings of the Physical Society. Section B*, 70(1):6–10, January 1957.

[33] J. Wesson and D. J. Campbell. *Tokamaks*. OUP Oxford, October 2011. Google-Books-ID: XJssMXjHUr0C.

[34] L. A. Artsimovich. Tokamak devices. *Nuclear Fusion*, 12(2):215–252, March 1972.

[35] L. Spitzer. The Stellarator Concept. *The Physics of Fluids*, 1(4):253–264, July 1958.

[36] N. Holtkamp. An overview of the ITER project. *Fusion Engineering and Design*, 82(5):427–434, October 2007.

[37] L. Wegener. Status of Wendelstein 7-X construction. *Fusion Engineering and Design*, 84(2):106–112, June 2009.

[38] M. Kwon, Y. K. Oh, H. L. Yang, et al. Overview of KSTAR initial operation. *Nuclear Fusion*, 51(9):094006, September 2011.

[39] A. Herrmann and O. Gruber. Chapter 1: ASDEX Upgrade - Introduction and Overview. *Fusion Science and Technology*, 44(3):569–577, November 2003.

[40] Songtao Wu. An overview of the EAST project. *Fusion Engineering and Design*, 82(5):463–471, October 2007.

[41] M. Yoshikawa. The JT-60 project and its present status. *Nuclear Fusion*, 25(9):1081–1085, September 1985.

[42] P. H. Rebut, R. J. Bickerton, and B. E. Keen. The Joint European Torus: installation, first results and prospects. *Nuclear Fusion*, 25(9):1011–1022, September 1985.

[43] A. Iiyoshi, A. Komori, A. Ejiri, et al. Overview of the Large Helical Device project. *Nuclear Fusion*, 39(9Y):1245–1256, September 1999.

[44] Salvatore Mancuso and Steven R. Spangler. Faraday rotation and models for the plasma structure of the solar corona. *The Astrophysical Journal*, 539(1):480–491, August 2000.

[45] E. Munin, J. A. Roversi, and A. Balbin Villaverde. Faraday effect and energy gap in optical materials. *Journal of Physics D: Applied Physics*, 25(11):1635–1639, November 1992.

[46] P.A. Williams, A. H. Rose, G. W. Day, et al. Temperature dependence of the Verdet constant in several diamagnetic glasses. *Applied Optics*, 30(10):1176–1178, April 1991.

[47] N. P. Barnes and L. B. Petway. Variation of the Verdet constant with temperature of terbium gallium garnet. *JOSA B*, 9(10):1912–1915, October 1992.

[48] J. L. Cruz, M. V. Andres, and M. A. Hernandez. Faraday effect in standard optical fibers: dispersion of the effective Verdet constant. *Applied Optics*, 35(6):922–927, February 1996.

[49] M.C. Murdock. Frequency-domain Faraday rotation spectroscopy (FD-FRS) for functionalized particle and biomolecule characterization. In *Materials Science*, 2015.

[50] S. Firdous, M. Fuzail, M. Atif, and M. Nawaz. Polarimetric characterization of ultra-high molecular weight polyethylene (UHMWPE) for bone substitute biomaterials. *Optik*, 122(2):99–104, January 2011.

[51] M. R. Koblischka, N. Moser, B. Gegenheimer, and H. Kronmüller. Determination of flux-density gradients in YBa2Cu3O7-d superconductors using the high-resolution Faraday effect. *Physica C: Superconductivity*, 166(1):36–48, March 1990.

[52] Y. Ikebe and R. Shimano. Characterization of doped silicon in low carrier density region by terahertz frequency Faraday effect. *Applied Physics Letters*, 92(1):012111, January 2008.

[53] A. M. Shuvaev, G. V. Astakhov, A. Pimenov, et al. Giant magneto-optical Faraday effect in hgte thin films in the terahertz spectral range. *Physical Review Letters*, 106(10):107404, March 2011.

[54] K. B. Rochford, A. H. Rose, M. N. Deeter, and G. W. Day. Faraday effect current sensor with improved sensitivity–bandwidth product. *Optics Letters*, 19(22):1903–1905, November 1994.

[55] Y. N. Ning, B. C. B. Chu, and D. A. Jackson. Miniature Faraday current sensor based on multiple critical angle reflections in a bulk-optic ring. *Optics Letters*, 16(24):1996–1998, December 1991.

[56] A. H. Rose, M. N. Deeter, and G. W. Day. Submicroampere-per-root-hertz current sensor based on the Faraday effect in Ga:YIG. *Optics Letters*, 18(17):1471–1473, September 1993.

[57] M.N. Deeter, A.H. Rose, and G.W. Day. Fast, sensitive magnetic-field sensors based on the Faraday effect in YIG. *Journal of Lightwave Technology*, 8(12):1838–1842, December 1990.

[58] T. Yoshino. Compact and highly efficient faraday rotators using relatively low verdet constant Faraday materials. *Japanese Journal of Applied Physics*, 19(4):745, April 1980.

[59] K. Shiraishi, S. Sugaya, and S. Kawakami. Fiber Faraday rotator. *Applied Optics*, 23(7):1103–1106, April 1984.

[60] R. Rosenberg, C.B. Rubinstein, and D.R. Herriott. Resonant optical Faraday rotator. *Applied Optics*, 3(9):1079–1083, 1964.

[61] R. Imazawa, Y. Kawano, T. Akiyama, et al. Polarization measurement techniques suitable for iter poloidal polarimeter. In *Proceedings of the 41st Plasma Physics Conference on Plasma Physics (EPS2014)*, page P5, 2014.

[62] M. Keilhacker. The ASDEX divertor tokamak. *Nuclear Fusion*, 25(9):1045, 1985.

[63] J. Faist. *Quantum Cascade Lasers*. OUP Oxford, March 2013.

[64] H. Li, J. C. Cao, Y. J. Han, et al. Temperature profile modelling and experimental investigation of thermal resistance of terahertz quantum-cascade lasers. *Journal of Physics D: Applied Physics*, 42(20):205102, September 2009.

[65] P. J. de Visser, J. J. A. Baselmans, J. Bueno, et al. Fluctuations in the electron system of a superconductor exposed to a photon flux. *Nature Communications*, 5(1):3130, February 2014.

[66] A. V. Sergeev, V. V. Mitin, and B. S. Karasik. Ultrasensitive hot-electron kinetic-inductance detectors operating well below the superconducting transition. *Applied Physics Letters*, 80(5):817–819, February 2002.

[67] G. Vardulakis, S. Withington, D. J. Goldie, and D. M. Glowacka. Superconducting kinetic inductance detectors for astrophysics. *Measurement Science and Technology*, 19(1):015509, December 2007.

[68] A. Monfardini, A. Benoit, A. Bideaud, et al. A dual-band millimeter-wave kinetic inductance camera for the IRAM 30 m telescope. *The Astrophysical Journal Supplement Series*, 194(2):24, May 2011.

[69] J. Zmuidzinas and P.L. Richards. Superconducting detectors and mixers for millimeter and submillimeter astrophysics. *Proceedings of the IEEE*, 92(10):1597–1616, 2004.

[70] J. Schlaerth, A. Vayonakis, P. Day, et al. A millimeter and submillimeter kinetic inductance detector camera. *Journal of Low Temperature Physics*, 151(3):684–689, 2008.

[71] M. Rösch. *Development of lumped element kinetic inductance detectors for mm-wave astronomy at the IRAM 30 m telescope*. PhD thesis, Karslruhe Institute of Technology, January 2014.

[72] Y. M. Shy, L. E. Toth, and R. Somasundaram. Superconducting properties, electrical resistivities, and structure of NbN thin films. *Journal of Applied Physics*, 44(12):5539–5545, December 1973.

[73] G. Federici, C. Bachmann, W. Biel, et al. Overview of the design approach and prioritization of R&D activities towards an EU DEMO. *Fusion Engineering and Design*, 109-111:1464–1474, November 2016.

[74] B.A. Mazin. *Microwave kinetic inductance detectors*. PhD thesis, Caltech, 2005.

[75] P.E. Stott, G. Gorini, and P. Prandoni. *Diagnostics for experimental thermonuclear fusion reactors 2*. Springer Science & Business Media, 2012.

[76] I. H. Hutchinson. Principles of Plasma Diagnostics: Second Edition. *Plasma Physics and Controlled Fusion*, 44(12):2603–2603, November 2002.

[77] H. Kamerlingh Onnes. The resistance of pure mercury at helium temperatures. *Commun. Phys. Lab. Univ. Leiden, b*, 120, 1911.

[78] W. Meissner and R. Ochsenfeld. A new effect in penetration of superconductors. *Die Naturwissenschaften*, 21:787–788, 1933.

[79] F. London and H. London. The electromagnetic equations of the supraconductor. *Proceedings of the Royal Society of London. Series A-Mathematical and Physical Sciences*, 149(866):71–88, 1935.

[80] J. Bardeen, L. N Cooper, and J.R. Schrieffer. Theory of superconductivity. *Physical Review*, 108(5):1175, 1957.

[81] C.J. Gorter. The two fluid model for superconductors and helium II. In *Progress in Low Temperature Physics*, volume 1, pages 1–16. Elsevier, 1955.

[82] L.N. Cooper. Bound electron pairs in a degenerate Fermi gas. *Physical Review*, 104(4):1189, 1956.

[83] R.G. Sharma. *Superconductivity: Basics and applications to magnets*, volume 214. Springer, 2015.

[84] H. Fröhlich. Theory of the superconducting state. The ground state at the absolute zero of temperature. *Physical Review*, 79:845–856, Sep 1950.

[85] J. Bardeen. Wave functions for superconducting electrons. *Physical Review*, 80:567–574, Nov 1950.

[86] C. Enss and S. Hunklinger. *Low-temperature physics*. Springer, 2005.

[87] V. Ambegaokar. The Green's function method. In *Superconductivity*. CRC Press, 1969.

[88] J. Gao. *The physics of superconducting microwave resonators*. California Institute of Technology, 2008.

[89] Anthony J. Annunziata, Daniel F. Santavicca, Luigi Frunzio, et al. Tunable superconducting nanoinductors. *Nanotechnology*, 21(44):445202, October 2010.

[90] A. B. Pippard and W. L. Bragg. An experimental and theoretical study of the relation between magnetic field and current in a superconductor. *Proceedings of the Royal Society of London*, 216:547–568, 1953.

[91] R.G. Chambers. The anomalous skin effect. *Proceedings of the Royal Society of London. Series A. Mathematical and Physical Sciences*, 215(1123):481–497, 1952.

[92] P. Mangin and R. Kahn. *Superconductivity: An introduction*. Springer International Publishing, 2017.

[93] S. P. Chockalingam, M. Chand, J. Jesudasan, et al. Superconducting properties and hall effect of epitaxial NbN thin films. *Physical Review B*, 77:214503, Jun 2008.

[94] A. Shoji, S. Kiryu, and S. Kohjiro. Superconducting properties and normal-state resistivity of single-crystal NbN films prepared by a reactive RF-magnetron sputtering method. *Applied Physics Letters*, 60(13):1624–1626, March 1992.

[95] D. E. Oates, A. C. Anderson, C. C. Chin, et al. Surface-impedance measurements of superconducting NbN films. *Physical Review B*, 43:7655–7663, Apr 1991.

[96] A. Semenov, B. Günther, U. Böttger, et al. Optical and transport properties of ultrathin NbN films and nanostructures. *Physical Review B*, 80:054510, Aug 2009.

[97] H. Bartolf. *Fluctuation Mechanisms in Superconductors*. Springer, 2016.

[98] A. Kamlapure, M. Mondal, M. Chand, et al. Measurement of magnetic penetration depth and superconducting energy gap in very thin epitaxial NbN films. *Applied Physics Letters*, 96(7):072509, February 2010.

[99] J.D. Jackson. *Classical Electrodynamics 3rd edition*. Wiley and Sons, 1998.

[100] A.P.S. Khanna and Y. Garault. Determination of loaded, unloaded, and external quality factors of a dielectric resonator coupled to a microstrip line. *IEEE Transactions on Microwave Theory and Techniques*, 31(3):261–264, 1983.

[101] J.R. Bray and L. Roy. Measuring the unloaded, loaded, and external quality factors of one-and two-port resonators using scattering-parameter magnitudes at fractional power levels. *IEEE Proceedings-Microwaves, Antennas and Propagation*, 151(4):345–350, 2004.

[102] S. B. Kaplan, C. C. Chi, D. N. Langenberg, et al. Quasiparticle and phonon lifetimes in superconductors. *Physical Review B*, 14(11):4854–4873, December 1976.

[103] K. S. Il'in, M. Lindgren, M. Currie, et al. Picosecond hot-electron energy relaxation in NbN superconducting photodetectors. *Applied Physics Letters*, 76(19):2752–2754, 2000.

[104] C. Yuan, Z. Zhou, X. Xiang, et al. Propagation properties of broadband terahertz pulses through a bounded magnetized thermal plasma. *Nuclear Instruments and Methods in Physics Research Section B: Beam Interactions with Materials and Atoms*, 269(1):23–29, January 2011.

[105] E. F. C. Driessen, F. R. Braakman, E. M. Reiger, et al. Impedance model for the polarization-dependent optical absorption of superconducting single-photon detectors. *The European Physical Journal - Applied Physics*, 47(1), July 2009.

[106] D. Marsden, B.A. Mazin, B. Bumble, et al. Optical lumped element microwave kinetic inductance detectors. In Andrew D. Holland and James W. Beletic, editors, *High Energy, Optical, and Infrared Detectors for Astronomy V*, volume 8453, pages 62 – 70. International Society for Optics and Photonics, SPIE, 2012.

[107] H. Yamada, A. Meier, F. Mazzocchi, et al. Dielectric properties of single crystalline diamond wafers with large area at microwave wavelengths. *Diamond and Related Materials*, 58:1–4, September 2015.

[108] J. Dai, J. Zhang, W. Zhang, and D. Grischkowsky. Terahertz time-domain spectroscopy characterization of the far-infrared absorption and index of refraction of high-resistivity, float-zone silicon. *JOSA B*, 21(7):1379–1386, July 2004.

[109] V. V. Kubarev. Optical properties of CVD-diamond in terahertz range and its applications on the NovoFEL. In *2007 Joint 32nd International Conference on Infrared and Millimeter Waves and the 15th International Conference on Terahertz Electronics*, pages 863–865, September 2007. ISSN: 2162-2035.

[110] H. A. Wheeler. Transmission-line properties of a strip on a dielectric sheet on a plane. *IEEE Transactions on Microwave Theory and Techniques*, 25(8):631–647, Aug 1977.

[111] Erik O. Hammerstad. Equations for Microstrip Circuit Design. In *1975 5th European Microwave Conference*, pages 268–272, September 1975.

[112] I.B. Vendik, O.G. Vendik, and S.S. Gevorgian. Effective Dielectric Permittivity of r-Cut Sapphire Microstrip. In *24th European Microwave Conference*, volume 1, pages 395–400, September 1994.

[113] P. D. Mauskopf. Transition Edge Sensors and Kinetic Inductance Detectors in Astronomical Instruments. *Publications of the Astronomical Society of the Pacific*, 130(990):082001, June 2018.

[114] S. Doyle. *Lumped element kinetic inductance detector*. phdthesis, Cardiff University, 2008.

[115] S. Shu, M. Calvo, J. Goupy, et al. Optical Response of Lumped-Element Kinetic-Inductance Detector Arrays. *IEEE Transactions on Terahertz Science and Technology*, 8(6):605–612, November 2018.

[116] S. Wuensch, C. Groetsch, M. Merker, and M. Siegel. Optimized LEKID Structures With Low Crosstalk for Large Detector Arrays. *IEEE Transactions on Applied Superconductivity*, 25(3):1–5, June 2015.

[117] A. Adane, G. Coiffard, M. Calvo, et al. Study of the behavior of crosstalk in Hilbert KID array using Sonnet software. In *2014 11th International Workshop on Low Temperature Electronics (WOLTE)*, pages 81–84, July 2014.

[118] S. Shu. *Large format LEKID arrays for millimeter-wave astronomy*. phdthesis, IRAM Grenoble, 2019.

[119] J. Zmuidzinas. Superconducting Microresonators: Physics and Applications. *Annual Review of Condensed Matter Physics*, 3(1):169–214, 2012.

[120] R.A. Khmelnitsky and A.A. Gippius. Transformation of diamond to graphite under heat treatment at low pressure. *Phase Transitions*, 87(2):175–192, February 2014.

[121] G. Davies, T. Evans, and R.W. Ditchburn. Graphitization of diamond at zero pressure and at a high pressure. *Proceedings of the Royal Society of London. A. Mathematical and Physical Sciences*, 328(1574):413–427, June 1972.

[122] Y. V. Butenko, V. L. Kuznetsov, A. L. Chuvilin, et al. Kinetics of the graphitization of dispersed diamonds at low temperatures. *Journal of Applied Physics*, 88(7):4380–4388, 2000.

[123] R. Heidinger, G. Dammertz, A. Meier, and M. K. Thumm. CVD diamond windows studied with low- and high-power millimeter waves. *IEEE Transactions on Plasma Science*, 30(3):800–807, June 2002.

[124] A. Hoessinger. *Simulation of ion implantation for ULSI technology*. PhD thesis, Technical University Wien, July 2000.

[125] A. S. Cooper. Precise lattice constants of germanium, aluminum, gallium arsenide, uranium, sulphur, quartz and sapphire. *Acta Crystallographica*, 15(6):578–582, June 1962.

[126] L.N. Cooper. Superconductivity in the neighborhood of metallic contacts. *Physical Review Letters*, 6(12):689–690, June 1961.

[127] Y. V. Fominov and M. V. Feigel'man. Superconductive properties of thin dirty superconductor–normal-metal bilayers. *Physical Review B*, 63(9):094518, February 2001.

[128] D. K. Finnemore, T. F. Stromberg, and C. A. Swenson. Superconducting properties of high-purity niobium. *Physical Review*, 149(1):231–243, September 1966.

[129] J. Donohue. *Structures of the elements*. John Wiley and Sons, New York, 1974.

[130] R. L. Barns. Niobium: lattice parameter and density. *Journal of Applied Physics*, 39(8):4044–4045, 1968.

[131] S. Narumanchi, M. Mihalic, K. Kelly, and G. Eesley. Thermal interface materials for power electronics applications. In *2008 11th Intersociety Conference on Thermal and Thermomechanical Phenomena in Electronic Systems*, pages 395–404, 2008.

[132] A. Dillon, K. McCusker, J. Van Dyke, et al. Thermal interface material characterization for cryogenic electronic packaging solutions. In *IOP Conference Series: Materials Science and Engineering*, volume 278, page 012054. IOP Publishing, 2017.

[133] S Doyle, J Naylon, P. Mauskopf, et al. Lumped element kinetic inductance detectors. In *18th International Symposium on Space Terahertz Technology Proceedings*, 2007.

[134] G. Ulbricht, B. A. Mazin, P. Szypryt, et al. Highly multiplexible thermal kinetic inductance detectors for x-ray imaging spectroscopy. *Applied Physics Letters*, 106(25):251103, June 2015.

[135] T. Sugie, T. Hatae, Y. Koide, et al. Diagnostics System of JT-60U. *Fusion Science and Technology*, 42(2-3):482–511, November 2002.

[136] T. Akiyama, S. Tsuji-Iio, R. Shimada, et al. CO2 laser polarimeter for electron density profile measurement on the large helical device. *Review of Scientific Instruments*, 74(5):2695–2703, 2003.

[137] A. Boboc, M. Gelfusa, A. Murari, and P. Gaudio. Recent developments of the JET far-infrared interferometer-polarimeter diagnostic. *Review of Scientific Instruments*, 81(10):10D538, 2010.

[138] V. S. Asadchy, M. S. Mirmoosa, A. Díaz-Rubio, et al. Tutorial on electromagnetic nonreciprocity and its origins. *Proceedings of the IEEE*, 108(10):1684–1727, October 2020.

[139] A.W.M. Lee, Q. Qin, S. Kumar, et al. High-power and high-temperature THz quantum-cascade lasers based on lens-coupled metal-metal waveguides. *Optics letters*, 32(19):2840–2842, 2007.

[140] E. Logean, L. Hvozdara, J. DiFrancesco, et al. High numerical aperture silicon collimating lens for mid-infrared quantum cascade lasers manufactured using wafer-level techniques. In *Optical Systems Design 2012*. International Society for Optics and Photonics, December 2012.

[141] A. Arbabi, R. M. Briggs, Y. Horie, et al. Efficient dielectric metasurface collimating lenses for mid-infrared quantum cascade lasers. *Optics Express*, 23(26):33310–33317, December 2015.

[142] D. M. Slocum, E. J. Slingerland, R. H. Giles, and T. M. Goyette. Atmospheric absorption of terahertz radiation and water vapor continuum effects. *Journal of Quantitative Spectroscopy and Radiative Transfer*, 127:49–63, September 2013.

[143] S. Atakaramians, S. Afshar, T. M. Monro, and D. Abbott. Terahertz dielectric waveguides. *Advances in Optics and Photonics*, 5(2):169–215, June 2013.

[144] M. Nazarov, A. Shilov, Z. Margushev, et al. A flexible terahertz waveguide for delivery and filtering of quantum-cascade laser radiation. *Applied Physics Letters*, 113(13):131107, September 2018.

Schriftenreihe des Instituts für Angewandte Materialien

ISSN 2192-9963

Band 1 Prachai Norajitra
Divertor Development for a Future Fusion Power Plant.
ISBN 978-3-86644-738-7

Band 2 Jürgen Prokop
Entwicklung von Spritzgießsonderverfahren zur Herstellung von Mikrobauteilen durch galvanische Replikation.
ISBN 978-3-86644-755-4

Band 3 Theo Fett
New contributions to R-curves and bridging stresses – Applications of weight functions.
ISBN 978-3-86644-836-0

Band 4 Jérôme Acker
Einfluss des Alkali/Niob-Verhältnisses und der Kupferdotierung auf das Sinterverhalten, die Strukturbildung und die Mikrostruktur von bleifreier Piezokeramik $(K_{0,5}Na_{0,5})NbO_3$.
ISBN 978-3-86644-867-4

Band 5 Holger Schwaab
Nichtlineare Modellierung von Ferroelektrika unter Berücksichtigung der elektrischen Leitfähigkeit.
ISBN 978-3-86644-869-8

Band 6 Christian Dethloff
Modeling of Helium Bubble Nucleation and Growth in Neutron Irradiated RAFM Steels.
ISBN 978-3-86644-901-5

Band 7 Jens Reiser
Duktilisierung von Wolfram. Synthese, Analyse und Charakterisierung von Wolframlaminaten aus Wolframfolie.
ISBN 978-3-86644-902-2

Band 8 Andreas Sedlmayr
Experimental Investigations of Deformation Pathways in Nanowires.
ISBN 978-3-86644-905-3

Die Bände sind unter www.ksp.kit.edu als PDF frei verfügbar oder als Druckausgabe bestellbar.

Band 9 Matthias Friedrich Funk
Microstructural stability of nanostructured fcc metals during cyclic deformation and fatigue.
ISBN 978-3-86644-918-3

Band 10 Maximilian Schwenk
Entwicklung und Validierung eines numerischen Simulationsmodells zur Beschreibung der induktiven Ein- und Zweifrequenzrandschichthärtung am Beispiel von vergütetem 42CrMo4.
ISBN 978-3-86644-929-9

Band 11 Matthias Merzkirch
Verformungs- und Schädigungsverhalten der verbundstranggepressten, federstahldrahtverstärkten Aluminiumlegierung EN AW-6082.
ISBN 978-3-86644-933-6

Band 12 Thilo Hammers
Wärmebehandlung und Recken von verbundstranggepressten Luftfahrtprofilen.
ISBN 978-3-86644-947-3

Band 13 Jochen Lohmiller
Investigation of deformation mechanisms in nanocrystalline metals and alloys by in situ synchrotron X-ray diffraction.
ISBN 978-3-86644-962-6

Band 14 Simone Schreijäg
Microstructure and Mechanical Behavior of Deep Drawing DC04 Steel at Different Length Scales.
ISBN 978-3-86644-967-1

Band 15 Zhiming Chen
Modelling the plastic deformation of iron.
ISBN 978-3-86644-968-8

Band 16 Abdullah Fatih Çetinel
Oberflächendefektausheilung und Festigkeitssteigerung von niederdruckspritzgegossenen Mikrobiegebalken aus Zirkoniumdioxid.
ISBN 978-3-86644-976-3

Band 17 Thomas Weber
Entwicklung und Optimierung von gradierten Wolfram/EUROFER97-Verbindungen für Divertorkomponenten.
ISBN 978-3-86644-993-0

Die Bände sind unter www.ksp.kit.edu als PDF frei verfügbar oder als Druckausgabe bestellbar.

Band 18 Melanie Senn
Optimale Prozessführung mit merkmalsbasierter Zustandsverfolgung.
ISBN 978-3-7315-0004-9

Band 19 Christian Mennerich
Phase-field modeling of multi-domain evolution in ferromagnetic shape memory alloys and of polycrystalline thin film growth.
ISBN 978-3-7315-0009-4

Band 20 Spyridon Korres
On-Line Topographic Measurements of Lubricated Metallic Sliding Surfaces.
ISBN 978-3-7315-0017-9

Band 21 Abhik Narayan Choudhury
Quantitative phase-field model for phase transformations in multi-component alloys.
ISBN 978-3-7315-0020-9

Band 22 Oliver Ulrich
Isothermes und thermisch-mechanisches Ermüdungsverhalten von Verbundwerkstoffen mit Durchdringungsgefüge (Preform-MMCs).
ISBN 978-3-7315-0024-7

Band 23 Sofie Burger
High Cycle Fatigue of Al and Cu Thin Films by a Novel High-Throughput Method.
ISBN 978-3-7315-0025-4

Band 24 Michael Teutsch
Entwicklung von elektrochemisch abgeschiedenem LIGA-Ni-Al für Hochtemperatur-MEMS-Anwendungen.
ISBN 978-3-7315-0026-1

Band 25 Wolfgang Rheinheimer
Zur Grenzflächenanisotropie von $SrTiO_3$.
ISBN 978-3-7315-0027-8

Band 26 Ying Chen
Deformation Behavior of Thin Metallic Wires under Tensile and Torsional Loadings.
ISBN 978-3-7315-0049-0

Band 27 Sascha Haller
Gestaltfindung: Untersuchungen zur Kraftkegelmethode.
ISBN 978-3-7315-0050-6

Band 28 Nicht erschienen

Band 29 Gunnar Picht
Einfluss der Korngröße auf ferroelektrische Eigenschaften dotierter $Pb(Zr_{1-x}Ti_x)O_3$ Materialien.
ISBN 978-3-7315-0106-0

Band 30 Esther Held
Eigenspannungsanalyse an Schichtverbunden mittels inkrementeller Bohrlochmethode.
ISBN 978-3-7315-0127-5

Band 31 Pei He
On the structure-property correlation and the evolution of Nanofeatures in 12-13.5% Cr oxide dispersion strengthened ferritic steels.
ISBN 978-3-7315-0141-1

Band 32 Jan Hoffmann
Ferritische ODS-Stähle – Herstellung, Umformung und Strukturanalyse.
ISBN 978-3-7315-0157-2

Band 33 Wiebke Sittel
Entwicklung und Optimierung des Diffusionsschweißens von ODS Legierungen.
ISBN 978-3-7315-0182-4

Band 34 Osama Khalil
Isothermes Kurzzeitermüdungsverhalten der hoch-warmfesten Aluminium-Knetlegierung 2618A (AlCu2Mg1,5Ni).
ISBN 978-3-7315-0208-1

Band 35 Nicht erschienen

Band 36 Christoph Hage
Grundlegende Aspekte des 2K-Metallpulverspritzgießens.
ISBN 978-3-7315-0217-3

Band 37 Bartłomiej Albiński
Instrumentierte Eindringprüfung bei Hochtemperatur für die Charakterisierung bestrahlter Materialien.
ISBN 978-3-7315-0221-0

Band 38 Tim Feser
Untersuchungen zum Einlaufverhalten binärer alpha-Messinglegierungen unter Ölschmierung in Abhängigkeit des Zinkgehaltes.
ISBN 978-3-7315-0224-1

Band 39 Jörg Ettrich
Fluid Flow and Heat Transfer in Cellular Solids.
ISBN 978-3-7315-0241-8

Band 40 Melanie Syha
Microstructure evolution in strontium titanate Investigated by means of grain growth simulations and x-ray diffraction contrast tomography experiments.
ISBN 978-3-7315-0242-5

Band 41 Thomas Haas
Mechanische Zuverlässigkeit von gedruckten und gasförmig abgeschiedenen Schichten auf flexiblem Substrat.
ISBN 978-3-7315-0250-0

Band 42 Aron Kneer
Numerische Untersuchung des Wärmeübertragungsverhaltens in unterschiedlichen porösen Medien.
ISBN 978-3-7315-0252-4

Band 43 Manuel Feuchter
Investigations on Joule heating applications by multiphysical continuum simulations in nanoscale systems.
ISBN 978-3-7315-0261-6

Band 44 Alexander Vondrous
Grain growth behavior and efficient large scale simulations of recrystallization with the phase-field method.
ISBN 978-3-7315-0280-7

Band 45 Tobias Kennerknecht
Fatigue of Micro Molded Materials – Aluminum Bronze and Yttria Stabilized Zirconia.
ISBN 978-3-7315-0293-7

Band 46 Christopher Scherr
Elektrochemisches Verhalten von Lithium-Schwefel-Zellen mit unterschiedlicher Kathodenstruktur.
ISBN 978-3-7315-0296-8

Band 47 Konstantin Frölich
Der Decal-Prozess zur Herstellung katalysatorbeschichteter Membranen für PEM-Brennstoffzellen.
ISBN 978-3-7315-0334-7

Band 48 Benedikt Haspel
Werkstoffanalytische Betrachtung der Eigenschaften von mittels neuartiger RTM-Fertigungsprozesse hergestellten glasfaserverstärkten Polymerverbunden.
ISBN 978-3-7315-0337-8

Band 49 Marco Berghoff
Skalenübergreifende Modellierung und Optimierung vom atomistischen kristallinen Phasenfeldmodell bis zur mesoskopischen Phasenfeldmethode.
ISBN 978-3-7315-0416-0

Band 50 Michael Selzer
Mechanische und Strömungsmechanische Topologie-optimierung mit der Phasenfeldmethode.
ISBN 978-3-7315-0431-3

Band 51 Michael Mahler
Entwicklung einer Auswertemethode für bruchmechanische Versuche an kleinen Proben auf der Basis eines Kohäsivzonenmodells.
ISBN 978-3-7315-0441-2

Band 52 Christoph Bohnert
Numerische Untersuchung des Verformungs- und Bruchverhaltens von einkristallinem Wolfram auf mikroskopischer Ebene.
ISBN 978-3-7315-0444-3

Band 53 Stefan Guth
Schädigung und Lebensdauer von Nickelbasislegierungen unter thermisch-mechanischer Ermüdungsbeanspruchung bei verschiedenen Phasenlagen.
ISBN 978-3-7315-0445-0

Band 54 Markus Klinsmann
The Effects of Internal Stress and Lithium Transport on Fracture in Storage Materials in Lithium-Ion Batteries.
ISBN 978-3-7315-0455-9

Band 55 Thomas Straub
Experimental Investigation of Crack Initiation in Face-Centered Cubic Materials in the High and Very High Cycle Fatigue Regime.
ISBN 978-3-7315-0471-9

Band 56 Maren Lepple
Kupfer- und Eisenoxide als Konversions-Elektrodenmaterialien für Lithium-Ionen-Batterien: Thermodynamische und Elektrochemische Untersuchungen.
ISBN 978-3-7315-0482-5

Band 57 Stefan Andreas Slaby
Charakterisierung und Bewertung der Zug- und Ermüdungseigenschaften von Mikrobauteilen aus 17-4PH Edelstahl. Ein Vergleich von mikropulverspritzgegossenem und konventionell hergestelltem Material.
ISBN 978-3-7315-0484-9

Band 58 Kumar Ankit
Phase-field modeling of microstructural pattern formation in alloys and geological veins.
ISBN 978-3-7315-0491-7

Band 59 Kuo Zhang
Characterization and Modeling of the Ratcheting Behavior of the Ferritic-Martensitic Steel P91.
ISBN 978-3-7315-0503-7

Band 60 Nicht erschienen

Band 61 Fabian Lemke
Untersuchung des Sinterverhaltens von $SrTiO_3$ unter Berücksichtigung der Defektchemie.
ISBN 978-3-7315-0510-5

Band 62 Johannes Kümmel
Detaillierte Analyse der Aufbauschneidenbildung bei der Trockenzerspanung von Stahl C45E mit Berücksichtigung des Werkzeugverschleißes.
ISBN 978-3-7315-0518-1

Band 63 László Hagymási
Modellierung der Stoffübertragung beim Niederdruckcarbonitrieren mit Ammoniak und Acetylen.
ISBN 978-3-7315-0568-6

Band 64 Reza Eslami
A novel micro-mechanical model for prediction of multiaxial high cycle fatigue at small scales.
ISBN 978-3-7315-0583-9

Band 65 Sebastian Schulz
Phase-field simulations of multi-component solidification and coarsening based on thermodynamic datasets.
ISBN 978-3-7315-0618-8

Band 66 Markus Stricker
Die Übertragung von mikrostrukturellen Eigenschaften aus der diskreten Versetzungsdynamik in Kontinuumsbeschreibungen.
ISBN 978-3-7315-0658-4

Band 67 Luis Straßberger
Untersuchung und Modellierung des viskoplastischen Verformungsverhaltens oxidpartikelverstärkter Stähle.
ISBN 978-3-7315-0674-4

Band 68 Mark Wobrock
Microplasticity of idealized single crystalline Ag cantilevers characterized with methods of high resolution.
ISBN 978-3-7315-0682-9

Band 69 Amritesh Kumar
Micromechanical study on the deformation behaviour of directionally solidified NiAl-Cr eutectic composites.
ISBN 978-3-7315-0694-2

Band 70 Johannes Hötzer
Massiv-parallele und großskalige Phasenfeldsimulationen zur Untersuchung der Mikrostrukturentwicklung.
ISBN 978-3-7315-0693-5

Band 71 Thomas Hupfer
Herstellung von LATP für den Einsatz als Festkörperelektrolyt und dessen Eigenschaften.
ISBN 978-3-7315-0702-4

Band 72 Florentin Pottmeyer
Schädigungsverhalten von in CFK-Laminaten eingebetteten Inserts unter bauteilnahen Beanspruchungen.
ISBN 978-3-7315-0719-2

Band 73 Andres Höweling
Untersuchung der Hochvoltstabilität und Tiefentladung von dotierten $LiNi_{0,5}Mn_{1,5}O_4$-Hochvoltspinellen.
ISBN 978-3-7315-0728-4

Band 74 Tabea Gisela Schwark
Deformation and Fracture Properties of the Soft Magnetic Composite Somaloy 700 3P on Different Length Scales.
ISBN 978-3-7315-0759-8

Band 75 Klaudia Lichtenberg
Metallmatrixverbunde mit Verstärkungselementen aus metallischem Glas $Ni_{60}Nb_{20}Ta_{20}$ – Herstellung und Charakterisierung.
ISBN 978-3-7315-0782-6

Band 76 Claudio Findeisen
Charakterisierung und Modellierung von instabilen Metamaterialien.
ISBN 978-3-7315-0869-4

Band 77 Nilesha Mishra
Influence of strain on the functionality of ink-jet printed thin films and devices on flexible substrates.
ISBN 978-3-7315-0853-3

Band 78 Simon Werner Bonk
Plastische Verformungsmechanismen in hochgradig kaltgewalzten, ultrafeinkörnigen Wolframblechen.
ISBN 978-3-7315-0878-6

Band 79 Tim Gräning
Herstellung, Charakterisierung und Optimierung von austenitischen ODS Stählen.
ISBN 978-3-7315-0732-1

Band 80 Peter Rupp
Herstellung, Prüfung und Modellierung neuartiger hybrider Aluminiumschaum-CFK-Sandwichverbunde.
ISBN 978-3-7315-0880-9

Band 81 Benjamin Sebastian Ehreiser
Einfluss mechanischer Lasten auf die Herstellung von Stahl-Glaskeramik-Verbunden.
ISBN 978-3-7315-0954-7

Band 82 Hans Giel
Weiterentwicklung experimenteller Methoden zur Ermittlung thermodynamischer Werkstoffdaten von Lithium-Ionen-Batterien.
ISBN 978-3-7315-0981-3

Band 83 Anna Trauth
Characterisation and Modelling of Continuous-Discontinuous Sheet Moulding Compound Composites for Structural Applications.
ISBN 978-3-7315-0950-9

Band 84 Jonas Johannes Hüther
The Impact of Recycling on the Fibre and the Composite Properties of Carbon Fibre Reinforced Plastics.
ISBN 978-3-7315-0983-7

Band 85 Nicolas A. Mayer
Thermodynamik von Kobaltoxid Anodenmaterialien für Lithium-Ionen-Batterien und ihr elektrochemisches Verhalten.
ISBN 978-3-7315-0996-7

Band 86 Ulrich Führer
Untersuchung und Modellierung des Haltezeiteinflusses auf die zyklische Entfestigung ferritisch-martensitischer Stähle.
ISBN 978-3-7315-0837-3

Band 87 Ebru Cihan
Structure evolution in tribological interfaces studied by multilayer model alloys.
ISBN 978-3-7315-0999-8

Band 88 Markus Sudmanns
Entwicklung einer Kontinuumsbeschreibung für die Versetzungsmobilität in Versetzungsnetzwerken.
ISBN 978-3-7315-1001-7

Band 89 Tao Zhang
Phase-field Modeling of Phase Changes and Mechanical Stresses in Electrode Particles of Secondary Batteries.
ISBN 978-3-7315-1002-4

Band 90 Markus Ganser
On the Electro-Chemo-Mechanical Coupling in Solid State Batteries and its Impact on Morphological Interface Stability.
ISBN 978-3-7315-1047-5

Band 91 Michael Kellner
Modellierung mehrkomponentiger Materialsysteme für die Phasenfeldmethode und Analyse der simulierten Mikrostrukturen.
ISBN 978-3-7315-1044-4

Band 92 Felix Schröckert
Herstellung dünner Folien aus Lithium-Lanthan-Titanat zur Anwendung als Festkörperelektrolyt.
ISBN 978-3-7315-1008-6

Band 93 Ephraim Schoof
Chemomechanische Modellierung der Wärmebehandlung von Stählen mit der Phasenfeldmethode.
ISBN 978-3-7315-1050-5

Band 94 Alexander Valentin Brabänder
Registrierende Härtemessung an neutronenbestrahlten Materialien bei hohen Temperaturen.
ISBN 978-3-7315-1097-0

Band 95 Denny Schmidt
Einfluss der Kompaktierung auf die Elektrodenmikrostruktur und elektrochemische Performance bei Lithium-Ionen-Zellen.
ISBN 978-3-7315-1098-7

Band 96 Svenja Dittrich
Entwicklung von Siebdruckpasten zur Herstellung von Glaslotfügungen für die Festoxidbrennstoffzelle.
ISBN 978-3-7315-1085-7

Band 97 Michael Dippon
Bestimmung der Betriebsgrenzen für das Schnellladen von Lithium-Ionen Batterien.
ISBN 978-3-7315-1123-6

Band 98 Patricia Haremski
Diffusionseigenschaften von Nickel in einer Festoxid-Brennstoffzelle.
ISBN 978-3-7315-1124-3

Band 99 Florian Wankmüller
Mehrskalige Charakterisierung der Hochtemperatur-Brennstoffzelle (SOFC).
ISBN 978-3-7315-1142-7

Band 100 Niklas Russner
Modellgestützte Analyse des Stackbetriebs von Festoxidzellen.
ISBN 978-3-7315-1144-1

Band 101 Theo Fett, Karl G. Schell, Ethel C. Bucharsky, Gabriele Rizzi, Pascal Hettich, Susanne Wagner, Michael J. Hoffmann
Consequences of hydroxyl generation by the silica/water reaction - Part I: Diffusion and Swelling.
ISBN 978-3-7315-1148-9

Band 102 Theo Fett, Karl G. Schell, Ethel C. Bucharsky, Gabriele Rizzi, Susanne Wagner, Michael J. Hoffmann
Consequences of hydroxyl generation by the silica/water reaction - Part II: Global and local Swelling
Part III: Damage and Young's Modulus.
ISBN 978-3-7315-1159-5

Band 103 Johannes Dornheim
Modellfreies Lernen optimaler zeitdiskreter Regelungsstrategien für Fertigungsprozesse mit endlichem Zeithorizont.
ISBN 978-3-7315-1158-8

Band 104 Markus Muth
Grundlagenuntersuchungen an intrinsisch gefertigten lasttragenden FVK/Metall-Hybridträgern.
ISBN 978-3-7315-1161-8

Band 105 Oleg Birkholz
Modeling transport properties and electrochemical performance of hierarchically structured lithium-ion battery cathodes using resistor networks and mathematical half-cell models.
ISBN 978-3-7315-1172-4

Band 106 Verena Irene Becker
Modellierung der Mechanik und der effektiven Transportei genschaften von partikulären Kathoden sowie deren Einfluss auf die elektrochemische Performance von Lithium-Ionen-Batterien.
ISBN 978-3-7315-1174-8

Band 107 Nikolai Zimber
Nanoskalige Analytik der Mikrostruktur von hochdosig bestrahltem Beryllium.
ISBN 978-3-7315-1178-6

Band 108 Francesco Mazzocchi
Development of NbN based Kinetic Inductance Detectors on sapphire and diamond substrates for fusion plasma polarimetric diagnostics.
ISBN 978-3-7315-1181-6

KARLSRUHER INSTITUT FÜR TECHNOLOGIE (KIT)
SCHRIFTENREIHE DES INSTITUTS FÜR ANGEWANDTE MATERIALIEN

This work aimed at designing, studying and producing the first prototypes of Kinetic Inductance Detectors tailored for fusion plasma polarimetric diagnostics in the terahertz range. Two well established substrate materials, silicon and sapphire, as well as diamond, were investigated. Diamond was considered in this innovative role given its unmatched optical, radiation hardness and thermal qualities that make it an ideal choice for the detection of low power signals in working environments potentially saturated with radiation. This is the first study of diamond as a substrate for low-temperature superconducting thin films and represents a first step toward the optimization and final application of this technology.

ISSN 2192-9963
ISBN 978-3-7315-1181-6

Gedruckt auf FSC-zertifiziertem Papier